Scanning Tunneling

Microscopy and Spectroscopy

of Magnetic Molecules

on Surfaces

Dissertation
zur Erlangung des Doktorgrades
des Fachbereichs Physik
der Universität Hamburg

vorgelegt von
Stefan Kuck
aus Hamburg

Hamburg
2009

Gutachter der Dissertation:	Prof. Dr. R. Wiesendanger
	Prof. Dr. M. H. Prosenc
Gutachter der Disputation:	Prof. Dr. R. Wiesendanger
	Prof. Dr. M. Bröring
Datum der Disputation:	20.03.2009
Vorsitzender des Prüfungsausschusses:	Prof. Dr. H. P. Oepen
Vorsitzender des Promotionsausschusses:	Prof. Dr. R. Klanner
Dekan der MIN-Fakultät:	Prof. Dr. H. Graener
Departmentleiter:	Prof. Dr. J. Bartels

Abstract

In this thesis the experimental results of scanning tunneling microscopy (STM) and scanning tunneling spectroscopy (STS) investigations of metal-organic molecules with a central magnetic ion, i.e. cobalt or iron, adsorbed on different surfaces are presented.

Before the magnetism of these metal-organic complexes can be studied, the basic behavior concerning adsorption, growth and electronic structure has to be understood first.

Two new molecular species are introduced to the field of STM: the cobalt-salen, derived from a Schiff base introduced by Schiff already in 1864 [1], and the iron-triphenylcorrole from the relatively new class of corrole molecules, first named in 1960 by Johnson and Price [2]. In addition, a comparative study of phthalocyanine (PC) molecules with different metallic centers was carried out. The molecules were investigated on Cu(111), Cu(100), and on NaCl/Cu(111).

As a beginning, the influence of the two facets of copper on the adsorption behavior of the fourfold symmetric phthalocyanine was studied and is presented in chapter 4. On the Cu(100) surface, two meta-stable orientations in addition to the already reported two orientations were found when preparing PC molecules on the cooled substrate. A symmetry reduction, turning the fourfold PC into a deformed twofold symmetric entity, was observed when preparing MPCs on Cu(111).

Chapter 5 covers the study of different Co-Salen derivatives. Co-Salen molecules exhibit chirality in the gas phase due to a deformation of the otherwise planar molecule. The consequence of this chirality on the adsorption was studied on the two facets of copper and on NaCl/Cu(111). In the more extensive study, STS was performed on single molecules on Cu(111). This includes spatial mapping of electronic states ($\mathrm{d}I/\mathrm{d}U$-map) and point spectroscopy. Using manipulation with the STM tip, molecules were successfully and reproducibly dehydrogenated and the influence on the electronic structure was studied. Additionally, by selectively exchanging substituents in the 5,5'-positions of Co-Salen molecules (provided by the chemistry group of Prof. M. Prosenc in Hamburg), the interaction among molecules on the surface could be tuned from repulsive to attractive, resulting in either single molecules or self-assembled clusters and networks on terraces.

Chapter 6 presents results for various derivatives of iron-corrole molecules (synthesized in the group of Prof. M. Bröring in Marburg) with different axial groups bound to the central iron atom, revealing a dissociation of the axial group for all corrole complexes already during the preparation. This enabled a study of pure iron-corrole molecules. The iron-corrole molecule, which is closely related to the porphyrin molecule, exhibits a saddle distortion of the macrocycle when adsorbed

on a metallic substrate similar to the porphyrin. This induces chirality and molecules become completely asymmetric. The influence of the two different surface geometries (sixfold for Cu(111) and fourfold for Cu(100)) on the adsorption, self-assembly and electronic structure was studied.

Kurzfassung

In dieser Arbeit werden die Ergebnisse einer Untersuchung mittels Rastertunnel-mikroskopie (STM für *engl. scanning tunneling microscopy*) und Rastertunnelspek-troskopie (STS) an metall-organischen Molekülen auf verschiedenen Oberflächen präsentiert. Die hierfür verwendeten Moleküle besitzen ein magnetisches Atom im Zentrum, z.B. Kobalt oder Eisen. Bevor der Magnetismus an diesen Molekül-komplexen studiert werden kann, müssen zunächst grundlegende Eigenschaften, wie Adsorption, Wachstum oder die elektronische Struktur verstanden sein. Zwei neue Molekülklassen werden zum ersten mal mittels STM untersucht: Das Kobaltsalen, abgeleitet von einer Schiff Base und eingeführt bereits 1864 von Schiff [1] sowie das Eisencorrol, benannt 1960 von Johnson und Price [2]. Zusätzlich wurde noch eine vergleichende Studie von Phthalocyanin Molekülen mit verschiedenen Metallzentren durchgeführt. Alle Moleküle wurden auf den Substraten Cu(111), Cu(100) und auf NaCl/Cu(111) untersucht.

Zunächst wurde der Einfluß der beiden Oberflächengeometrien von Kupfer auf das Adsorptionsverhalten des vierzähligen Phthalocyanins (PC) untersucht und ist in Kapitel 4 zusammengefasst. Auf der Cu(100)-Oberfläche wurden zusätzlich zu den zwei aus der Literatur bekannten Orientierungen noch zwei meta-stabile Zustände gefunden, wenn die PC-Moleküle auf der kalten Probe präpariert wurden. Ein Sym-metriebruch, der das vierzählige PC in ein Zweizähliges verformt, wurde bei der Präparation von MPCs auf Cu(111) gefunden.

Kobaltsalen Moleküle besitzen durch eine Deformierung des ansonsten planaren Moleküls bereits in der Gasphase eine Chiralität. Deren Auswirkung auf das Ad-sorptionsverhalten wurde auf den oben benannten Oberflächen untersucht. In einer ausführlicheren Studie auf Cu(111) wurden die Moleküle mittels Rastertunnelspek-troskopie untersucht. Dies umfasste auch die Aufnahme von Karten der differen-ziellen Leifähigkeit (dI/dU-Karten), die eine räumliche Auflösung der elektronischen Zustände darstellen. Durch Manipulation mit der STM-Spitze wurden erfolgreich und reproduzierbar Wasserstoffatome aus dem oberen Teil des Moleküls abgespalten und die Auswirkung auf die elektronische Struktur untersucht. Zusätzlich wurden gezielt die Substituenten in den 5,5'-Positionen ausgetauscht (durchgeführt in der Arbeitsgruppe von Prof. M. Prosenc in Hamburg) um die Wechselwirkung zwischen den Molekülen von abstoßend auf attraktiv zu schalten. Dadurch konnten entweder Einzelmoleküle oder selbstangeordnete Netzwerke auf der Oberfläche erzeugt wer-den. Dieser Teil ist in Kapitel 5 beschrieben.

Verschiedene Derivate des Eisencorrols (synthetisiert in der Arbeitsgruppe von Prof. M. Bröring in Marburg) mit unterschiedlichen Axialgruppen wurden studiert. Die Untersuchung ergab die Abspaltung der Axialgruppen bereits während der

Präparation und alle weiteren Experimente wurden an dem reinen Eisencorrol ohne Axialgruppe durchgeführt. Das Eisencorrol, welches eng mit dem Pophyrin verwandt ist, liegt auf dem metallischen Substrat analog zum Porphyrin in einer Sattel-Konformation vor. Diese Deformation des Makrozyklusses erzeugt eine Chiralität im Molekül auf der Oberfläche und es wird komplett asymmetrisch. Der Einfluß der beiden Oberflächengeometrien (sechsfach bei Cu(111) und vierfach bei Cu(100)) auf die Adsorption, das selbstangeordnete Wachstum und die elektronische Struktur wurden untersucht. Die Ergebnisse sind in Kapitel 6 dargestellt.

Contents

II STM Experiments on Individual Molecules   37

4 Symmetry Effects of MPCs on Copper Surfaces   39

5 Co-Salen   47

6 Iron TriPhenylCorrole (FeTPC)   75

7 Summary and Outlook   101

Bibliography   109

Publications   111

Conferences   113

Acknowledgements   115

Introduction

Living in the information age where the importance of Moore's Law and magnetic storage devices is omnipresent, the scientific interest on magnetic nanostructures on surfaces is constantly growing. The demand for improved hard disk drives and alternative information storage systems can only be satisfied by an increasing density of information. However, the limit of the current hard disk drive technology (predicted to be 1 Tbit/in^2) is in reach. One way to overcome this limit is an exchange of normal magnetic domains for single bits with new materials. For this new approach with different admaterials as magnetic bits, molecules have entered the stage as a class of metal-organic hybrid systems which already take part in nearly every branch of industry (e.g. OLEDs, organic solar cells, catalysts for fuel cells). One unique aspect of metal-organic molecules is the combination of various properties, e.g. conductance, optical properties and magnetism.

Since the theoretical description of a molecular rectifier by Aviram and Ratner in 1974 [3], which was experimentally confirmed by Martin *et al.* [4], molecules are highly anticipated to further advance the pace of development in the field of electronic devices. An important issue in molecular electronics is the determination of the resistance of a single molecule (both theoretical and experimental). The main approach studying these properties is the field of break junctions, where single molecules and molecular wires are contacted from two sides [5]. This leads to stunning results including Kondo resonance in single-molecule transistors [6, 7]. The demands on the theory to calculate these more and more complex systems have grown, but the methods used by theory advanced as well, for example through the introduction of 'Smeagol' by S. Sanvito [8]. Also STM was used to determine the conductivity of molecules in a single molecular switch [9].

For the use of molecular films on surfaces, the understanding of the adsorption and coupling leading to different effects in the electronic and magnetic structure is of utter importance. Therefore, the investigation of molecules on surfaces has to be studied on the local scale to first understand the properties of single molecules. For exactly that purpose, STM is the best tool.

For the understanding of processes on the molecular level, isolated molecules on surfaces have to be studied. Therefore, all experiments presented in this thesis were carried out in ultra-high vacuum (UHV) with the sample at low temperatures (25 K).

The combined effort of both disciplines, physics and chemistry, is necessary to get complete insight into this complicated field of metal-organic systems on surfaces. Therefore, the study presented in this thesis was carried out in close collaboration with two leading chemistry groups. The molecules provided by these

groups are studied with STM for the first time: the cobalt-salen molecule provided by Prof. M. Prosenc in Hamburg and the iron-corrole synthesized in the group of Prof. M. Bröring in Marburg. With the help of chemistry, the understanding of molecular processes and effects on the surface is ameliorated. Also the high flexibility of exchanging substituents in the molecules, made possible by the expertise of the chemists, allows delicate tuning and steering of certain effects and properties of the molecules on the surface.

Additionally, the support from theory is very important. DFT calculations were performed by the group of Prof. S. Sanvito in Dublin, but the results are still preliminary and therefore only a selected preview is shown.

Part I

Principles of STM Studies on Molecular Systems: Fundamentals, Instrumentation and Preparation

Chapter 1

Fundamentals
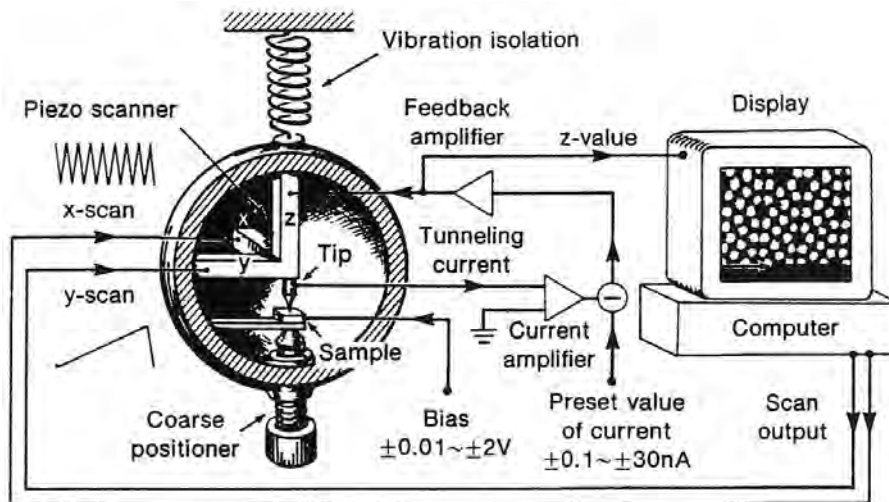
Figure 1.1: Schematic concept of a scanning tunneling microscope; taken from [10]. After coarse positioning the tip in tunneling distance to the sample, the tip is raster-scanned over the surface applying adequate waveforms to the x- and y-piezos. The z-piezo is modifying the distance, keeping the current constant on a preset value. The regulated values for z are recorded and displayed in the computer as topographic images. For high precision measurements, vibration isolation is essential.

1.1   Theory of STM

The scanning tunneling microscope (STM) was invented by Binnig and Rohrer and implemented by Binnig, Rohrer, Gerber, and Weibel in 1982 [11, 12]. Figure 1.1 shows its essential elements. A probe conductive tip, usually made of W or Pt-Ir alloy, is attached to a piezodrive, that consists of three mutually perpendicular piezo-electric transducers: x-, y-, and z-piezo. In more recent designs this piezoelement for tip positioning is exchanged with a segmented piezotube (see Sec. 2.4). Upon applying a voltage, the piezo element expands or contracts moving the probe tip in all three dimensions. By applying a sawtooth voltage on the x-piezo and a voltage

ramp on the y-piezo, the tip scans within the xy-plane. Using the coarse positioner and the z-piezo, the tip and sample are brought to within a few ångströms of each other. The electron wavefunctions of the tip overlap with electron wavefunctions of the sample surface. A bias voltage, applied between tip and sample, causes an electrical current to flow. Such a current is the manifestation of a quantum mechanical phenomenon, tunneling. An elementary theory of tunneling is presented in Sec. 1.1.1.

The highly sensitive tunneling current (typically of the order of a few pA to a few nA) is amplified by the current amplifier and converted into a voltage (range of ± 10 V). In the normal operation mode, the current is compared to a reference set-point and kept constant during scanning over a surface by adjusting the tip-sample distance. This is realized by a modification of the voltage applied to the z-piezo, to regulate the z-position of the tip. During scanning over a surface, these changes in z are recorded and displayed in a color encoded image also called topographic image.

For high precision measurements on the atomic level, a vibrational isolation system is necessary. This is often realized in two stages: damping the microscope via springs and the whole setup via pneumatic damping legs.

1.1.1   Elementary Theory of Tunneling

The concept of the quantum mechanical tunneling is best understood within the elementary model of tunneling through a one-dimensional potential barrier.

In classical mechanics, an electron with the energy E moving in a potential $U(z)$ is described by

$$\frac{p^2}{2m} + U(z) = E, \tag{1.1}$$

where m is the electron mass. In regions where $E > U(z)$, the electron has a nonzero momentum $p = [2m(E - U)]^{1/2}$. On the other hand, the electron cannot penetrate into any region with $E < U(z)$, or a *potential barrier*. In quantum mechanics, the state of the electron is described by a wavefunction $\psi(z)$, that satisfies Schrödinger's equation,

$$-\frac{\hbar^2}{2m}\frac{d^2}{dz^2}\psi(z) + U(z)\psi(z) = E\psi(z). \tag{1.2}$$

Consider the case of a piecewise-constant potential, as shown in Fig. 1.2. In the classically allowed region, $E > U$, Eq. 1.2 has solutions

$$\psi(z) = \psi(0)\mathrm{e}^{\pm ikz}, \tag{1.3}$$

where

$$k = \frac{\sqrt{2m(E - U)}}{\hbar} \tag{1.4}$$

is the wave vector. The electron is moving (in either a positive or negative direction) with a constant momentum $p = \hbar k$, or a constant velocity $v = p/m$, as in the classical case. In the classically forbidden region, Eq. 1.2 has solutions
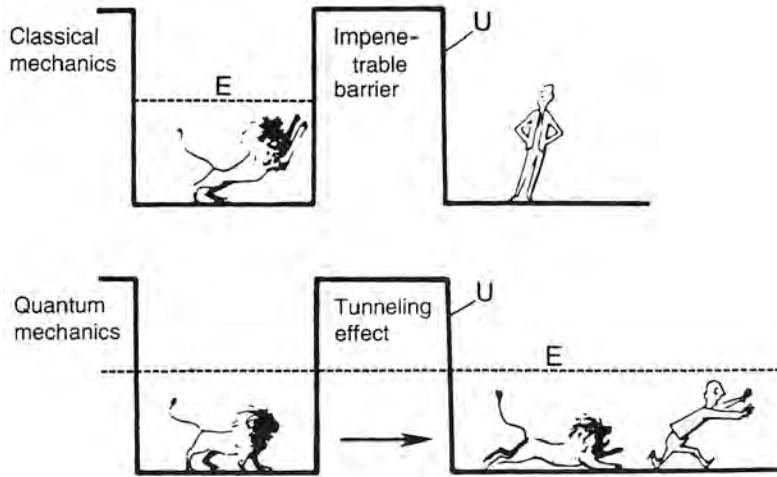
Figure 1.2: The difference between classical theory and quantum theory. In quantum mechanics, an electron has a nonzero probability of tunneling through a potential barrier. Taken from [10].

$$\psi(z) = \psi(0)\mathrm{e}^{-\kappa z}, \tag{1.5}$$

where

$$\kappa = \frac{\sqrt{2m(U - E)}}{\hbar} \tag{1.6}$$

is the decay constant. It describes a state of the electron penetrating through the barrier into the $+z$-direction. The probability density of observing an electron near a point z is proportional to $|\psi(0)|^2 \mathrm{e}^{-2\kappa z}$, which has a nonzero value in the barrier region, thus has a nonzero probability to penetrate the barrier. Another solution, $\psi(z) = \psi(0)\mathrm{e}^{\kappa z}$, describes an electron state decaying in the $-z$-direction. It is usually too small to be significant.

Starting from this elementary model, some basic features of metal-vacuum-metal tunneling can be explained. The *work function ϕ* of a metal surface is defined as the minimum energy required to remove an electron from the bulk to the vacuum level. In general, the work function depends not only on the material, but also on the crystallographic orientation of the surface. For example the experimental values for the two facets of copper, important in this thesis later on, are given by [13] as $\phi = 4.85$ eV (111) and $\phi = 4.55$ eV (100). Neglecting thermal excitations, the Fermi level is the upper limit of the occupied states in a metal. Taking the vacuum level as the reference point of energy, this results in $E_{\mathrm{F}} = -\phi$. For simplification, the work functions of tip and sample are assumed to be equal.

The *transmission coefficient T* is defined as the ratio of the transmitted current to the impinging current at $z = 0$,

$$T \equiv \frac{I(z)}{I(0)} \simeq \mathrm{e}^{-2\kappa z}, \tag{1.7}$$

where the limit of a thick and high tunnel barrier has been assumed, and

$$\kappa = \frac{\sqrt{2m\phi}}{\hbar} \tag{1.8}$$

is the decay constant of a sample state near the Fermi level in the barrier region. The numerical value for the decay constant is

$$\kappa = 5.1\sqrt{\phi(eV)}\ \text{nm}^{-1}. \tag{1.9}$$

Taking the average of the copper values for ϕ from above, a typical value of the decay constant is $\kappa \approx 11.2$ nm^{-1}. According to Eq. 1.7, the tunneling current decays 9.4 times, or one order of magnitude per 1 Å.

1.1.2   Bardeen Approximation and Topographic Imaging

The standard theoretical method for the understanding of a tunneling junction is the time-dependent perturbation approach developed by Bardeen [14]. Instead of trying to solve the Schrödinger equation of the combined system, Bardeen considers two separate subsystems first. The electronic states of the separated subsystems are obtained by solving the stationary Schrödinger equations. For many practical systems, those solutions are known. The rate of transferring an electron from one electrode of a tunneling junction to another is calculated using time-dependent perturbation theory. As a result, Bardeen showed that the amplitude of electron transfer, or the tunneling matrix element M, is determined by the overlap of the surface wavefunctions of the two subsystems. Assuming an STM tip over a surface as these two subsystems in a tunneling junction, the current of tunneling electrons is given by

$$I = \frac{2\pi e}{\hbar} \sum_{\mu,\nu} \left\{ f(E_\mu)[1 - f(E_\nu + eU)] - f(E_\nu + eU)[1 - f(E_\mu)] \right\} |M_{\mu\nu}|^2 \delta(E_\mu - E_\nu), \tag{1.10}$$

where $f(E)$ is the Fermi function, U is the applied voltage, $M_{\mu\nu}$ is the tunneling matrix element between wave functions ψ_μ of the tip and ψ_ν of the sample, and E_μ is the energy of state ψ_μ in the absence of tunneling. In the limits of small voltages and temperatures it turns into

$$I = \frac{2\pi}{\hbar} e^2 U \sum_{\mu,\nu} |M_{\mu\nu}|^2 \delta(E_\nu - E_\text{F}) \delta(E_\mu - E_\text{F}). \tag{1.11}$$

As shown by Bardeen, the tunneling matrix element can be written as

$$M_{\mu\nu} = \frac{\hbar^2}{2m} \int \text{d}S (\psi_\mu^* \nabla \psi_\nu - \psi_\nu \nabla \psi_\mu^*) \tag{1.12}$$

where the integral corresponds to a surface within the barrier region between the sample and tip. To evaluate $M_{\mu\nu}$ in a way that the resulting expression for I can be compared quantitatively with STM images in general (i.e. not for one specific choice of sample and tip) requires several approximations. Tersoff and Hamann [15]
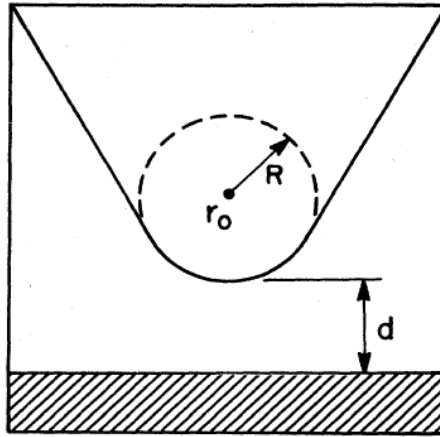
Figure 1.3: Schematic picture of tunneling geometry. The probe tip is assumed locally spherical with a curvature radius R and the position of the curvature center r_0. The distance of nearest approach is d (taken from [15]).

showed that by assuming a locally spherical potential well for the tip with only s-wave functions, I could be expressed as

$$I \propto \sum_{\nu} |\psi_{\nu}(\overrightarrow{r_0})|^2 \delta(E_{\nu} - E_{\mathrm{F}}) \tag{1.13}$$

with $\overrightarrow{r_0}$ as the location of the tip (see Fig. 1.3).

By definition, the summation is the local density of sample electronic states (LDOS), $\rho_{\mathrm{S}}(\overrightarrow{r_0}, E_{\mathrm{F}})$, at the Fermi-energy at the center of curvature of the tip

$$\rho_{\mathrm{S}}(\overrightarrow{r_0}, E_{\mathrm{F}}) \equiv \sum_{\nu} |\psi_{\nu}(\overrightarrow{r_0})|^2 \delta(E_{\nu} - E_{\mathrm{F}}). \tag{1.14}$$

Thus, constant current images correspond to contours of constant density of sample electronic states. This is used in the topographic imaging mode of STM.

1.1.3 Tunneling Spectroscopy

Bardeen's treatment provided a sound basis for interpretation of the experimentally observed scanning tunneling spectroscopy (STS). Now the tunneling current at a bias voltage eU applied between tip and sample can be evaluated by summing over all relevant states. At a finite temperature, the electrons in both electrodes (tip and sample) follow the Fermi distribution. With a bias voltage eU, the total tunneling current is

$$I = \frac{4\pi e}{\hbar} \int_{-\infty}^{\infty} [f(E_{\mathrm{F}} - eU + \epsilon) - f(E_{\mathrm{F}} + \epsilon)] \rho_{\mathrm{S}}(E_{\mathrm{F}} - eU + \epsilon) \rho_{\mathrm{T}}(E_{\mathrm{F}} + \epsilon) |M|^2 \mathrm{d}\epsilon, \tag{1.15}$$

where $f(E) = (1 + \exp[(E - E_{\mathrm{F}})/k_{\mathrm{B}}T])^{-1}$ is the Fermi distribution function. The quantities $\rho_{\mathrm{T}}(E)$ and $\rho_{\mathrm{S}}(E)$ are the density of states (DOS) of tip and sample.
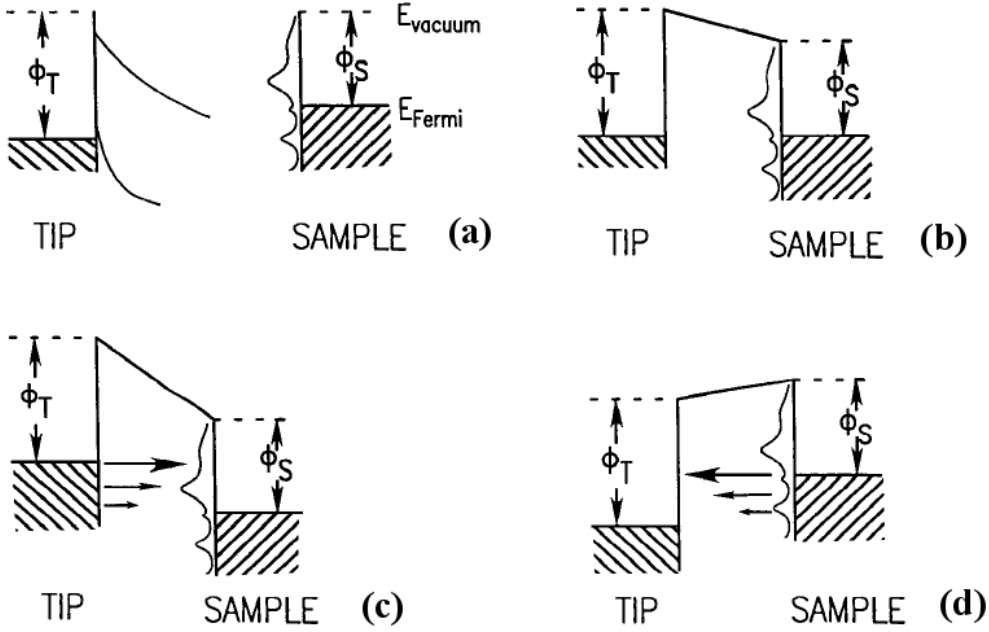
Figure 1.4: Energy level diagrams for different sample and tip levels. (a) Tip and sample are not in tunneling distance. (b) Tip and sample in tunneling distance, but in equilibrium separated by a small vacuum gap. (c) Positive sample bias: electrons tunnel from the tip to the sample. (d) Negative sample bias: electrons tunnel from the sample into the tip. Taken from [16].

If $k_B T$ is smaller than the energy resolution required in the measurement, then the Fermi distribution function can be approximated by a step function. In this case, the tunneling current is

$$I = \frac{4\pi e}{\hbar} \int_0^{eU} \rho_S(E_F - eU + \epsilon)\rho_T(E_F + \epsilon)|M|^2 \mathrm{d}\epsilon. \qquad (1.16)$$

It was further assumed by Bardeen, that the magnitude of the tunneling matrix element M does not change appreciably in the interval of interest. Then, the tunneling current is determined by the convolution of the DOS of tip and sample:

$$I \propto \int_0^{eU} \rho_S(E_F - eU + \epsilon)\rho_T(E_F + \epsilon)\mathrm{d}\epsilon. \qquad (1.17)$$

The electronic structures of tip and sample enter into Eq. 1.17 in a symmetric way. In other words, they are interchangeable. The DOS of the tip ρ_T and the DOS of the sample ρ_S contribute equally to the tunneling current I. For further clarification, a one-dimensional scheme is shown in Fig. 1.4. When the tip and the sample are independent (Fig. 1.4a), their vacuum levels are considered to be equal (dashed lines) and their respective Fermi energies, E_F, lie below the vacuum level by their respective work functions Φ_T and Φ_S. The wavefunctions decay energy-dependent into the vacuum, which is shown in Fig. 1.4a for two different states of the tip. If the tip and the sample are in the tunneling regime and in thermodynamic equilibrium, their Fermi levels must be equal (Fig. 1.4b). The effective potential

barrier is trapezoidal in shape but electrons can tunnel through if the barrier is sufficiently narrow.

When a voltage is applied to the sample, its energy levels will be rigidly shifted upward or downward in energy by the amount $|eU|$, depending on the polarity of the potential. At positive sample bias, electrons tunnel from the occupied states of the tip into unoccupied states of the sample (Fig. 1.4c). At a negative bias, the situation is reversed, and electrons tunnel from occupied states of the sample into unoccupied states of the tip (Fig. 1.4d).

If one assumes a tip with a constant DOS, the following relation can be derived from Eq. 1.17:

$$\frac{\mathrm{d}I}{\mathrm{d}U} \propto \rho_{\mathrm{S}}(E_{\mathrm{F}} - eU). \tag{1.18}$$

Therefore, the differential tunneling conductance $\mathrm{d}I/\mathrm{d}U(U)$ in this approximation is a direct representation of the DOS of the sample at the proximity of the tip at the energy $E_{\mathrm{F}} - eU$.

1.2   STM on Molecules

Studying molecules with STM already started in the late 1980s. The first molecule introduced was the copper phthalocyanine (CuPC) imaged by Gimzewski *et al.* [17] and Lippel *et al.* [18] with submolecular resolution. Even large molecules like DNA were investigated [19, 20] resolving the helix structure of the molecular entity. Also manipulation of molecules with STM became a hot topic from the very beginning, varying from simple pinning experiments done in solution [21], to more sophisticated approaches, e.g. rotation of molecular oxygen on Pt(111) [22] and building of molecular arrangements that can be imaged at room-temperature [23]. The electronic structure of molecules probed by STS was also first introduced for the example of phthalocyanines [24, 25]. The first states near the Fermi level were identified as HOMO (highest occupied molecular orbital) and LUMO (lowest unoccupied molecular orbital). Later, even probing the vibrational modes of certain molecular bonds was shown using vibrational spectroscopy [26]

Already in 1989 Spong *et al.* described a way to use the STM for distinguishing between different functional groups in organic molecules [27]. As mentioned above an alternative approach to conventional STM experiments was established using STM in liquids [28], imaging liquid crystals [29, 30] and chemical reactions. An example for the latter was shown recently by imaging the real-time oxidation process of porphyrin molecules [31]. This alternative of STM in solution is not further discussed, as all experiments in this thesis were done in UHV and at low temperatures. In the following, relevant publications which also deal with the main issues of this thesis are summarized.

The molecules investigated in chapters 5 and 6 exhibit chirality: in the first case already in the gas phase and in the second case induced by a conformational change on the surface. In 1998 Lopinski *et al.* showed for the first time the determination of the absolute chirality of butene molecules adsorbed on a silicon surface [32]. For

some molecules chirality is induced by a different conformation on the surface. Jung *et al.* showed the possibility to identify different conformational states of Cu-TBPP on various metallic surfaces [33]. A conformational change of a molecule on a surface can also lead to a change in chirality. This chiral switching was shown by Weigelt *et al.* by spontaneous conformational changes [34]. This issue concerning change of chirality induced by conformational switching is also covered in this thesis (see Sec. 6.2.2). Apart from conformational changes done with the STM tip, molecular manipulation became more and more sophisticated over the years, starting with controlled chemical reactions [35], multiple-step molecular switching [36] and moving molecules on the surface, including turning [37], rolling [38] and sliding [39]. A more destructive way is the controlled dehydrogenation of molecules. This was shown for CoPC molecules on Au(111) with a change in coupling between molecule and substrate [40] and the reversible control for methylaminocarbyne on Pt(111) [41]. In this thesis the controlled dehydrogenation of Co-Salen on Cu(111) is presented (Sec. 5.1.3). The reduced coupling between molecule and substrate mediated via an insulating adlayer makes it possible to probe molecular features otherwise quenched by the strong molecule-metal interaction. This was demonstrated by Qiu *et al.* for the Al_2O_3/NiAl(110) system probing vibrationally resolved fluorescence of ZnEtiol molecules [42], and by Repp *et al.* for the NaCl/Cu(111) studying the electronic structure of pentacene molecules [43]. The latter system is also used in this thesis (Sec. 5.4 and 6.4).

1.3   Magnetism of Molecules

The magnetism of molecules on surfaces is of great interest concerning various applications, e.g. in the field of magnetic storage devices. The methods of probing magnetic spins of adatoms and molecules on surfaces are divided into surface area averaging (electron spin resonance (ESR) and X-ray magnetic circular dichroism (XMCD)) and local techniques (spin-polarized STM (SP-STM) and magnetic exchange force microscopy (MExFM)).

1.3.1   Surface Averaging Techniques

For decades the only tool to grant access to the spin of materials was the electron spin resonance (ESR). The first ESR experiments on a single molecule were achieved in 1993 by Köhler *et al.* [44] and Wrachtrup *et al.* [45]. Their experiments detected the magnetic resonance transition of a single pentacene molecule in a *p*-terphenyl host crystal. Afterwards, ESR became a standard technique for chemists to investigate molecular states, but the detection of a single spin including spatial resolution is still missing.

In 2003 Gambardella *et al.* measured the magnetic anisotropy energy of ensembles of single cobalt atoms on a Pt(111) surface using X-ray magnetic circular dichroism (XMCD) [46]. Although they had access to the average values of orbital and spin moments, still the measurement was done by averaging over the surface area which comes with the technique of XMCD.

The magnetic coupling between the magnetic center ion of a molecule and the underlying substrate was demonstrated for the first time in 2005 by Scheybal *et al.* [47]. The magnetic interaction between a magnetized thin film cobalt substrate and adsorbed manganese(III)tetraphenylporphyrin chloride (MnTPPCl) molecules was studied by XMCD. This showed a ferromagnetic coupling between the manganese center atom and the cobalt film.

Recently, Wende *et al.* investigated the coupling mechanism of Octaethylporphyrin (OEP) Fe(III) chloride molecules to magnetic thin films of Co and Ni [48]. The two different ferromagnetic films were used for in-plane (Co) and out-of-plane (Ni) magnetization of the substrate. The chloride atom is removed from the molecules during preparation. Analysis of the XMCD signals from these two systems revealed a ferromagnetic coupling between the iron atom in the molecule and the ferromagnetic films. The authors presented an even more detailed model derived from DFT calculations of the Fe-porphyrin on the cobalt thin film. The exchange coupling mechanism of Fe-Co is not direct due to the absence of a direct hybridization between Fe and Co orbitals. The magnetic coupling is mediated via the nitrogen atoms in the porphyrin macrocycle.

1.3.2   Local Probe Achievements

The first pioneering attempt to detect the time-varying ESR component, e.g. the precession of individual spins with STM was performed in 1989 by Manassen *et al.* [49]. The next step after a long period of controversy over the work of Manassen was the introduction of an ESR-STM setup by Durkan and Welland [50]. They performed an experiment on the organic molecule BDPA, showing the large spin signal of the molecular radicals spatially resolved.

Probing the spin on the atomic level directly with lateral resolution and precision was shown recently by the two local methods with spin sensitivity, i.e. spin-polarized STM (SP-STM) and magnetic exchange force microscopy (MExFM). In the case of SP-STM, the magnetization and coupling of single isolated cobalt atoms on a Pt(111) surface were investigated [51]. Also the difference in coupling of iron and chromium atoms on Co/Cu(111) was demonstrated [52]. With force microscopy the limitation of STM to conductive samples is not given and therefore the spin-structure of the insulating NiO(001) surface could be resolved [53].

For a long time the only possibility to investigate the magnetism of (single) molecules on surfaces was the indirect probing of magnetic effects such as the Kondo effect. For single magnetic adatoms on surfaces the Kondo effect was investigated with STM for the first time in 1998 by Li *et al.* [54] and Madhavan *et al.* [55] and for single molecules in 2005 by Zhao *et al.* [40]. In the following years it was shown, that various aspects affect the coupling between magnetic molecules and substrate and therefore lead to variations in the Kondo signal. These studies concern molecular conformation [56], two-dimensional assembly [57] and quantum size effects of the substrate [58]. Just recently, the probing of the spin of individual CoPC molecules on Co/Cu(111) by SP-STM was achieved [59].

Chapter 2

Instrumentation

This chapter describes the construction of a scanning tunneling microscope operated at variable temperatures (VT-STM). It was designed for the purpose of preparation and investigation of molecular samples at temperatures ranging from low temperatures (20 K) to room temperature (300 K). After a short introduction into the complete setup, the molecule preparation and the setup of the microscope are discussed in more detail.
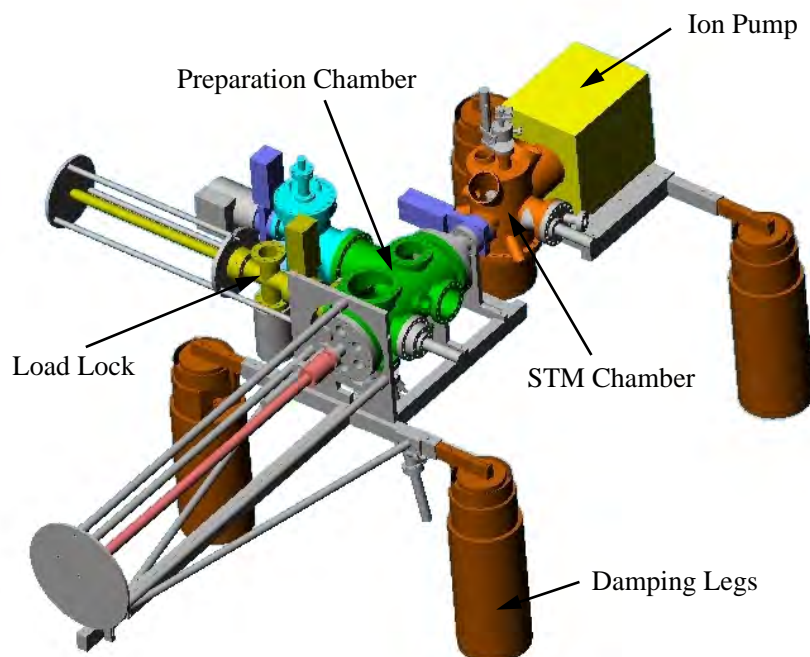
Figure 2.1: Setup of the vacuum system with three separate chambers for loading samples, sample preparation, and sample analysis. The complete setup is mounted on a rigid frame and is mechanically isolated from building vibrations via passive damping legs.
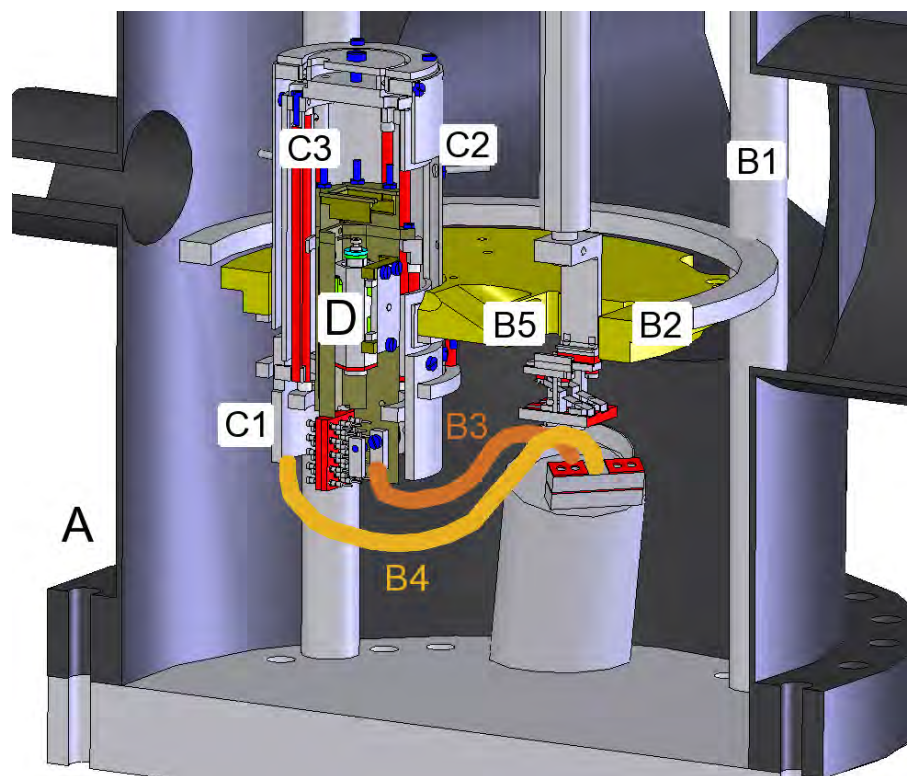
Figure 2.2: Schematic view into the STM chamber (A). Relevant parts are the damping and cooling stages (B1–B5), the housing of the thermal isolation (C1–C3), and the microscope body (D).

2.1 Vacuum System

The VT-STM is part of a vacuum system for the investigation of the temperature dependent growth of molecular systems on various surfaces. The experimental setup resides in a three chamber vacuum system (see Fig. 2.1): a load lock for the exchange of samples, tips, and evaporation materials, a preparation chamber for sample and tip cleaning i.e., argon ion etching and heating, and a STM chamber for the local characterization of molecular systems. Possible materials for evaporation range from metals (Fe, Co, Cr) and insulators (NaCl) to all kinds of volatile molecules. The materials are evaporated from Knudsen cells with flux control via the ion rate (for metals) and via a quartz microbalance (for molecules). Deposition of adlayers and molecules at room temperature and above takes place in the preparation chamber, whereas low temperature deposition takes place in the STM chamber with the sample stored in the cooled microscope head (see B5 in Fig. 2.2 and Sec. 2.2). The vacuum chambers are pumped via an ion getter, titanium sublimation, and turbo-molecular pumps with the base pressure maintained in the lower 10^{-10} mbar range. For mechanical stability and mechanical isolation the vacuum system is mounted on a rigid steel frame with additional, stabilizing frames for the transfer rods. The complete system rests on four pneumatic, passive damping legs.

Figure 2.2 gives a detailed insight into the STM chamber (A) including the components for damping (B1+B2), cooling (B3+B4), thermal isolation (C1–C3),

and the STM (D).

2.2   Damping, Cooling and Sample Preparation

This section covers the mechanical damping (B1 and B2 in Fig. 2.2), the cryostat (B3+B4), and the preparation of molecules on cold surfaces (B5).

The concept of the mechanical mounting is based on a commercial setup [60]. There, the STM head is fixed on a gold-plated platform. This platform has cut-outs for optical access and for the liquid helium flow cryostat and is connected via springs (B1) and an eddy current damping stage (B2) to the base flange. During sample and tip exchange the platform is fixed to a predefined position via a z-manipulator. During STM operation the platform is released and the sample is cooled from the side (above the platform).

In our system, some modifications were introduced to host a custom-made STM head and to permit deposition of molecules onto the cold sample. The base flange is a CF 250 flange with ports for electrical feedthroughs (three floating BNC and a 20 pin feedthrough), for the liquid helium flow cryostat, and for a z-manipulator to lock the platform during tip and sample exchange. The length of the springs to hold the platform is adjusted to the weight of our STM design. The liquid helium flow cryostat ends below the platform to enable effective cooling of the whole microscope and not only of the sample. The STM head is connected to the liquid helium cryostat via a short and flexible copper braid (B3). Additionally, to reduce the thermal load on the STM, a radiation shield is installed (see Sec. 2.3). The radiation shield is connected to a second flexible copper braid and cooled by the backflow line of the liquid helium flow cryostat (B4). A special cut-out is introduced into the platform opposite the STM for accommodating a home-built molecule evaporation stage (B5). With small mobile evaporators (see next section) it is possible to exchange the molecular material source *in situ*. This way, more than one kind of molecule can be evaporated on the same cold substrate (for details, see chapter 3). During evaporation with the shield of the STM left open, the temperature of the sample in the microscope head rises to 20 K when operated at the highest helium flux. Molecules from the evaporation stage impinge on the sample surface under an angle of 25°.

2.2.1   Mobile Evaporators

For an easy handling of molecules inside the UHV system and full control over the flux of molecules in both preparation stages (preparation and STM chamber), small mobile evaporators are used. The technical drawing of such a mobile evaporator is shown in Fig. 2.3. It consists of a base plate in the same dimensions as a sample holder with electrically isolated contacts going to a commercial heating plate and a copper head mounted on it. The evaporation material is filled in the bore of the copper head and is then put into the UHV system via the load lock. The evaporators can be grabbed by wobblestick at the handle and their transportation is identical to samples and tip shuttles through wobblesticks and transfer rods. There are two
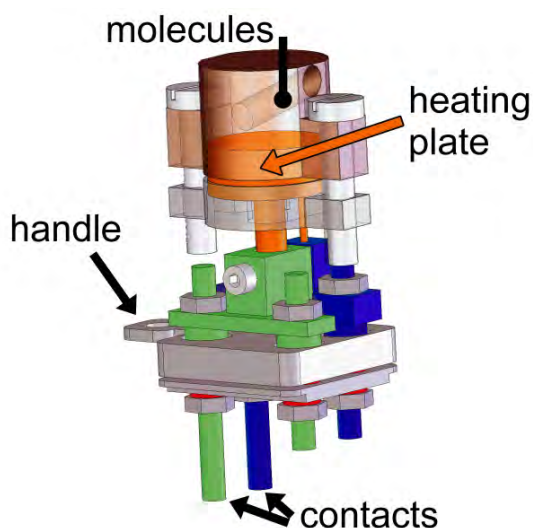
Figure 2.3: Technical drawing of a mobile evaporator. The base has the dimensions of a sample holder and can be grabbed by wobblesticks at the handle.

evaporation stages in the vacuum system to hold and connect the mobile evaporators, one in the preparation and one in the STM chamber. A current is fed through the contact rods from the evaporation stage, which is then heating the heating plate. It can easily reach temperatures up to 550 °C and more, which is enough for volatile molecules and also suitable for low temperature evaporation material, e.g. NaCl.

Therefore, using the microbalance molecular sources can be calibrated in the preparation chamber and then be transferred to the STM chamber for deposition onto the cold sample at a predetermined rate. In such a way it is also possible to exchange the molecular source *in situ* and deposit several different molecules one after another on the same cold sample inside the STM (see Sec. 3.2). It can be used for any type of volatile molecule with a vapor pressure below 10^{-10} mbar at room temperature.

2.3 Thermal Isolation

To maintain a low and stable temperature in the STM head, it is thermally decoupled from the room temperature environment. A helium back flow cooled housing (see C1 in Fig. 2.2) and a rotatable shutter (C2) for tip and sample exchange shield the STM head from thermal radiation. The housing is rigidly mounted to the inner STM head and the outer platform via a cascade of tubes with low thermal conductivity (C3). The final concept was selected after numerically modeling different designs.

2.3.1 Realization

Figure 2.4 (left) shows the supporting skeleton of the radiation shield. It consists of four layers of tubes and five stainless steel rings (I–V) interconnecting the tubes. The outer ring (I) fixes the skeleton to the eddy current damped platform at room
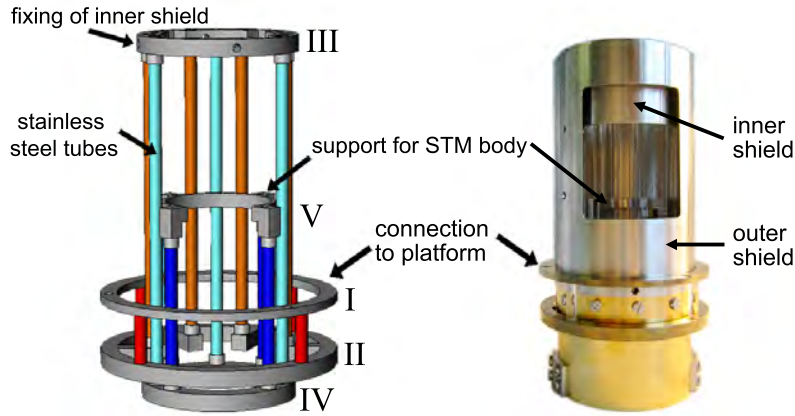
Figure 2.4: Left: The inner housing is a series of stainless steel tubes connecting the STM body with the damping platform and holds the radiation shield. Right: Photograph of the inner and outer housings. For protection against heat radiation, the outer housing consists of a cooled copper shield and a rotatable shutter.

temperature. The radiation shield (see Fig. 2.4, right) is mounted on ring III. The STM head itself is fixed to the innermost ring (V), whereas the other two rings (II and IV) give an additional extension of the tubes to increase the length of the heat dissipation paths.

Rings I and II are interconnected by four quartz rods ($\varnothing = 3$ mm). Quartz is an ideal material for thermal and electrical isolation but is also rather fragile. During tip and sample exchange, additional side forces appear, which limit the usage of quartz to short lengths. Therefore, for further thermal isolation the remaining skeleton is made of stainless steel tubes. The tubes are circularly arranged around the center for a high stiffness. To compensate for the increased heat conductivity, the wall thickness is reduced ($\varnothing = 3$ mm, $d_{\text{wall}} = 0.1$ mm).

As radiation shields, several stages are used. The inner shield (OFHC copper) is rigidly fixed at one end to ring III, whereas the opposite end is directly cooled through the helium back flow line. The inner shield has an opening to the front to grant direct access to the STM head. During STM operation, this hole is completely covered by the outer shutter. The outer stainless steel shield is sustained by a ball bearing for rotation and is *in situ* handled by a wobble stick.

2.3.2 Simulation

The choice of materials and dimensions of the different parts resulted from a numerical simulation of the heat dissipation within the system. The goal was to achieve a base temperature in the range of 15 K–20 K. As a boundary condition, the massive platform is assumed to stay constantly at room temperature. The cooling power of the liquid helium flow cryostat is given by the manufacturer (5 W) [61], the microscope body (see next section) is thermally highly conductive and the assumption of a constant, i.e., homogeneous temperature, is reasonable. The response of the housing on the cooling process is then described by an iterative approach. This additionally yields information on the time dependence of the cooling process.
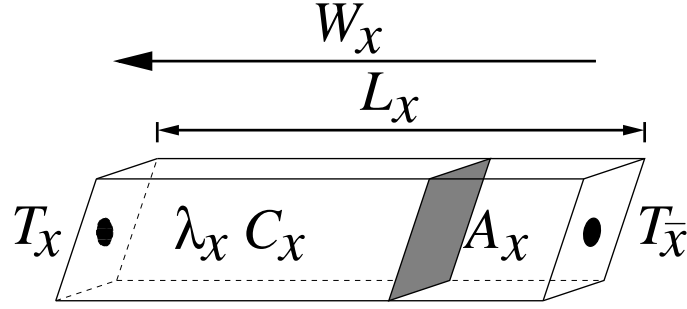
Figure 2.5: Each component of the housing is approximated by a part of length L and of surface area A. The heat conductance λ and capacity C depend on the properties of the material and vary with the temperature T of the part.

Starting with the whole system at room temperature, the cooling by the cryostat is switched on at time $i=0$. Then, the development of the temperature for each individual component of the setup is calculated up to an equilibrium state. This is illustrated in Fig. 2.5 for one idealized component x of length L_x and cross sectional area A_x. With a temperature gradient ΔT_x given between both ends $(T_x, T_{\bar{x}})$ this results in a net heat dissipation W_x. This heat dissipation reflects the temperature dependent material properties (heat conductance λ_x) whereas the resulting change in temperature reflects the ratio of heat dissipation and heat capacitance C_x. With the material properties known from standard literature [62, 63], we calculate the heat dissipation and the new temperature T_x^* after a time step Δi to be

$$W_x^{T_x, T_{\bar{x}}} = \frac{A_x}{L_x} \cdot \lambda_x(T_x, T_{\bar{x}})\Delta T_x \qquad \text{(heat dissipation)}, \qquad (2.1)$$

$$T_x^* = T_x + W_x^{T_x, T_{\bar{x}}} \cdot \frac{\Delta i}{C_x^{(T_x)}\Delta T_x} \qquad \text{(new temperature)}. \qquad (2.2)$$

Including contributions due to heat radiation ($\sim \mathrm{T}^4$), this approach was applied to the final design with the most relevant components schematically shown in Fig. 2.6. For simplification we introduced some approximations in the simulation: each component is described by its length and an average cross sectional area instead of its real geometry, i.e., with the exact positions of cut-outs and bores. Heat conductivity and heat capacity enter the calculation as homogeneous material properties, i.e., temperature gradients are neglected. Instead, for each step in the calculation, values for heat conductivity and heat capacity are taken for a mean temperature $((T_x + T_{\bar{x}})/2)$. Interface heat resistances between two linked components were treated in the limit of idealized contacts. The cooling power of the helium back flow line was unknown. Therefore, the same calculation was applied to two other similar VT-STM systems with known temperature behavior. The results of those calculations for the helium back flow line were handled as input parameters for the present calculation [64, **?**].

Figure 2.7 shows the results of this calculation (full line) along with the measured experimental data of the final setup (dashed line). Experimentally, the temperatures of the cryostat at the sample stage within the microscope body and at the inner

Figure 2.6: Schematic of the different stages connecting STM, shield, platform, and cooling braids. The two sources of heat load are heat flow ($\rightarrow$) from the platform and heat radiation ($\Rightarrow$).

shielding were measured in intervals of 5 min by silicon temperature diodes. Overall a convincing agreement between experimental and calculated temperatures is found.

20 min after the start of the cooling procedure the liquid helium cryostat is efficiently cooled down to approximately 30 K. The temperature load now only comes from parts of the microscope behind the cooling point of the cryostat. The slope of the time dependent temperature changes significantly in experiment as well as in the calculations (dashed and full black curves). The same effect can be observed after approximately 50 min in the curves related to the cryostat and to the sample stage (red curves). The microscope body reaches a temperature value of 25 K and the slope of both curves changes. The temperature of the inner shield still decreases for another 12 h (green lines).

In the calculations the time dependent temperature curve of the sample stage shows a pronounced kink at 100 K. This results from a drastic change of heat conductivity for copper with its approximation by a mean value. In reality the existing temperature gradient washes out this effect. Additional deviations between simulation and experiment (see Fig. 2.7) arise from the unknown interface heat resistance and the overestimation of the cooling power of the helium backflow line. After approximately 1 h, the base temperature of the sample stage of about 18 K is reached.

2.4 STM

The design of the STM head derives from the original design by Pan [65] and its further development at the University of Hamburg [66, 67]. The current version is optimized for use in a VT-STM system. To reduce the heat capacity and to minimize the surface area for thermal radiation, its size was reduced compared to the original

Figure 2.7: The cooling process as simulated and experimentally observed for different positions within the setup.

version.

Figure 2.8 shows three photographs of the homebuilt STM head: a back view (a) and views into the assembled microscope body with (b) and without (c) the scan unit. The body has a tube shape with a diameter of 24 mm.

The STM body consists of phosphor bronze, a material with low thermal conductivity, therefore acting as a damper against thermal fluctuations. Moreover, phosphor bronze is advantageous in terms of mechanical properties and its machinability compared to OFHC copper. For an effective and homogeneous cooling, the body is directly connected to a rigid thread made out of OFHC copper, which hosts the contact points for the cooling braids. A temperature diode is installed close to the sample stage with the wiring guided along the backside. At the bottom end a contact pad for electrical connections is mounted. Twenty-three commercial pin sockets are glued into a solid macor block. For maintenance, the electrical connections can easily be plugged and unplugged.

The front view (Figs. 2.8b and 2.8c) opens an insight into the assembled microscope. The sample stage is glued into the upper part of the body with nonconductive glue and is separately contacted with a miniature UHV compatible low-noise coaxial cable. The potential of the sample is defined by the voltage applied between the sample stage and the grounded body. Below the sample stage four piezowalker stacks for the coarse approach are visible. These stacks are completed by Al_2O_3 plates on top of each stack. Al_2O_3 is a hard material keeping the abrasion during operation of the coarse approach minimal. Polishing of the Al_2O_3 plates results in a very smooth and reproducible coarse movement.

The view in Fig. 2.8b shows the microscope body after adding the scan unit. The scan unit consists of a sapphire prism with the scanner tube mounted inside. It is a conventional five segment piezo tube with four outer segments for the *x-y-*
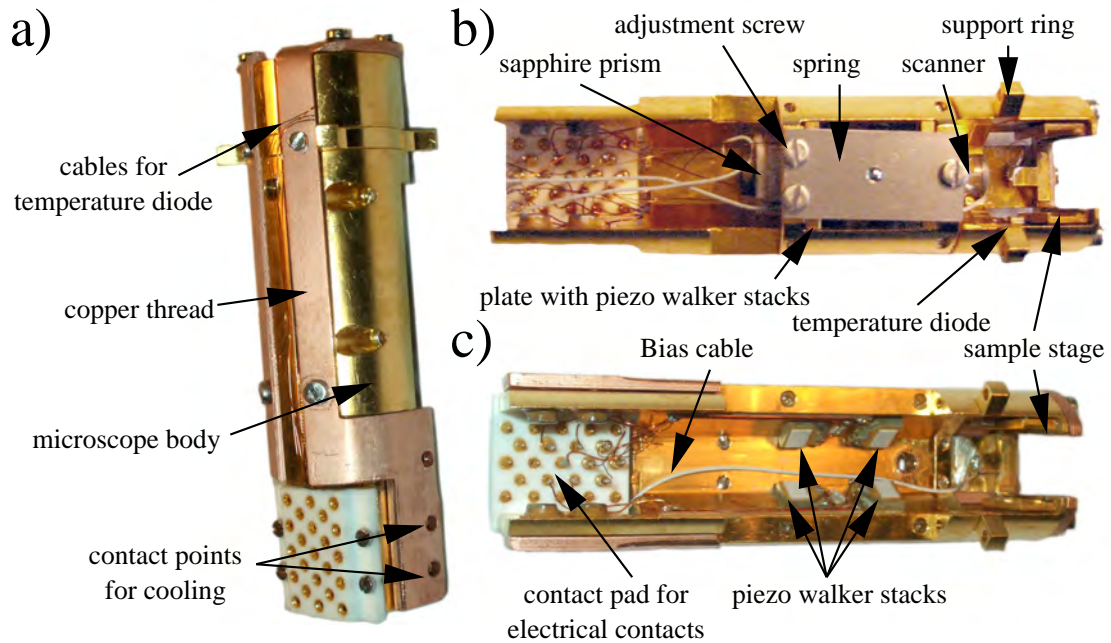
Figure 2.8: The body of the STM shown from the back (a) and the front [(b) and (c)]. It is made out of phosphor bronze with copper parts for homogeneous cooling power. The front view shows the STM after assembly with (b) and without the scan unit (c).

positioning and an inner segment for the z-positioning. For easy access, we use a wraparound electrode for the inner segment. Therefore, the contact point is below the sapphire prism and on the outer side. At the other end, the scanner tube extends beyond the sapphire prism and in case of failure, the x-y-z-cabling can be optically controlled and easily repaired. The sapphire prism rests on the four piezowalker stacks and is fixed in its position by a counter plate which hosts two more piezowalker stacks (hidden below the spring). The contact pressure between the sapphire prism and the six piezowalker stacks is controlled through the spring force. The spring force is adjusted by three adjustment screws. With optimized spring force, a reliable and reproducible approach speed within the full temperature range is achieved. The approach is operated at 1.5 kHz with a typical step size of $\sim$120 nm at room temperature and of $\sim$60 nm at 18 K. The travel distance accounts for $\sim$10 mm, which is sufficient for *in situ* tip exchange.

The STM is controlled via external electronics for temperature monitoring, the coarse approach, and the STM operation. Sensitive signals are the current I, the bias voltage V, and the high voltage for z-positioning (z). To minimize the electronic noise on these signals, the STM and the control units are electrically isolated from the electronics of the vacuum system. The current I is fed through a 1 kHz low-pass filter before entering the STM electronics to damp high frequencies, which are not important for the comparatively slow speed of measurements used on molecular samples.

We defined one common ground node at the back side of the STM control unit which is rigidly connected to the ground of the building by a thick, low ohmic copper

braid. The potential of the ground node serves as reference for all signals. To avoid the creation of a ground loop via the approach control unit, the approach piezos are electrically isolated from the control unit and grounded at the common ground node through a mechanical switch during STM operation.

Outside of the vacuum, conventional low-noise BNC cables are used for z, V, and I. On the vacuum side, UHV compatible low-noise coaxial cables are used. These cables have a small diameter, minimizing thermal conductivity. The shieldings of the sensitive signals are guided into the vacuum system via floating BNC feedthroughs with the ends of the shieldings left open at the microscope body. All other signals are transmitted *in situ* via unshielded and Kapton insulated copper wires and in air via a shielded BNC cable bundle. The electric potential of the STM body is defined by the common ground node with a direct connection to it. Further, ground connection through the cooling is prevented by thermally highly conductive but electrically insulating sapphire plates and the STM is electrically insulated from the chamber by quartz rods (see also Sec. 2.3).

Chapter 3

Preparation Techniques for Molecules on Surfaces

This chapter explains the preparation of molecular systems on different surfaces. Several molecular systems are studied at a coverage of a complete monolayer. This stabilizes molecules on a surface and makes measurements possible at room temperature or even in solution without an UHV environment. The preparation of such systems is quite unproblematic in terms of sample temperature and molecule rate. To prepare isolated molecules on a substrate such as NaCl/Cu(111), evaporation with a calibrated source on a precooled sample is inevitable. The capabilities of the vacuum system introduced in chapter 2 are described, but also the limitations of molecule preparation are discussed.

In the first section (3.1), different substrates and their properties are introduced. Section 3.2 deals with the comparison of preparation at room temperature and low temperature. In addition, the role of the NaCl adlayer thickness is explained. In Sec. 3.3, the important conditions for spectroscopy on molecules are discussed.

3.1 Substrates

To study the adsorption of molecules on surfaces, different substrates with well defined properties were selected. Typical substrates used for the study of molecules with STM are metal surfaces, such as gold, silver, and copper. In this study copper single crystals with two different crystallographic surface orientations were used: the (111) surface because of the surface state signature in the electronic structure and the (100) facet to have a square lattice with an increased atomic corrugation compared to the much denser packed (111) facet. Electronical decoupling of the molecule from the metallic substrate can be achieved by evaporation of insulating films. It is known from literature, that epitaxially grown thin films of NaCl exhibit (100) orientation starting from the first monolayer [68, 69]. These three template systems and their special properties are described in the following sections.

3.1.1   Equipment for Sample Preparation

The preparation chamber is equipped with a sputter gun and a heating stage for the cleaning process of copper single crystals. This is done in consecutive cycles of Ar^+ ion etching and annealing by heating to $\sim$900 K. After routine checks of the samples cleanness in the STM, admaterials are evaporated using mobile evaporators in the two evaporation stages, i.e., in the preparation or STM chamber.

3.1.2   Cu(111)

The (111) facet of copper is a well known system and intensively studied with STM for many years [70]. Experimental observation of the theoretically predicted Shockley type surface state [71] on the Cu(111) surface gained considerable interest in the STM community due to its two-dimensional nearly free electron gas behavior [72].
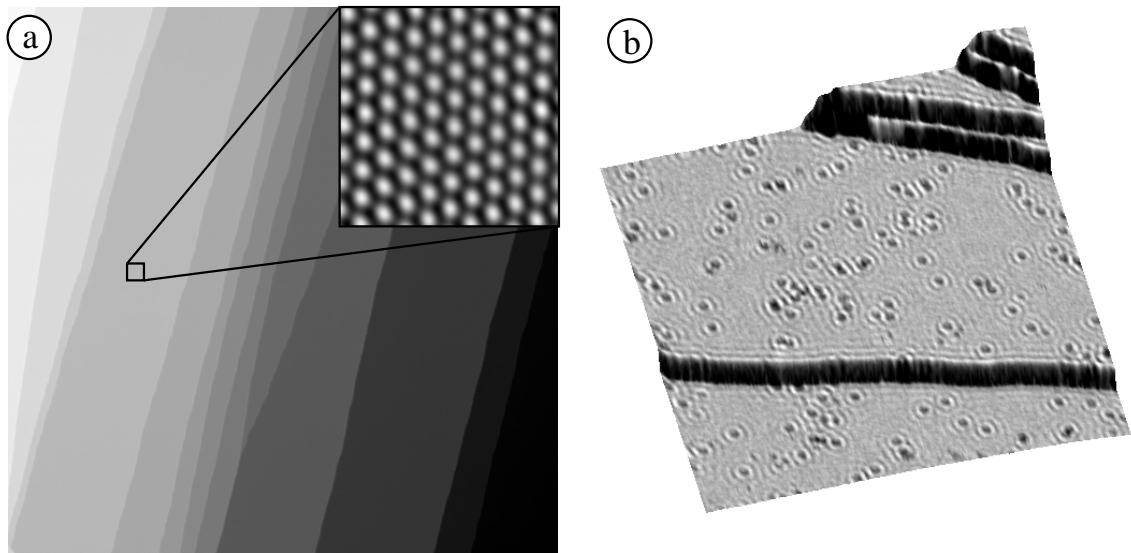
Figure 3.1: (a) STM topography image of a stepped Cu(111) surface (350 $\times$ 350 nm^2, $U = +300$ mV). Inset: Atomic resolution of the hexagonal lattice on a Cu(111) terrace (2 $\times$ 2 nm^2, $U = -50$ mV). (b) 3D representation of the measured height overlaid with the gray-scale map of differential conductance (dI/dU) (100 $\times$ 100 nm^2, $U = -250$ mV).

After cleaning the copper single crystal, the surface exhibits monoatomic steps with a step height of $\sim$209 pm$\pm$3 pm as shown in Fig. 3.1a. The inset shows a zoom-in on one terrace with atomic resolution. The sixfold symmetry of the (111)-lattice is clearly resolved with a nearest neighbor distance of $\sim$256 pm$\pm$5 pm.

Taking a map of the differential conductance (dI/dU) of the Cu(111) surface at energies above $U = -450$ mV reveals characteristic spatial oscillations due to the scattering of the surface electrons at step edges and defects. Figure 3.1b shows such a gray-scale dI/dU-map superimposed on the 3D representation of a constant-current topographic image. Oscillations decay with distance from scattering centers.
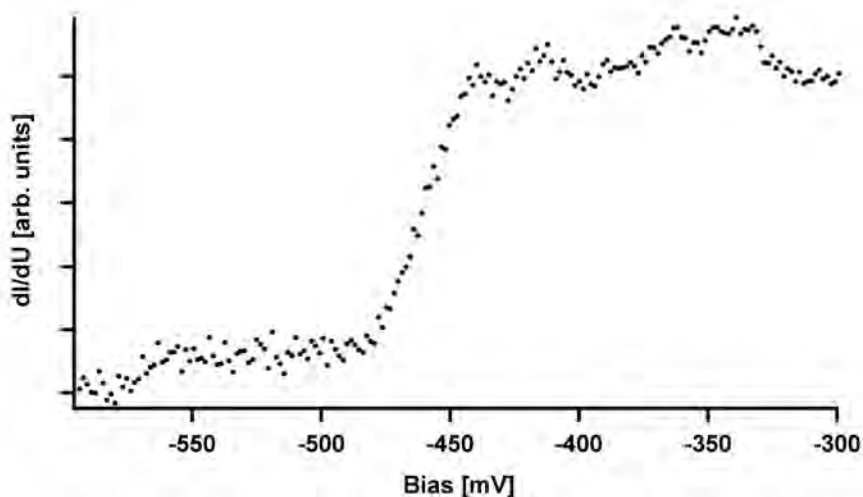
Figure 3.2: Point spectrum, i.e., differential conductivity vs voltage taken on a Cu(111) surface at least 5 nm away from any step edge and adsorbate. Average over ten spectra taken with Lock-In technique ($f = 1.777$ kHz, $V_{\mathrm{mod}} = 10$ mV)

The surface state is also visible in local point spectra taken on a clean copper terrace (see Fig. 3.2). In the given example, the voltage is ramped from $U = -600$ mV to $U = -300$ mV and the dI/dU-signal is recorded using a Lock-In amplifier ($f = 1.777$ kHz, $V_{\mathrm{mod}} = 10$ mV). At a bias voltage of $U \approx -450$ mV the signal reveals a steplike feature in the spectrum. This corresponds to an increase in the surface LDOS and is due to the onset of the surface state at this energy. The width of this feature is given by the electron lifetime of the surface state[73] combined with the thermal broadening of the system.

This feature in the spectroscopy is used as an indicator for the quality of the STM tip. The tip is treated by pulsing and dipping until the surface state is observed as the only feature in the curve. Therefore, before and after every spectroscopic measurement on molecules the tip status is appraised by taking a reference spectrum on the bare copper surface to exclude tip changes during acquisition.

3.1.3   Cu(100)

The Cu(100) surface was chosen as substrate for the comparison to the previously introduced (111) facet of copper. With copper maintained as material, the distinction of the (100) facet is the square atomic lattice and the absence of a surface state in the electronic structure. Figure 3.3 shows a STM image of an atomically resolved Cu(100) surface taken at 25 K. The slight distortion of the square lattice is caused by thermal drift.

The differences between these two facets of copper are important for the adsorption and growth behavior of molecules: the different geometries can induce different growth directions and the increased corrugation of the (100) lattice can influence the mobility of molecules on the surface.
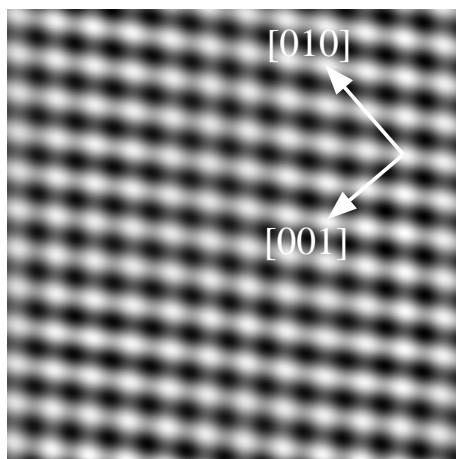
Figure 3.3: STM topograph of the Cu(100) atomic lattice. The two main crystal axes are marked by the white arrows (3×3 nm^2, $U = +30$ mV).

3.1.4 NaCl on Cu(111)

The growth of insulating materials on metals has been studied already for many years with different techniques including LEED, AFM, and STM [68, 69]. The system of ultra-thin films of sodium chloride on copper was introduced into the field of STM by Repp *et al.* to electronically decouple molecules [43, 74].

For a preparation at room temperature or above, NaCl is known to grow in the so called "carpet-mode" [75]. Islands with the (100)-facet and ~ 1 μm in size cover several copper terraces (see Fig. 3.4a). The NaCl island is colored in yellow for strong contrast with respect to the bare copper substrate. It starts with a bilayer and grows with additional monolayers. Due to the insulating character of NaCl adlayers, tunneling becomes more difficult with increasing thickness, but imaging up to 5 layers is reported [76].

Imaging single molecules deposited on such a bilayer system is already challenging in a bath cryostat system, but impossible with the VT-STM operated at 25 K (see Sec. 3.2). On the monolayer molecules are less mobile and can be probed also at 25 K. To achieve patches of only one monolayer in height, a different method is presented. NaCl is prepared with the copper substrate slightly below room temperature. The result of such an exemplary preparation is shown in Fig. 3.4b. The bilayer is still growing from one copper terrace to the next, but in addition a patch of the monolayer of NaCl is observed. The protrusions visible in the atomic resolution of both layers are assigned to the chloride atoms of the NaCl. This is suggested by theoretical [77] and experimental results [75, 78].

The strong mismatch between the hexagonal Cu(111) substrate with an atomic distance of 256 pm and the square NaCl(100) lattice with a Cl-Cl distance of 397 pm (unit cell of 562 pm) leads to a slightly disordered first layer (see inset in Fig. 3.4b with atomic resolution of the monolayer), which is similar to the Moiré patterns observed for the bilayer [76], but more pronounced in corrugation. The measured Cl-Cl distance is (404 ± 10)pm indicating a dislocation of the lattice. The bilayer (presented with atomic resolution) does not exhibit such disorder patterns. The layer
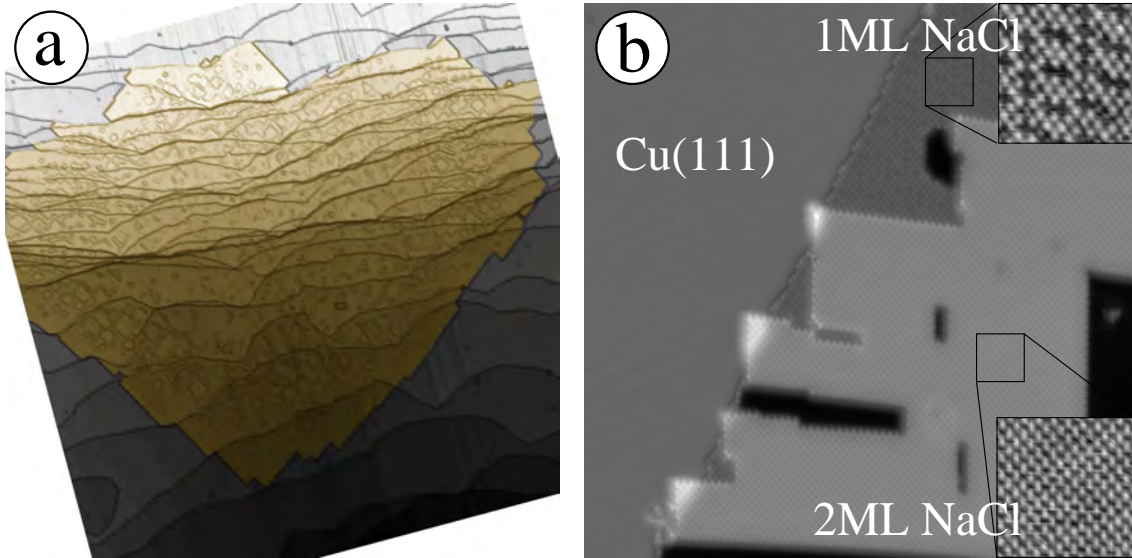
Figure 3.4: (a) Room temperature preparation of NaCl on Cu(111). The insulating adlayer forms large islands covering several copper terraces with an island size of $\sim$1 μm (1400 $\times$ 1400 nm^2, $U = +1000$ mV). (b) Deposition of NaCl on a Cu(111) surface slightly below room temperature. Instead of the typical bilayer islands also small parts of the monolayer are visible (40 $\times$ 40 nm^2, $U = +1250$ mV).

is fully relaxed which is reflected in the measured Cl-Cl distance of (394 ± 10)pm.

The apparent height of NaCl layers differs from the real height due to the insulating character of the medium. The tip has to approach further to the substrate to gain the same tunnel current in comparison to pure metal substrates. Therefore, the apparent height is reduced. The apparent height of the three first layers is measured as: 1 ML: (190 ± 10)pm; 2 ML: (320 ± 10)pm; 3 ML: (460 ± 10)pm.

The band structure of the clean copper surface is changed with an additional NaCl adlayer, leading to a shift in energy between the copper surface state and the interface state of the NaCl/Cu(111) system. Spectroscopy curves taken over different thicknesses of NaCl and on the clean copper are shown in Fig. 3.5. They reveal a shift in energy by comparing the spectra on copper and on NaCl/Cu(111), whereas the first and second monolayer of NaCl show the same onset in energy. This reveals the decoupling nature of the insulating adlayer already from the first monolayer of NaCl on copper.

Due to the energetic shift the wavelength deduced from the interference patterns on the surface are different on Cu(111) and on NaCl/Cu(111) at the same energy. A bilayer island of NaCl on Cu(111) is prepared and imaged with the topographic channel and the differential conductance recorded simultaneously (see Fig. 3.6a+b). The oscillations formed by the scattered surface electrons visualized in the dI/dU-map have different wavelengths on the NaCl island and on the clean copper. This is connected to the change in energy of the interface state on NaCl/Cu(111) derived from the band structure of the system [79].
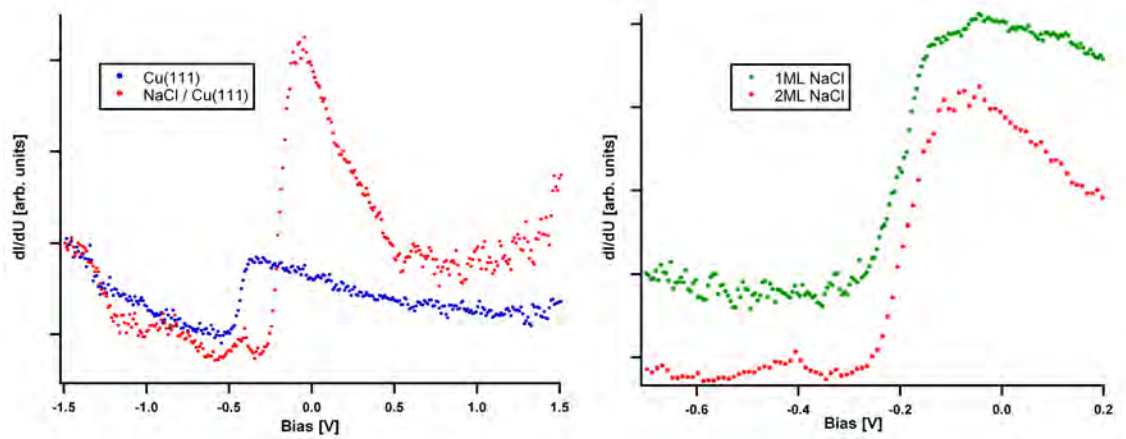
Figure 3.5: dI/dU-spectra taken over the clean copper surface (left, blue) and the NaCl/Cu(111) with a modulation-voltage of $V_{mod} = 10$ mV. The onset of the surface and interface state, respectively, is clearly visible. For the NaCl adlayer, the onset is shifted in energy from $U = (-450 \pm 10)$mV to $U = (-225 \pm 10)$mV due to the change in dispersion. Between the first and second layer of NaCl no additional shift is observed (right).
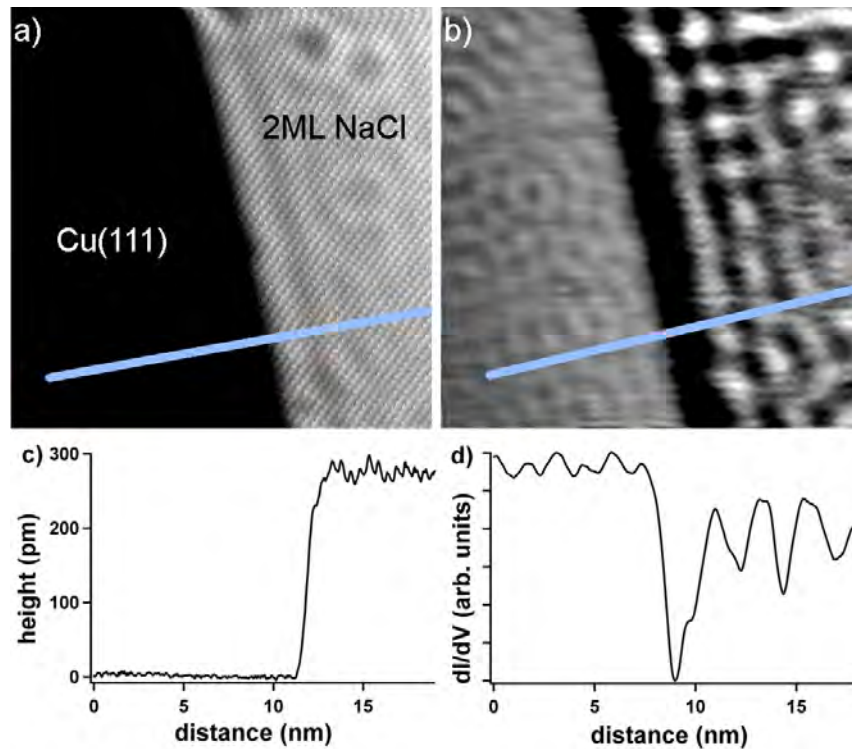
Figure 3.6: STM topograph (a) and simultaneously recorded dI/dU-map (b) of 2 ML NaCl on Cu(111). The energetic shift of the state from the clean copper to the NaCl island is observed in different wavelengths of the oscillations formed by the electrons on the surface (20×20 nm^2, $U = -75$ mV). (c)+(d) Associated line profiles indicated in (a) and (b).

3.2 Preparation of Molecules

The preparation of molecular samples depends as strongly on the quality of source material and substrate as on the system parameters during preparation. In the following, some of these challenges are discussed for the example of two well-known molecules, the phthalocyanine (PC) and tetra-phenyl-porphyrin (TPP) molecules. They are commonly used in STM, in the case of PC for nearly two decades, and are easily available due to their importance in industry as dye molecules or for the use in metal-organic hybrid systems. A short discussion is given, comparing the preparation of molecules from different sources, at different sample temperatures and on different materials.

3.2.1 Degassing of Molecular Material

The degassing of the molecular source is especially important for the use of commercial products. The purity is generally of the order of 90-95%. Remaining materials are often solvents or byproducts in the processing cycle and highly disturbing for measurements on individual molecules on surfaces. These remaining materials appear as additional adsorbates during the preparation and are therefore simply called dirt.

Figure 3.7a shows a STM image of a Cu(111) surface after preparation of FePC with the sample kept at room temperature. Only few FePC molecules are visible among and on top of dirt. Degassing the source for a few days slightly below the sublimation temperature of the desired molecule results in the removal of all materials from the source with lower sublimation temperature. After thoroughly degassing, preparation without adsorbates is feasible. This is demonstrated in Fig. 3.7b after
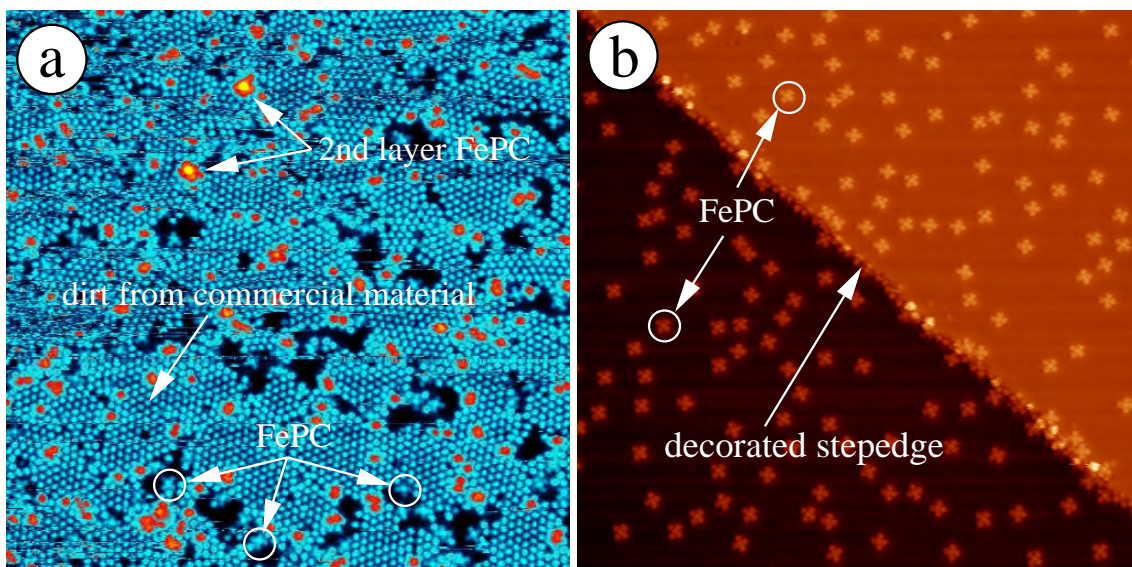
Figure 3.7: (a) Cu(111) surface covered mainly with dirt and a few FePC molecules (60×60 nm^2, $U = -300$ mV). (b) Image of a similar preparation after thoroughly degassing the molecular source (75×75 nm^2, $U = -225$ mV).

degassing the source. FePC molecules decorate step edges of the copper substrate due to their mobility at room temperature. The amount of dirt is significantly reduced and the investigation of individual molecules is possible.

3.2.2   Preparation on warm vs cold Surfaces

For most molecular species the mobility at room temperature is high enough to freely diffuse over the surface. This denies the possibility of room temperature investigation of individual molecules. In addition most of the molecular species form clusters and islands when prepared at room temperature, which then makes stable measurements with STM possible. To achieve a coverage with isolated molecules a preparation with a cooled sample is necessary. The impact of these two preparational conditions is presented in Fig. 3.8.

Two different types of porphyrin molecules with cobalt and copper as center ion are prepared on the same substrate. Figure 3.8a shows an image after room temperature preparation on Au(111). Molecules form a self-assembled island. Due to the different metal centers they are easily distinguished and it is observed that they are intermixing when co-evaporated on the same surface.

This is different when molecules are prepared on the same substrate with the sample kept at low temperature. The mobility of molecules on the surface is reduced and they stay isolated on the substrate (see Fig. 3.8b).

Using these two preparation conditions it is possible to prepare either isolated molecules, clusters or islands of molecules. Thus it is possible to study intramolecular
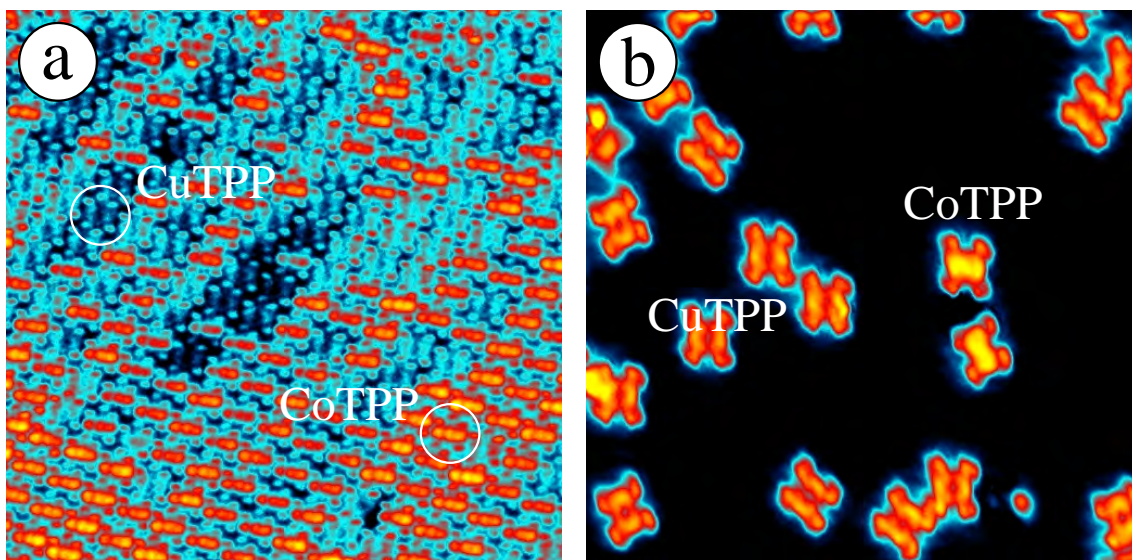
Figure 3.8: Co-evaporation of CoTPP and CuTPP molecules. (a) Room temperature preparation on Au(111). The two TPP species form an intermixed closed island structure, but due to their different appearance they are easily distinguished (20×20 nm^2, $U = +1200$ mV). (b) Deposition on a cold Cu(111) sample. The mobility of molecules is reduced and they stay isolated on the substrate (15×15 nm^2, $U = -800$ mV).

features of single molecules as well as intermolecular interactions of small clusters and molecular islands.

3.2.3   Molecules on NaCl

Insulating adlayers like sodium chloride are introduced as a spacer between the molecule and the metallic substrate to electronically decouple the molecule from the substrate and to prevent or reduce hybridization [43]. This reduced coupling makes the sample preparation and the measurements more challenging, due to the mobility of molecules on NaCl being further increased compared to the bare copper.

Figure 3.9 shows two cases of this increased mobility. FePC was prepared on NaCl/Cu(111) with the sample kept at room temperature (see Fig. 3.9a). The molecules are clearly identified on the copper surface, but the NaCl island is completely undecorated. Due to the low coupling of the molecules to the 2 ML high island of NaCl, they diffused onto the bare copper.

Even when the molecules are deposited on this substrate at low temperatures, some molecules are adsorbed on the NaCl, but are displaced by the tip during scanning (see Fig. 3.9b). The coupling between the two layers of NaCl and the FePC molecules is too weak to maintain a stable position. The influence of the tip is sufficient to drag the FePC molecules even with the tip further away ($U = -1700\,\mathrm{mV}$ and $I = 40\,\mathrm{pA}$). Therefore, the preparation of the monolayer of NaCl on Cu(111) was introduced, which is described in Sec. 3.1.4. The mobility of molecules on this monolayer is not as high as on the bilayer and measurements of individual molecules at 25 K are possible.

The same system of FePC/NaCl/Cu(111) was prepared with patches of the first
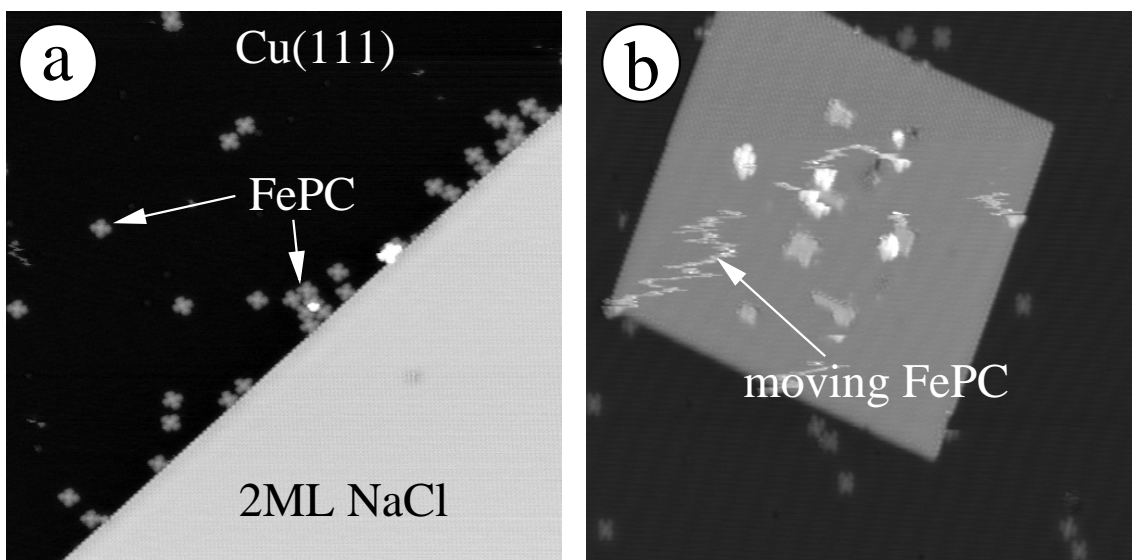
Figure 3.9: FePC molecules on 2 ML islands of NaCl/Cu(111). (a) Room temperature preparation ($60 \times 60\,\mathrm{nm}^2$, $U = -800\,\mathrm{mV}$). (b) Deposition of molecules on the cold sample. Molecules are observed on the NaCl island, but are highly mobile ($50 \times 50\,\mathrm{nm}^2$, $U = -1700\,\mathrm{mV}$).
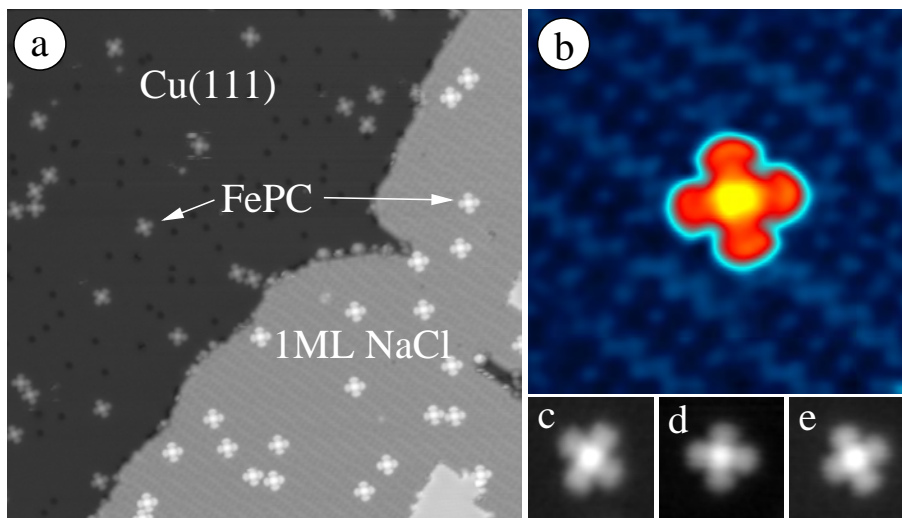
Figure 3.10: FePC prepared on monolayer patches of NaCl on Cu(111) with the
sample kept at 30 K. (a) Individual FePC molecules are recognized on the copper
terrace as well as on the first monolayer of NaCl (60×60 nm^2). (b) Zoom-in on
a single FePC on 1 ML NaCl. The Moiré pattern of the NaCl lattice is nicely
resolved (7×7 nm^2) (c)-(e) Cut-outs of single FePC molecules from (a) showing
three different orientations on the hexagonal substrate of Cu(111) (4×4 mm^2). All
images obtained with $U = -1000$ mV.

layer of NaCl available and is shown in Fig. 3.10. Isolated FePC molecules are
observed on the copper and on the NaCl island (Fig. 3.10a). They are now immobile
during imaging even with the atomic resolution (mixed with a strong Moiré pattern)
of the NaCl island clearly resolved (Fig. 3.10b). Only one orientation of FePC on
NaCl is found in contrast to three orientations of FePC on Cu(111), which are shown
in Fig. 3.10c-e.

3.3   Spectroscopy on Molecules

There are different ways to probe the electronic states or electron density of the
sample with STM. The two techniques used for the molecular samples in this thesis
are local point spectroscopy and maps of differential conductance (dI/dU-maps).
They are explained in detail in the two following sections.

3.3.1   Point Spectroscopy Curves

In Sec. 1.1.3 the relation between the local density of states (LDOS) directly below
the STM tip and the derivative of the tunneling current with respect to the applied
voltage was explained. This dependence is used to probe the LDOS of the sample
by taking the current and its derivative with varying bias voltage. In this point
spectroscopy mode the STM tip is first positioned over the point of interest on the
sample. The feedback-loop is opened keeping the tip at a constant height (depending
on the thermal z-drift of the system) and during the ramping of the bias voltage,
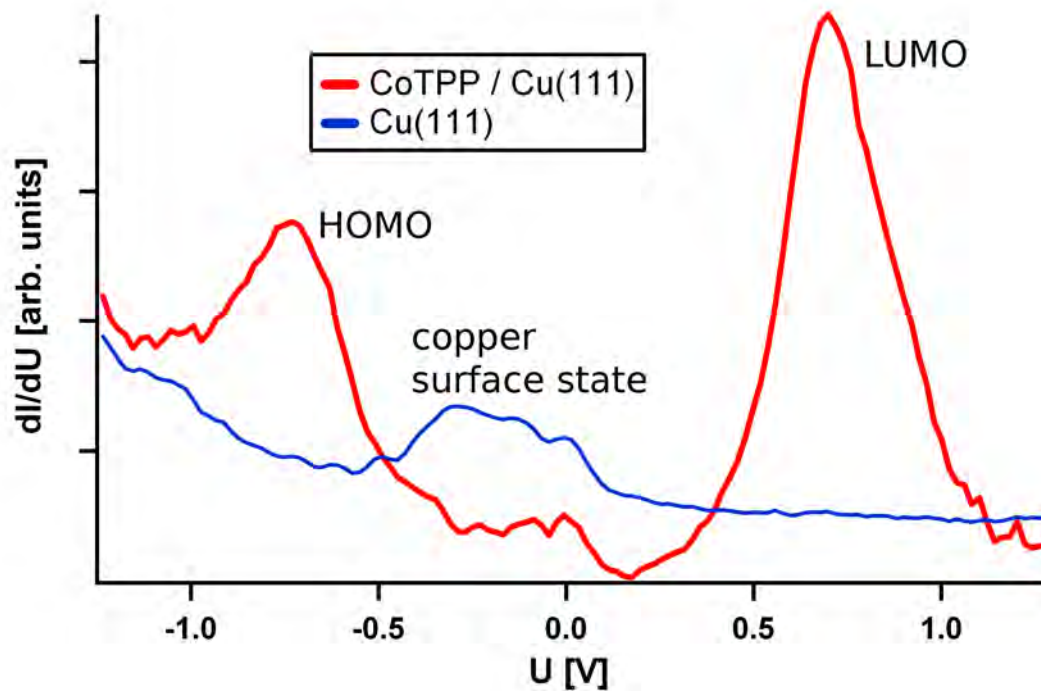
Figure 3.11: Spectroscopy curves taken over the center of a CoTPP molecule on a Cu(111) surface and on the clean copper as reference. The surface state is observed in the copper spectrum (blue); in the spectrum taken over the CoTPP molecule, two peaks due to molecular states (HOMO and LUMO) are identified (red).

the current is recorded. For the derivative of the current (dI/dU) the current is fed through a lock-in amplifier and the first derivative from the output is also logged. Spectroscopy curves taken in this way are presented in Fig. 3.11.

The red curve is taken over the center of a CoTPP molecule on a Cu(111) surface. For comparison and as a reference for the tip quality, another spectroscopy curve is taken on the clean copper (blue curve). These reference curves of the substrate are taken some nanometers away from any molecule, other adsorbate, or defect. The parameters of the lock-in amplifier were always $f = 1.777$ kHz and $V_{mod} = 15$ mV when not stated differently. The axis of the dI/dU-signal is mapped in arbitrary units.

In the blue curve, the surface state of the Cu(111) substrate is observed. The red curve of the molecule exhibits two huge maxima. These are usually referred to as HOMO (highest occupied molecular orbital, left peak below the Fermi energy) and LUMO (lowest unoccupied molecular orbital, right peak above the Fermi energy), although keeping in mind that the observed states are not the pristine molecular states from the molecule but a hybridized combination of molecular and copper states.

3.3.2   dI/dU-maps

Another way of probing the dI/dU-signal with spatial resolution is the map of differential conductance or dI/dU-map. The current is again fed through a lock-in amplifier and the first derivative is recorded during the scan of the sample. This is shown as an example for two different porphyrin molecules prepared on a Cu(111) surface.
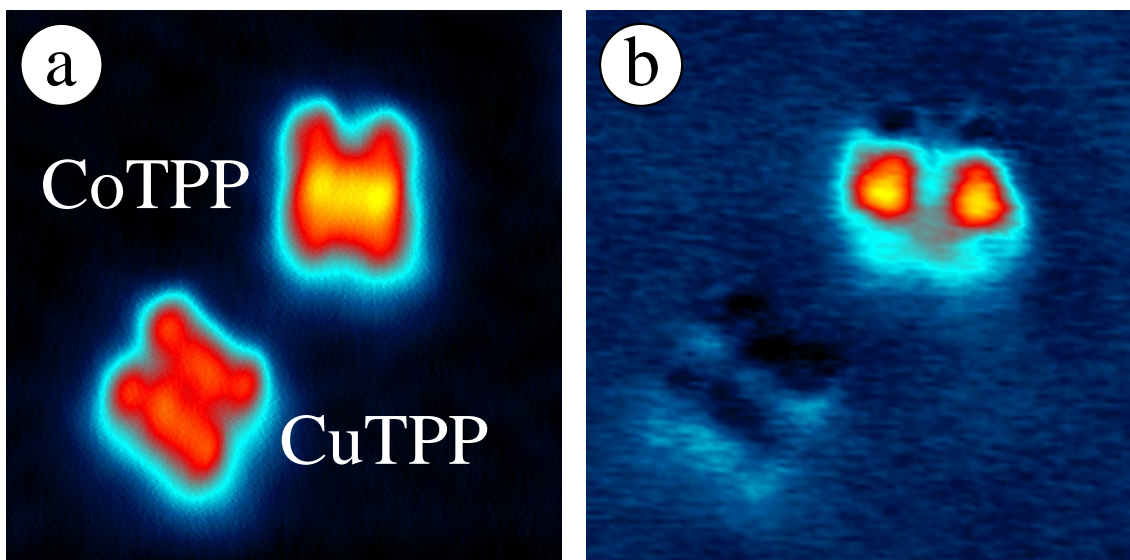
Figure 3.12: CuTPP and CoTPP molecule on a Cu(111) surface illustrated with the (a) topographic and (b) differential conductance channel (6 × 6 mm^2, $U = -750$ mV).

Figure 3.12 shows the two different channels of the same sample area recorded at the same time. In Fig. 3.12a the topographic channel is shown. The two different TPP molecules with cobalt and copper as metallic center ions are clearly identified: The CuTPP shows a pronounced minimum at the center, whereas the CoTPP shows an elevated backbone with constant height.

In the channel of differential conductance, the discrepancy between the two molecules is even more drastic: the CoTPP molecule has two round maxima at the position of the bent-up pyrrolic units of the saddle backbone. This molecular orbital corresponds to the maximum at $U \approx -750$ mV observed in the point spectroscopy curve of Fig. 3.11. The map of differential conductance now shows this molecular orbital spatially distributed over the molecule. This observation is consistent with literature [80].

The CuTPP molecule remains dark in the dI/dU-map with no observable feature at this energy. This is consistent with the point spectroscopy of this molecule (not shown).

This shows the possibility of probing the spatial distribution of the density of states also on molecule-metal systems.

Part II

STM Experiments on Individual Molecules

Chapter 4

Symmetry Effects of Metal Phthalocyanines on Copper Surfaces

Imaging of Metal Phthalocyanines (MPCs) and of their intramolecular structures by STM was first achieved by Gimzewski *et al.* [17] and Lippel *et al.* [18] under UHV condition. Until now, many MPCs (M = Cu [17, 18, 81, 82], Co [40, 59, 83, 84], Fe [85–90], Ni [87], Pd [91], Zn [92], Mn [58]) have been studied on various surfaces: they adsorb on surfaces in a planar configuration and exhibit four-lobed cross shapes in STM images, which are consistent with their molecular structures (see Fig. 4.1). The metallic centers appear either as a dip or as a protrusion in STM images depending on the electronic structure of the central metal ion, i.e., the energy of the d_{z^2} orbital with respect to the Fermi level [87]. For larger ionic sizes of metallic centers of MPCs, such as SnPC, the metallic ion sticks out of the molecular plane resulting in a nonplanar configuration on surfaces [93, 94]. For the growth behavior on metallic surfaces Cu, Au, Ag, and graphite, no ordered structures are found at low coverages. With increasing coverage, ordered molecular domains start to appear and form a complete molecular monolayer before the formation of the second molecular layer [85, 87, 89–92, 94]. Upon further increase of coverage, self-assembling in higher layers can be observed with the molecular plane parallel [95] or tilted [85, 89] towards the surface plane.

In the low-coverage regime, many physical properties of isolated MPCs on metallic substrates are dominated by the molecule-substrate interaction. For instance, MPCs with a magnetic center, such as Fe, Co or Mn, adsorbed on nonmagnetic substrates are highly fascinating, as spin-scattering processes are manifested as a Kondo resonance in STS and thereby reflecting molecule-substrate interactions and molecular excitations [58, 83, 86]. The distance between magnetic centers of MPCs and substrate [40, 59] as well as the exact adsorption site [86] were found to strongly modify the Kondo temperature. For metallic substrates, three orientations of FePCs have been reported for the adsorption on Cu(111) [85] and Au(111) [86] in the sub-monolayer regime, which are directly attributed to the substrate symmetry. Low-energy electron diffraction (LEED) observations exhibited two orientations for CuPCs and FePCs on Cu(100) of $\pm 22.5°$ relative to the $\langle 001 \rangle$ directions [96]. Later,

M=Cu, Co, Fe
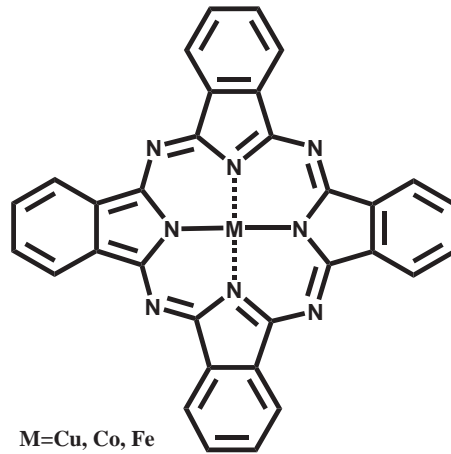
Figure 4.1: Molecular structure of a phthalocyanine molecule with a metal ion in the center position exhibiting a four-lobe cross shape. In this study Cu, Co, and Fe were used as metallic centers.

this was reconfirmed by STM experiments on CuPC on Cu(100) [18]. In addition, one metastable configuration of FePC is reported to occur when FePC is adsorbed on Au(111) [86].

However, in the above experiments molecules were evaporated onto surfaces being held either at room temperature or above and therefore, MPCs adsorbed in stable configurations. It remains an open question whether there are more metastable configurations, which might have different properties than stable ones when adsorbed on surfaces at low temperatures. In addition, the adsorption of fourfold symmetric MPCs on substrates with commensurate and incommensurate symmetries, as Cu(100) and Cu(111), respectively, can provide a valuable contribution to the understanding of molecule-substrate interactions.

In this study three kinds of MPCs (M = Cu, Co, and Fe) were used [97]. The powder was thoroughly degassed as described in Sec. 3.2.1. All molecules were prepared at low temperatures (20 K–35 K).

4.1 Meta-stable Configurations of Metal Phthalocyanines on Cu(100)

Figure 4.2a shows a STM image of a stepped Cu(100) surface with adsorbed CoPCs. CoPCs are arbitrarily distributed but copper steps remain undecorated, which is typical for a low temperature preparation. Four different adsorption orientations are identified. For each orientation, enlarged images of representative CoPCs are plotted in Fig. 4.2b. CoPCs appear in their characteristic four-lobe structure with a bright center similar to those adsorbed on other metals [40, 59, 83, 84]. This suggests a planar structure. With a closer inspection, the molecular axes of configuration 3 are found to be parallel with the crystallographic axes of Cu(100). The molecular axes of configurations 1 and 2 are rotated by $\sim \pm 22°$ and of configuration 4 by $\sim \pm 45°$ with respect to configuration 3 and to the crystallographic axes, respec-
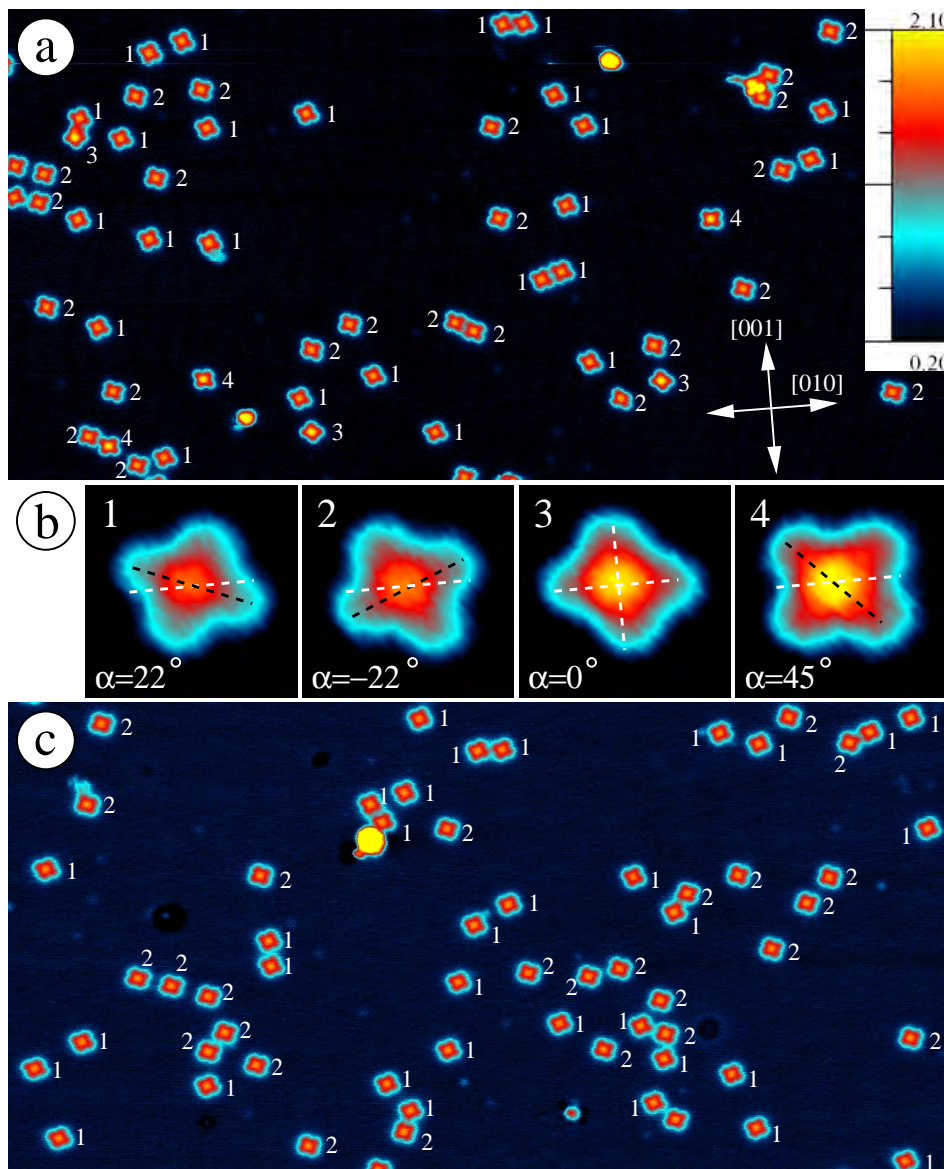
Figure 4.2: STM images of CoPC on Cu(100) prepared at 29 K (a) and after post annealing to room temperature (c) (60×30 nm^2, $U = -1200$ mV). (b) Magnifications of four different orientations as marked in (a) with 1–4 (3×3 nm^2). In (a), a set of arrows reflects the crystallographic axes of Cu(100) as determined from the clean surface. In (b) one crystallographic axis (white dashed line) and one molecular axis (black dashed line) are indicated.

tively. Relative frequencies of molecular configurations clearly manifest two groups of distributions as shown in Fig. 4.3: orientations 1 and 2 ($\sim 87\%$) significantly dominate over orientations 3 and 4 ($\sim 13\%$). Within each group different orientations have almost identical appearing rates. Within the limits of statistical significance, an identical distribution of molecular orientations can be found for FePc and CuPC on Cu(100) (see Fig. 4.3).

The observation of four different orientations of CuPC, CoPC, and FePC on
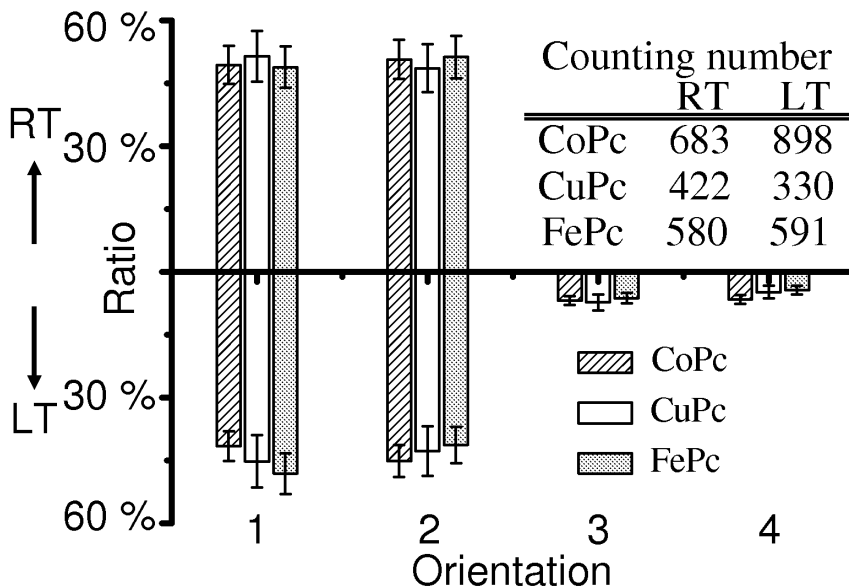
Figure 4.3: Relative frequencies of adsorption orientations for CoPCs, CuPCs, and FePCs on Cu(100) after preparation at room temperature (RT) and at low temperature (LT). The statistical error is indicated.

Cu(100) is in apparent disagreement with previous findings for CuPC and FePC on Cu(100) [18, 96]. In previous findings, after room temperature preparation STM and LEED data reveal an alignment of MPCs in only two orientations ($\pm 22.5°$) which are in agreement with orientations 1 and 2 in this study. The disagreement suggests a decisive temperature effect. To test the influence of preparation temperature, samples were annealed to room temperature and the resulting surface structures were compared to those of samples after room temperature preparation. In both cases the observable orientations are reduced to the previously reported orientations. This is demonstrated in Figs. 4.2c and 4.3. As a consequence orientations 3 and 4 have to be assigned to meta-stable configurations.

Under the given scanning conditions ($U \leq 2000$ mV, $I \leq 300$ pA) the appearances of benzene groups of MPCs are identical as shown in the line profiles crossing MPCs in stable and meta-stable configurations (Fig. 4.4b). However, the apparent height at the metallic centers varies significantly with the configuration of MPCs. In Figs. 4.2 and 4.4b a pronounced center is observed for CoPCs in meta-stable configurations at $U = -1200$ mV ($\Delta z \sim 0.25$ Å). The effect is more pronounced for FePCs (see Figs. 4.4a+b) but is not observed for CuPCs.

4.2 Symmetry Reduction of Metal Phthalocyanines on Cu(111)

In another experiment, the growth of fourfold symmetric MPCs on the sixfold symmetric surface of Cu(111) was investigated in order to find the fingerprint of the
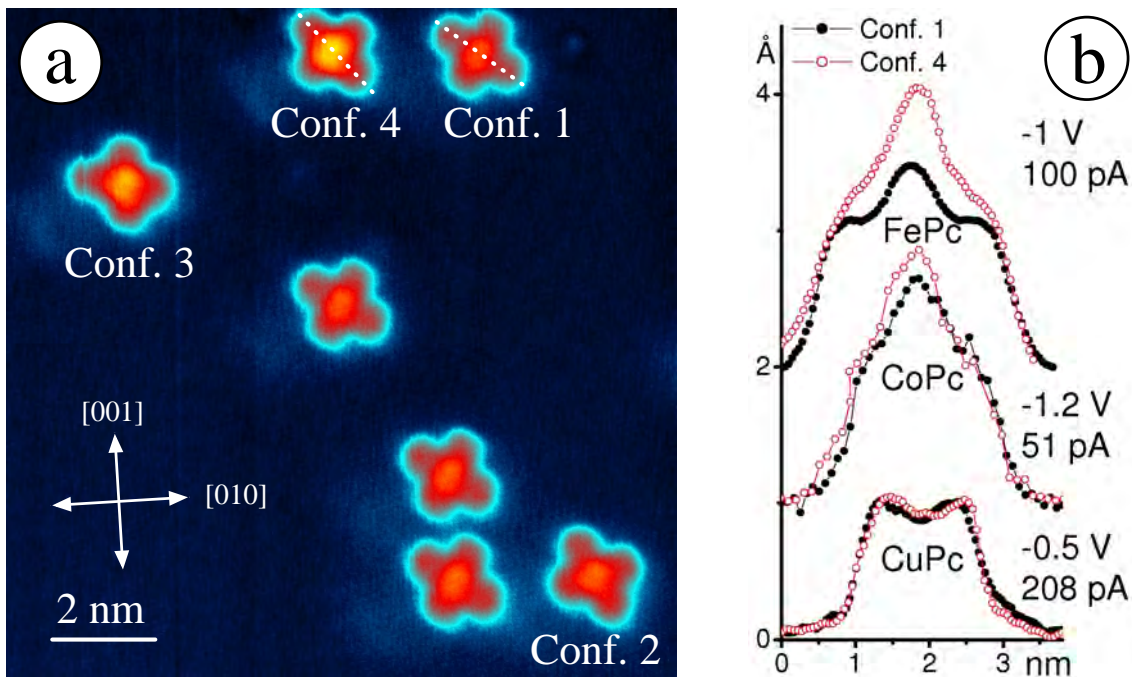
Figure 4.4: (a) STM image of FePCs on Cu(100) prepared at low temperature. (b) Line profiles crossing configurations 1 and 4 of FePC, CoPC, and CuPC. For each pair of line profiles identical tips were used.

incommensurate symmetries. To study intramolecular details, Fig. 4.5a gives an enlarged view of CoPCs adsorbed on Cu(111). At the given voltage, CoPCs evolve as parallelograms with one axis pronounced and a second perpendicular axis appearing at reduced apparent height. For all molecules, this second axis is perfectly aligned to one of the closed-packed directions of the substrate, i.e., CoPCs in three different orientations are present, independent of the preparation temperature.

The appearance of PC molecules in STM images depends on the molecular states involved in the tunneling process, i.e., on the applied bias voltage as well as on the molecular center. The evolution of molecular appearances is depicted in Figs. 4.5b-d for CoPC, CuPC, and FePC at representative bias voltages. Instead of sharp transitions with bias, a gradual change can be observed. This is indicative for a strong hybridization of molecular and substrate states [18, 43, 98]. For FePC and CoPC, the center appears as a protrusion in the topography for all bias voltages between $U = 1500$ mV and $U = +400$ mV. This effect is attributed to the half filled d_{z^2} state [87]. For MPCs with higher atomic numbers for the central ion, e.g., CuPC, this d_{z^2} state is filled with two electrons. As a consequence this state shifts at least 2 eV below the ligand HOMO, creating a large interval with no significant contribution from the d-orbital around the Fermi energy as calculated by Rosa *et al.* [99]. Within the studied energy range the only hint for the d_{z^2} state of CuPC was observed starting at $U = +1500$ mV (see Fig. 4.5c). Instead, for CuPC a strong symmetry-reduction results in two pronounced protrusions at the sites of the benzene rings. A symmetry reduction of similar intensity can be observed for CoPC as long as contributions of the d_{z^2} state to the tunneling process do not become

−1500 mV   −250 mV   +250 mV   +1500 mV
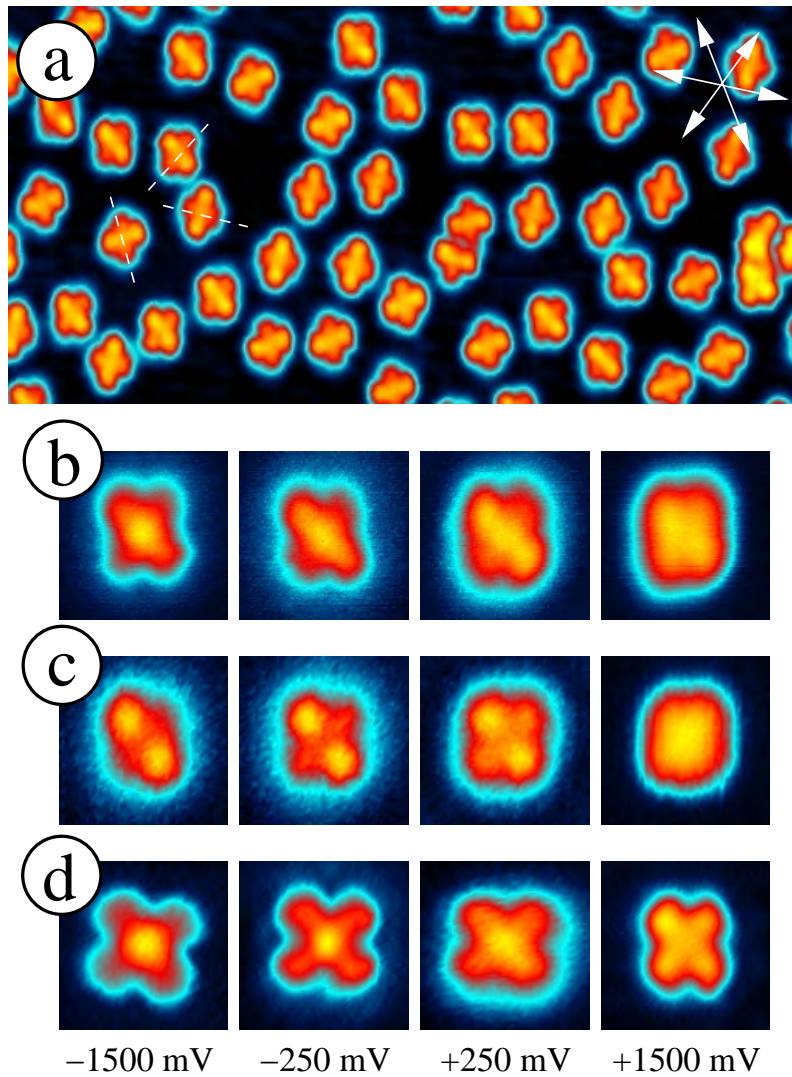
Figure 4.5: STM images of CoPC (a)+(b), CuPC (c), and FePC (d) on Cu(111). In (a), for each of the three orientations of CoPCs, the molecular axis of one molecule which appears at reduced apparent height is marked by a white dashed line. These axes are parallel to one of the three crystallographic axes determined from atomically resolved images of the bare Cu(111) substrate. (b-d): 3×3 nm^2.

dominant. For FePC the symmetry reduction is nearly lifted but faintly present (see also Ref. [85]).

So far, the origin of the observed symmetry reduction of molecular structure (which is present for all MPCs studied) remains unclear. The incommensurability of molecular and surface symmetries results in a different atomic configuration underneath two perpendicular molecular axes. Therefore, electronic effects, due to the atomic structure underneath, and geometric effects, due to a structural deformation, have to be considered since STM does not distinguish between them. Indeed, indications for such a geometrically driven reduction of symmetry can be found. Although MPCs on Cu(100) can be found in four different orientations with three different molecule-substrate configurations (orientations 1 and 2 are mirror symmet-

ric), indications for a substrate-induced effect are not found in STM images and the benzene groups appear identical for all molecular orientations within the experimental accuracy (Fig. 4.4b). We conclude that the driving contribution of the observed symmetry reduction is a vertical bending along one of the molecular axes. As a consequence of the reduced molecular symmetry the degeneracy of molecular states is partially lifted. This is manifested as a strongly bias-voltage-dependent symmetry of molecular appearances (Figs. 4.5b-d).

Chapter 5

Co-Salen

The complex of N,N'-1,2-Ethylenebis(salicylideniminato)-cobalt(II), referred to as Co-Salen in the following is one of the first cobalt complexes reported to coordinate molecular oxygen [100] and is used in numerous applications in material chemistry and transition metal catalysis [101–110]. The molecular structure of a Co-Salen molecule is depicted in Fig. 5.1. The metal center is surrounded in the complex by two nitrogen and two oxygen donor atoms, which can lead to complexes in quite high oxidization states. The hydrogen atoms in the 5,5'-positions (marked by X) of the simple Co-Salen are easily substituted by CH_3, F, Cl, Br, I, NO_2, etc. via the respective salicylaldehyde precursor.

The first derivative of the Co(5,5-X_2-Salen) molecules (X = H, CH_3, and Cl) used in this work is the simple Co-Salen with hydrogen in the 5,5'-positions. All Salen molecules used were supplied by the chemistry group of Prof. M. Prosenc in Hamburg. Results of DFT calculations of the optimized structure of the free Co-Salen molecule performed by M. Prosenc *et al.* are shown in Fig. 5.2. The side view (Fig. 5.2b) clarifies a C_2 symmetry due to a deformation of the C_2H_4-bridge which implies chirality. The bridge is tilted into the third dimension with one of the four bridge hydrogens pointing up and one down relative to the molecular plane (Fig. 5.2c).

X=H, CH₃, Cl
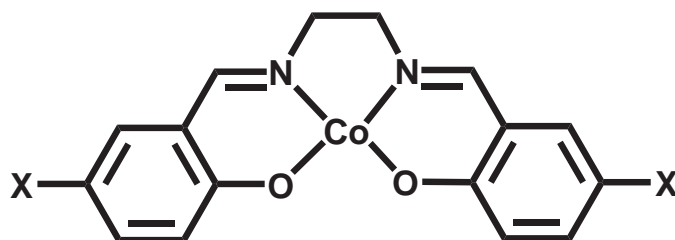
Figure 5.1: Molecular structure of a Co-Salen molecule. In the 5,5'-positions (marked by X) substituents are easily exchanged. These can range from halogens (Br, F, Cl, etc.) to small functional groups (CH_3, NO_2, etc.). The substituents used in this study are hydrogen, CH_3, and Cl.
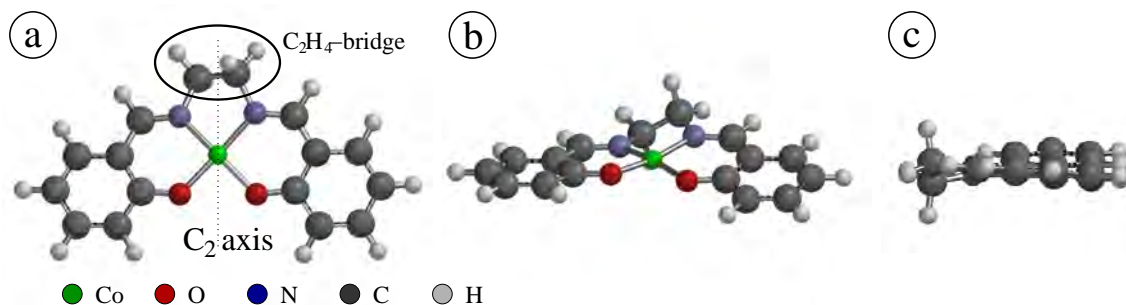
Figure 5.2: (a) Optimized structure of a free Co-Salen molecule modeled by DFT-methods viewed from the top. (b) The side view clarifies a C_2 symmetry due to a deformation of the C_2H_4-bridge. (c) Two hydrogens of the deformed bridge point up and down out of the molecular plane.

In the experiment molecules are first sublimed on a Cu(111) surface followed by a growth comparison depending on the attached substituent (X = H, CH_3, Cl). Afterwards, Co-Salens with hydrogen are prepared for comparison on Cu(100) and an insulating layer of NaCl on Cu(111).

5.1   Co-Salen on Cu(111)

To hinder thermally induced mobility and therefore to enable the study of isolated molecules, molecules are evaporated onto the cooled substrate (see Sec. 3.2 for preparation details). As a result molecules are arbitrarily distributed on the surface. A representative STM image after such a preparation is shown in Fig. 5.3. At the given low bias voltage of $U = -100$ mV the standing wave pattern of the copper surface state is visible already in the topographic image. Due to interaction of the molecules with the substrate molecules act as efficient scattering centers for surface state electrons as manifested in circular scattering patterns around the molecules. As observable in the overview image (Fig. 5.3) with several molecules present in various orientations, all molecules have an identical and characteristic appearance. Therefore the appearance of a single molecule will be discussed first.

Fig. 5.4 shows high resolution topographic images of the same isolated Co-Salen molecule on Cu(111) imaged at different bias voltages. All images are superimposed with the chemical structure at the appropriate scale. The alignment of the structure relative to the position of the molecule is identical for all three images and was achieved through a defect nearby serving as a geometrical marker. Imaged around the Fermi energy (Fig. 5.4b at $U = -100$ mV), the molecule appears as a banana shaped, flat individual with a pronounced central feature and the ends of the banana can be identified as the two C_6-rings of the molecule. Its maximum is not located above the cobalt atom but at a location between the cobalt atom and the top C_2H_4-bridge. The lateral size of the molecule perfectly fits the chemical model.

Imaging the molecule at a larger negative bias, i.e. when tunneling into energetically lower occupied states, these features which are attributed to the C_6-rings almost vanish, whereas the topographic maximum shifts to the position of the cobalt
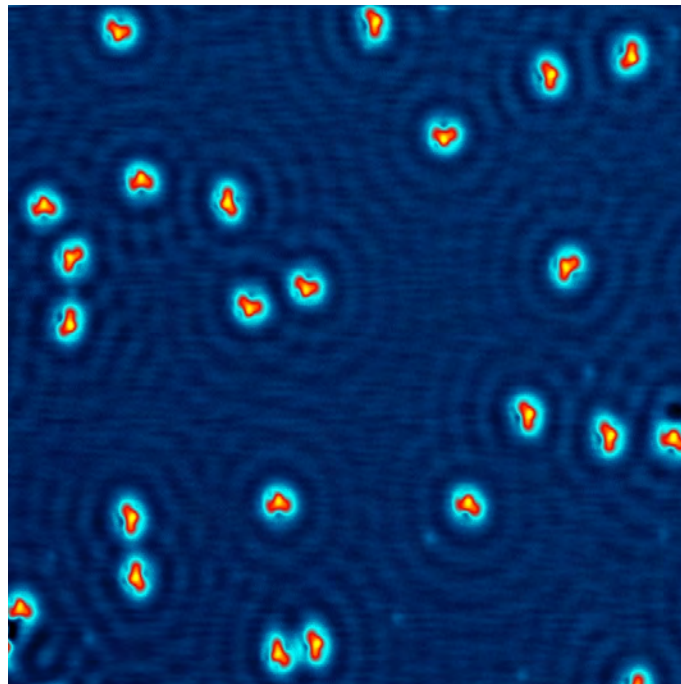
Figure 5.3: STM image of isolated Co-Salen molecules adsorbed on Cu(111) after low temperature deposition. Molecules show a characteristic appearance in several orientations and act as scattering centers for surface state electrons. (40×40 nm^2, $U = -100$ mV).
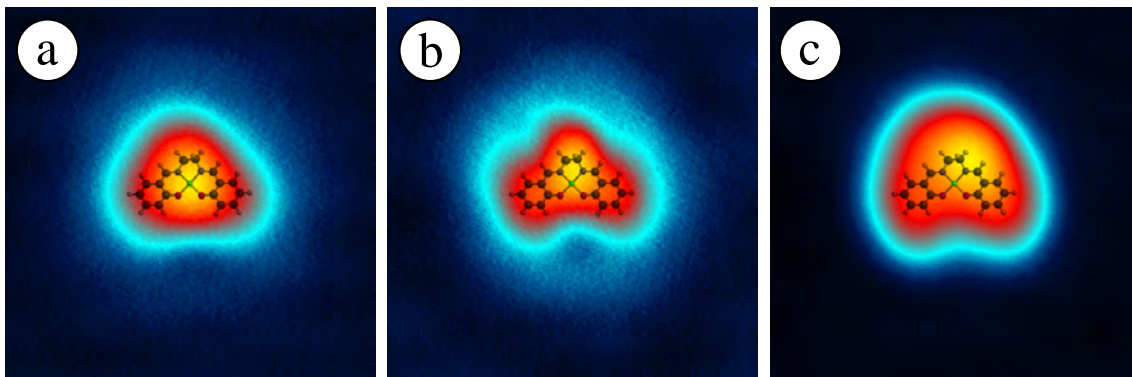
Figure 5.4: Topographic images of the same Co-Salen molecule imaged at (a) $U = -1500$ mV, (b) $U = -100$ mV and (c) $U = +1500$ mV. All images are superimposed with the chemical structure scaled to the image size. The alignment was done relative to a nearby adsorbate serving as a marker. (All images: 3×3 nm^2).

atom (see Fig. 5.4a). Such an accentuation of the metallic ion at certain energies in STM images is characteristic for planar metal-organic complexes such as CoPC, FePC, and other molecules with these metal centers (see also chapter 4). In these systems this is explained by localized d_{z^2} states at the metallic sites, which extend further into the vacuum than the in-plane molecular orbitals. When these states are participating in the tunneling process, the metallic center is imaged as a pronounced maximum in the topographic channel.
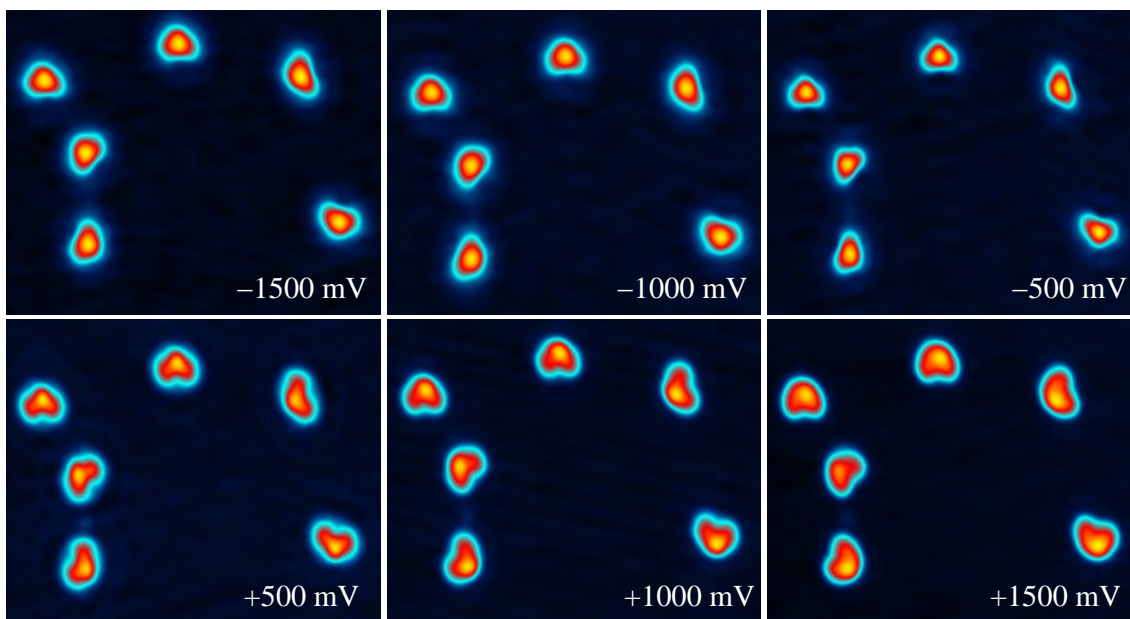
Figure 5.5: Same area of Co-Salen molecules on Cu(111) imaged at different bias voltages as indicated (16×13 nm^2).

Applying a positive bias, the appearance of the molecule changes drastically (Fig. 5.4c). The lateral extension of the molecule is increased and the maximum in apparent height is shifted to the top C_2H_4-bridge of the molecule and slightly to the side. As a consequence molecules appear asymmetric, which can be attributed to the canted C_2H_4-bridge as known from the gas phase.

Zooming in on a group of molecules (from image 5.3) the evolution of molecular appearances in the topographic channel in dependence of the bias voltage is investigated. Six bias voltages at different polarities with representative images are shown in Fig. 5.5. Molecules are present in different orientations. Therefore, all features in the molecular appearance which are rotated accordingly can be attributed solely to molecular properties. Structural features produced by the unknown tip geometry are invariant against the rotation of the studied objects.

At negative bias the variation in molecular appearance is weak. All molecules show the same symmetric shape with a maximum in the center, which increasingly dominates at elevated negative voltages. The apparent height at the maximum (of the molecules shown in Fig. 5.5) increases from $\sim$1.3 Å at $U = -100$ mV to $\sim$1.5 Å at $U = -1500$ mV. These values slightly vary with the actual tip, but the trend as well as the ratio of values remains unaffected and is also independent of the value of the current.

At positive voltages a significant variation is observable. The appearance of molecules is changing already within small voltage steps ($\Delta U = 100$ mV). The shape of molecular appearance becomes more extensive and the maximum is moving to the top and to the side with increasing voltage. Depending on the orientation of the molecule, the maximum is either moving to the left or the right side. This effect will be discussed in more detail in the next section.

The variation of the apparent height values is much stronger at positive bias

compared to negative voltages. The values (measured for the same molecules in Fig. 5.5) vary from $\sim$1.3 Å at $U = -100$ mV to $\sim$2.5 Å at $U = +1500$ mV. This is explained by the interplay of electronic density and real topographic height and is clarified by STS measurements in Sec. 5.1.2.

5.1.1 Orientations on Cu(111)

Co-Salen adsorbs in 12 different orientations on Cu(111), which has a sixfold symmetry (see Sec. 3.1.2). All observed configurations are depicted in Fig. 5.6 as imaged with the STM operated at low ($U = -100$ mV, Fig. 5.6a) and high ($U = +1400$ mV, Fig. 5.6b) bias voltages.

The observable asymmetry at elevated positive energies (Fig. 5.6b) unambiguously reveals two mirror symmetric ("R" vs "L") sets of six molecules each rotated in steps of 60°. The six rotations (α to ζ) are attributed to the sixfold symmetry of the substrate and the two mirror symmetric configurations to the chirality of the molecule. With the exact crystallographic axes determined from atomically resolved images of the bare copper substrate, two mirror symmetric enantiomers can be attributed to each crystallographic direction. Molecules denoted with "R" are rotated clockwise by $+11° \pm 3°$ relative to the substrate axes and with "L" anticlockwise by $-8° \pm 3°$, respectively. This is schematically illustrated in Fig. 5.6c.

DFT calculations of Co-Salen adsorbed on the Cu(111) surface were performed by M. Prosenc *et al.*, which revealed an optimized structure as depicted in Fig. 5.7a. The C_2-axis as defined for the free molecule is tilted by -10° relative to one of the closed-packed directions of the substrate. Such a molecule corresponds excellently to a left-handed molecule of configuration ζ_L as experimentally observed.

A detailed view is given in the 3D representation of the results of the calculation (Fig. 5.7b). A distance of 325 pm between the Co-center and the copper surface is found. The Co-center is shifted about 11 pm below the O_2N_2-ligand plane spanned by the two oxygen and two nitrogen ligand atoms indicating hybridization of the
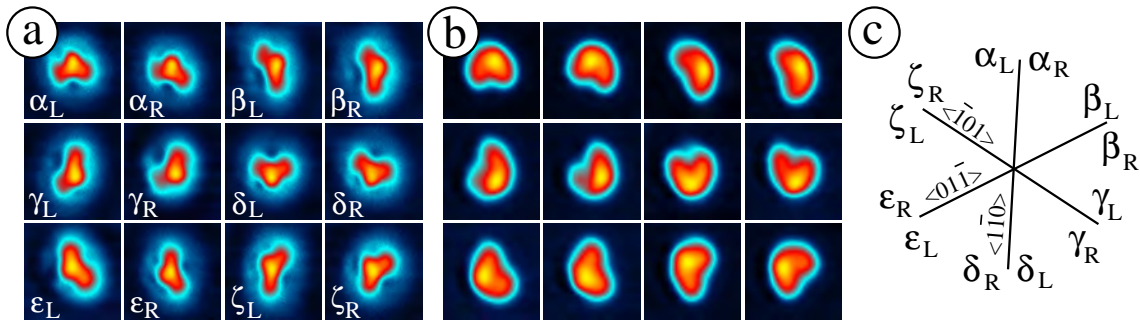
Figure 5.6: Topographic images of Co-Salen molecules adsorbed in 12 different configurations on a Cu(111) surface recorded at (a) $U = -100$ mV and (b) $U = +1400$ mV (all images 2 × 2 nm^2). The six main configurations due to the substrate geometry are labeled α to ζ, the two variations due to chirality with "L" and "R". (c) Sketch of all 12 configurations with the substrate axes indicated by black lines.
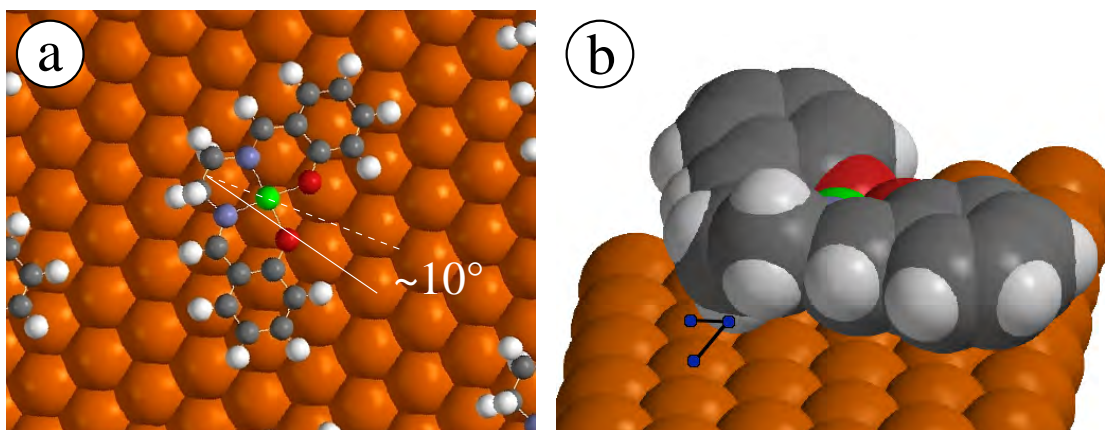
Figure 5.7: Optimized Co-Salen complex on a Cu(111) surface. (a) The top view reveals an angle of $\sim 10°$ between the C_2 axis of the molecule and one crystallographic axis of the substrate. The example shown corresponds to configuration ζ_L. (b) Van-der-Waals representation of deposited Co-Salen; close contacts of one of the C_2H_4-hydrogen atoms with surface Cu atoms (edge site, Cu-H = 254 pm, Cu-H = 260 pm) are depicted by blue dots.

Co-orbitals with substrate states. In addition, short distances (d(H-Cu) = 254 pm and 260 pm) between one of the C_2H_4-hydrogen atoms and Cu-atoms (indicated by blue dots in Fig. 5.7b) and distances of d(C_6-Cu) = 325 pm and 375 pm between the centroids of the C_6-rings of the Salen ligand and the nearest Cu-atom reveal the point of molecule-surface interaction. Compared to the optimized structure in gas phase (Fig. 5.2) Co-O and Co-N distances are extended by 2 pm and 3 pm, respectively, upon deposition of Co-Salen on the surface. An epimerization of the C_2H_4-bridge leads to different H-Cu$_2$ contacts, which result in a rotation of the molecule by about 20°, i.e. $+10°$ relative to one of the closed-packed directions of the substrate. This fits perfectly to the two mirror symmetric enantiomers observed in the experiment. The deformation of the bridge and the slight canting from top to bottom of the molecule on the surface lead to the asymmetric maximum feature in apparent height.

5.1.2   Spectroscopy on Co-Salen

A way to investigate electronic properties of Co-Salen molecules on Cu(111) is point spectroscopy. A representative example of a spectrum taken over a Co-Salen molecule is shown in Fig. 5.8 (red curve) along with a reference spectrum taken on the bare copper surface (blue curve). The surface state of the Cu(111) surface is visible at $U = -450$ mV.

In the Co-Salen spectrum, the negative side is completely featureless and corresponds to the reference copper spectrum up to $U = -2000$ mV. On the positive side a pronounced shoulder in the density of states is observed. Due to molecular instabilities at elevated energies, the peak of the maximum cannot be resolved and its exact energy position is unknown. (See the next section for more details about effects in the elevated positive voltage regime.) Such a molecular spectrum
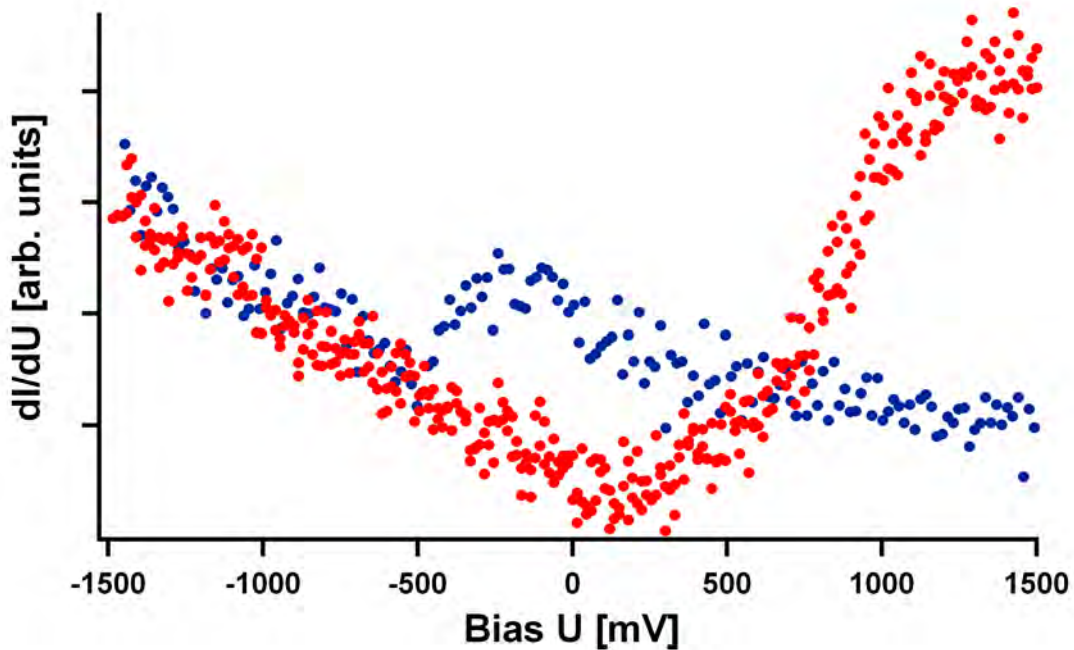
Figure 5.8: Point spectroscopy curves taken over the center of a Co-Salen molecule on Cu(111) (red curve) and on the copper surface for reference (blue curve).

is characteristic for strong hybridization. Occupied states of the molecule (negative energies) are suppressed by the contact to the metallic substrate.

For a better understanding of the spatial distribution of electronic states within the molecule, maps of the differential conductivity (dI/dU-maps) are acquired. Since Co-Salen molecules do not show any characteristic feature at $U < 0$ eV, dI/dU-maps acquired at negative bias are neglected. This coincides with the observation of non-significant contributions of molecular states when performing point spectroscopy at negative bias on molecular sites.

For a detailed discussion, an isolated molecule with an adsorbate as a reference is chosen. Topographic images and dI/dU-maps are acquired in parallel with the bias voltage ramped from $U = +100$ mV in 50 mV-steps up to $U = +1550$ mV. The dI/dU-maps are recorded with Lock-In technique using a modulation voltage of $V_{\mathrm{mod}} = 20$ mV added to the bias at a frequency of $f = 1.777$ kHz. The complete collection of images is shown in Fig. 5.9. The corresponding dI/dU-maps are shown below each individual topographic image. Due to a strong molecule-substrate interaction the change in appearance with bias in the topographic images is subtle and varies gradually over the complete range between $U = +100$ mV and $U = +1550$ mV. The molecule grows in size with increasing voltage with the maximum in the apparent height shifted to one side of the top C_2H_4-bridge.

The changes in the dI/dU-maps are much more pronounced than in the topographic channel. At the lower voltages (100-400 mV, first row), the influence of the copper surface state is strong. Therefore, the scattering of surface state electrons at the molecule serving as a scattering center dominates in the dI/dU-maps. The conductivity at the site of the molecule coincides with the topographic channel, but
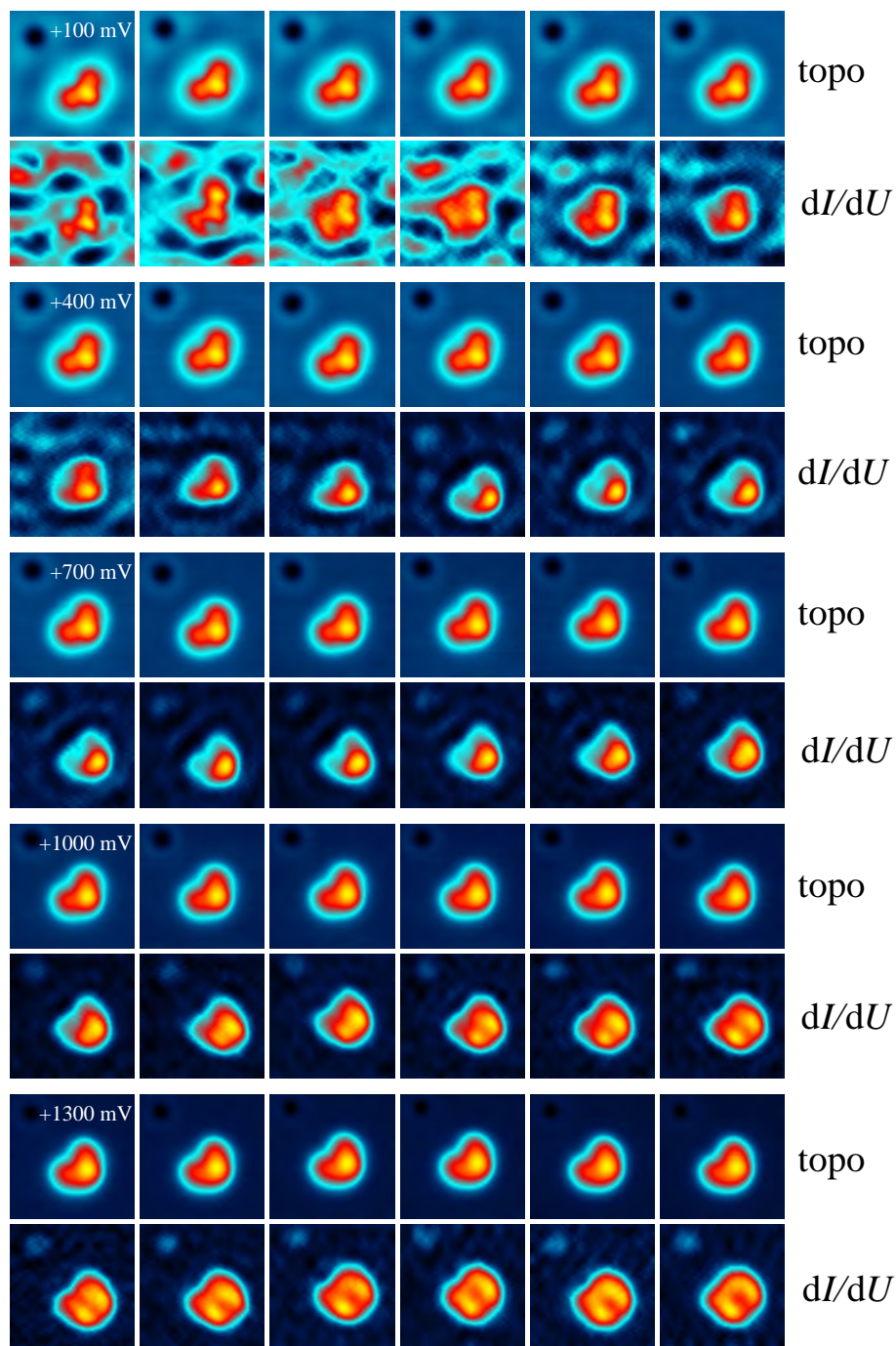
Figure 5.9: Simultaneously recorded STM topographs and dI/dU-maps (corresponding image below topograph) of a single isolated Co-Salen molecule. The bias voltage is increased in 50 mV-steps from left to right starting from $U = +100$ mV up to $U = +1550$ mV. All images are 3×3 nm^2.

with a slight asymmetry between the two sides of the molecule: the left C_6-ring of the molecule shows a higher electron density than the right one. With increasing energy, the electron density on the sites of the C_6-rings decreases. Instead, a single maximum is forming on the top of the molecule with an asymmetry towards the left side (second row, 400-700 mV). The spatial variation of the next voltage interval is not very peculiar (third row, 700-1000 mV). The central feature is gaining in intensity and is increasing in size. This is consistent with STS data, where the onset of the signal on the molecule occurs at $U = +700$ mV. The most striking change in the spatial distribution of the electron density takes place starting with $U = +1000$ mV (fourth and fifth row). The central feature is splitting into two pronounced maxima with a node in the middle. With increasing energy these maxima are moving to the sides of the molecule and increase in size along the vertical direction of the molecule. Still, the left maximum has a slightly higher intensity than the right one reflecting again the asymmetry of the molecule. At the highest voltage setting, the dI/dU-map displays a nice set of two straight maxima with a distinct node in the middle.

To exactly correlate the molecular structure to specific spectroscopic features in dI/dU-maps, i.e. to avoid lateral displacement by the actual tip shape or by drift and creep, a nearby adsorbate serves as a marker. STM topographs along with their corresponding dI/dU-maps at voltages with significant changes are selected from the collection of Fig. 5.9. They are superimposed with the molecular structure of Co-Salen aligned to the adsorbate and presented in Fig. 5.10.

As previously discussed the maximum in the topographic channel is shifting to the top left of the asymmetric C_2H_4-bridge. This asymmetry is reproduced in the dI/dU-maps, but the variation is much stronger with increasing bias voltage. At $U = +400$ mV the appearance in the dI/dU-signal is similar to the topographic channel, with a reduced intensity on the right side of the molecule. Changing to $U = +700$ mV the intensity on the C_6-rings nearly vanishes completely and a strong maximum is observed on the top left of the molecule. This maximum is increasing
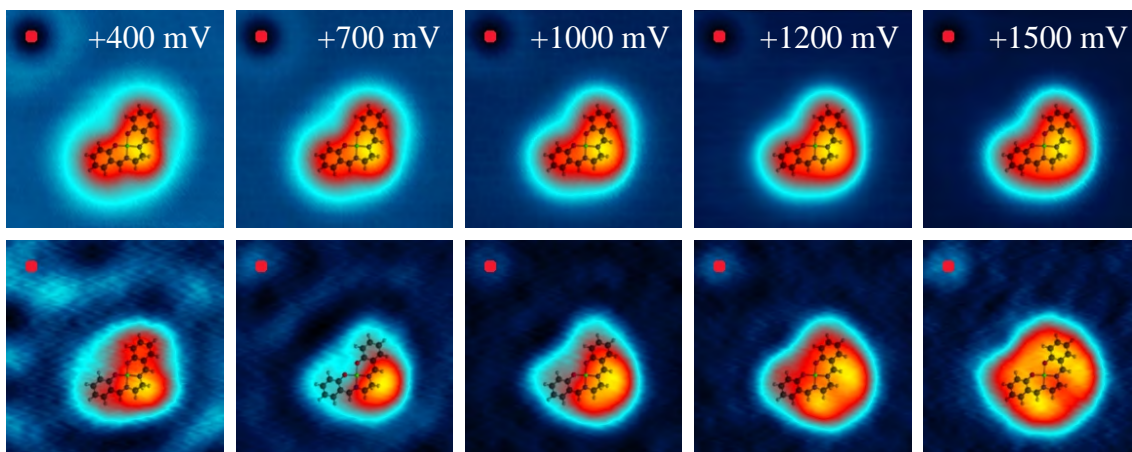
Figure 5.10: Selected images from Fig. 5.9 superimposed with the molecular structure aligned in relation to the adsorbate marker as imaged at voltages, where significant changes can be observed (all images 3×3 nm^2).

in lateral size when increasing the energy to $U = +1000$ mV. Most striking is the extension of the electron density beyond the structure of the molecule. The molecular state extends well beyond the C_2H_4-bridge with a maximum located at the left, while it shows negligible contribution on the C_6-rings. This asymmetric shape fits to the slight tilt of the molecule compared to the copper plane derived from theoretical calculation discussed earlier in this chapter. The splitting of the maximum starts at $U = +1200$ mV and evolves into a node at the middle of the molecule with the two maxima moving to the sides with increasing energy. In the dI/dU-map taken at $U = +1500$ mV the two maxima start at the location of the C_6-rings and extend a long way over the top of the structure of the molecule. The node goes from the top down to the location of the cobalt atom.

These striking appearances in the dI/dU-maps concerning asymmetry and splitting of the maximum are investigated more thoroughly using DFT calculations performed by Prof. S. Sanvito *et al.*. The results are preliminary and the calculation is still in progress, but selected topographic images and dI/dU-maps for low ($U = +600$ mV) and elevated ($U = +1500$ mV) positive energy taken from STM experiments in comparison to the simulated images are presented in Fig. 5.11. The comparison is done for a molecule of the right-rotated variation ("R").

On the left the comparison between the topographic channel of STM and DFT is shown. The STM image at $U = +1500$ mV exhibits the typical appearance for elevated positive energy. The lateral size of the molecule is increased compared to the appearance at $U = +600$ mV and the maximum feature shifts to the top left. This effect is also observed in the simulated images.

The agreement in the dI/dU-maps is also persuasive. In the STM image at $U = +600$ mV a pronounced maximum feature is observed on the left side of the C_2H_4-
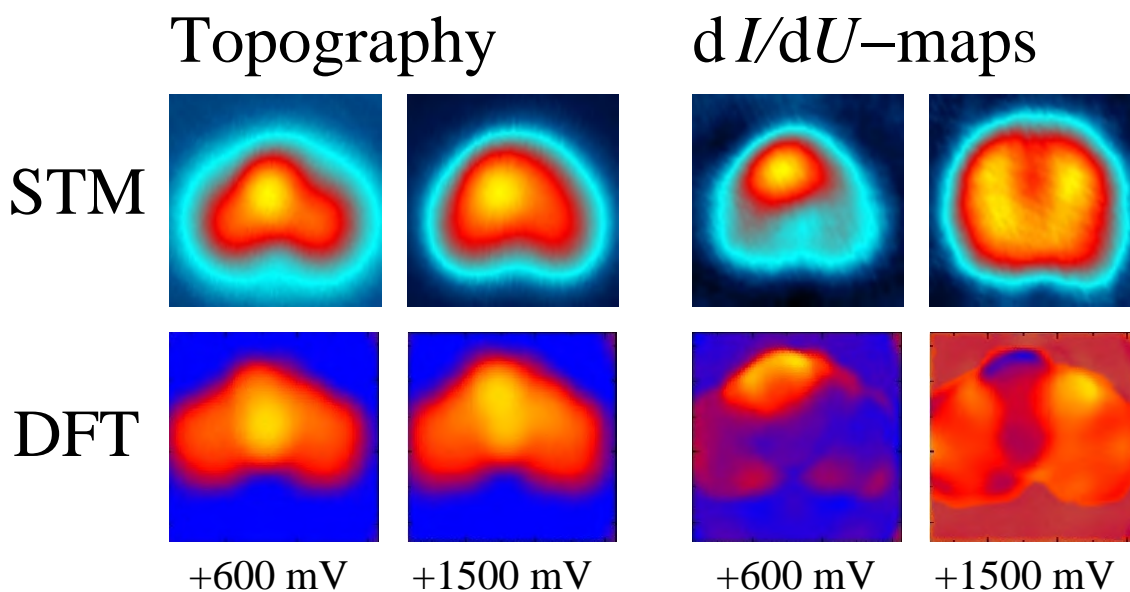
Figure 5.11: Comparison between experiment and theory. The appearance of single Co-Salen molecules on Cu(111) in the topographic and the differential conductance channel was modelled by DFT calculations. (All images: 2×2 nm^2).

bridge, which dominates over the rest of the molecule. This is perfectly reproduced in the calculated dI/dU-map. For the elevated energy the significant double maximum with a node in differential conductance also at the location of the cobalt atom is observed in the DFT calculation. The overall agreement is representative and further results are highly anticipated.

5.1.3 Hydrogen stripping

In this section effects which result from contacting Co-Salen at large positive bias are discussed. It is possible to reproducibly remove two hydrogen atoms from the C_2H_4-bridge by injecting energy into the molecule with the STM tip. The two new dehydrogenated states of the Co-Salen were modelled using DFT calculations performed by Prof. S. Sanvito *et al.*. They are clearly distinguished by their appearance in topographic images from the initially intact molecule. The single dehydrogenated state, called 1H-less in the following, still exhibits a deformation in the C_2H_3-bridge. This is different for the double dehydrogenated state (2H-less), which is mirror symmetric with one hydrogen left per carbon atom in the C_2H_2-bridge. All three states (intact, 1H-less, 2H-less) exhibit different apparent heights. The manipulation can be done either with point spectroscopy or in the normal constant current scanning mode.

As an example Fig. 5.12 shows the same molecule before and after point spectroscopy to probe molecular states up to 2 eV. A distinct change in appearance
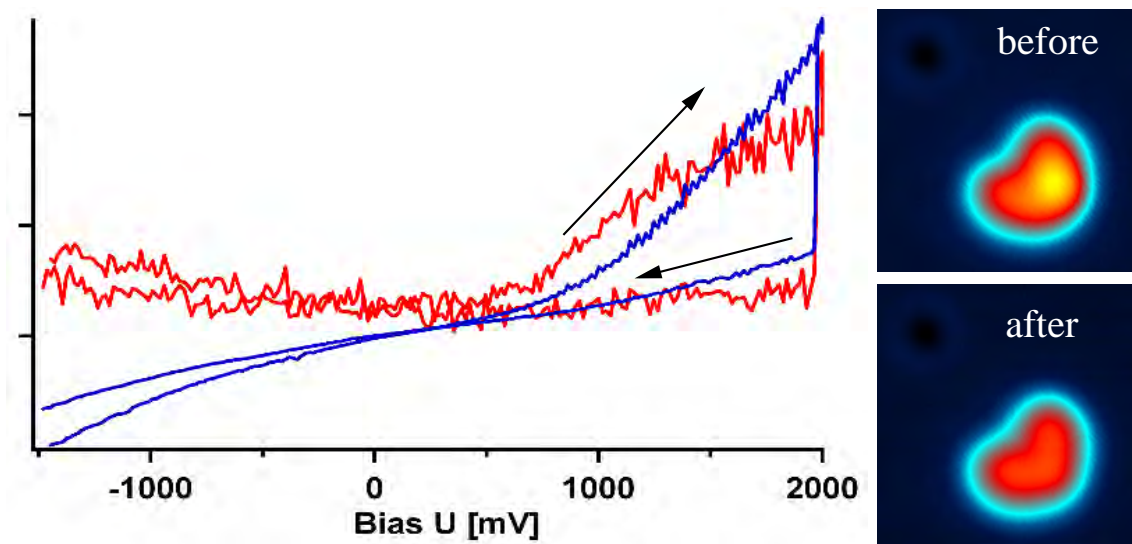
Figure 5.12: Single point spectroscopy curve taken over the center of a Co-Salen molecule. The bias voltage was ramped from $U = -1500$ mV to $U = +2000$ mV and back indicated by the black arrows. The molecule changed during the spectrum acquisition, which is seen as a sudden drop in the dI/dU (red) as well as in the I/U-signal (blue). This change is also visible in the appearance of the molecule when comparing STM topographs taken before and after the spectrum. The adsorbate serves again as a marker.

can be observed. In the presented experiment the tip is positioned over the center of the Co-Salen molecule. For spectroscopy the bias voltage is ramped from $U = -1500$ mV to $U = +2000$ mV and then back to the initial bias setting with an open feedback loop, i.e. at constant height. During this procedure the tunneling current I and the differential conductivity dI/dU are recorded. The curves for both signals are plotted in Fig. 5.12. At a large positive energy the signals drop abruptly and remain at this level for the backwards ramp. Repeating the acquisition, the sudden drop does not reappear, but the molecule is changed. Comparing STM images of the molecule as taken before and after the spectroscopy measurement, the change in appearance is obvious. The molecule after the spectroscopy acquisition is easily identified as the double dehydrogenated state of the molecule with a symmetric C_2H_2-bridge. The apparent height is reduced and the shape became symmetric. Such a change in appearance is regularly observed when applying a bias voltage above $U = +1700$ mV during spectroscopy acquisition, but the intermediate state of the molecule, the single dehydrogenated state, could not be observed. Therefore, another approach is presented to gain access to the intermediate state 1H-less.

The manipulation also occurs when scanning over Co-Salen molecules at positive bias voltages above $U = +1700$ mV as demonstrated in Fig. 5.13.
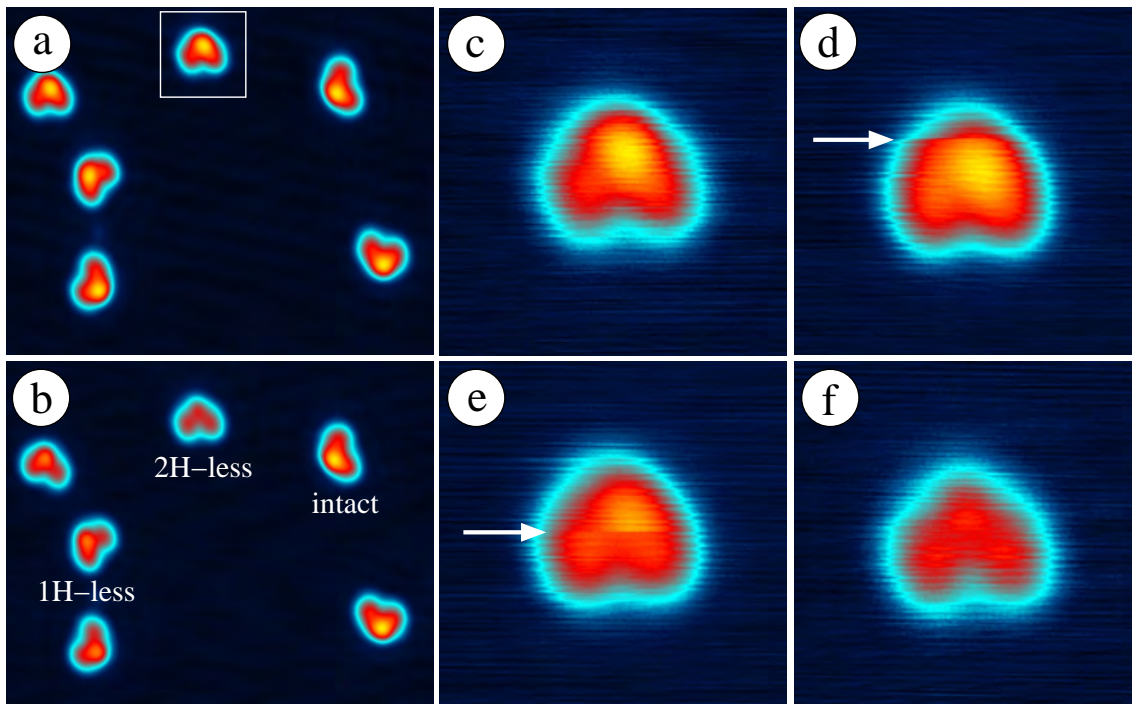
Figure 5.13: Manipulation of Co-Salen molecules by scanning with high positive bias voltage of $U = +1700$ mV. Six individual molecules are shown (a) before and (b) after scanning with increased voltage (both images 16 nm × 13 nm, $U = +1000$ mV). (c) Blow-up of the single molecule marked by the white square in (a). The molecule is then scanned with $U = +1700$ mV (d) up and (e) down again. The observed change in the molecule is indicated by a white arrow. (f) The same molecule after the manipulation with the height scaled to image (c) for comparison.

There, six individual molecules in different orientations are imaged at $U = +1000$ mV (Fig. 5.13a), i.e. at a voltage which does not affect molecules. One molecule is selected for a zoomed scan at an elevated voltage, which is indicated in Fig. 5.13a by a white square. Before the manipulation scan, the molecule is imaged for comparison at a bias of $U = +1000$ mV (Fig. 5.13c). The molecule exhibits the already known asymmetric structure with a pronounced maximum. The molecule is then scanned at a voltage of $U = +1700$ mV with the slow scan direction from bottom to top (Fig. 5.13d). During the scan a change in the appearance of the molecule in one fast scanline as indicated by the white arrow is observed. Another scan is performed (with the slow scan direction going from top to bottom) inducing another change in the molecular appearance. A reduction in apparent height is observed. Further scanning of the molecule does not cause additional changes. For comparison with the initial state, the molecule is again scanned at $U = +1000$ mV (see Fig. 5.13f scaled in z-values to the height of Fig. 5.13c). It appears strongly reduced in height and exhibits now a mirror symmetry.

Then, a high voltage treatment ($U = +1700$ mV) is applied during one scan to all three molecules on the left side. Directly afterwards the complete area is revisited at a low voltage ($U = +1000$ mV) where tip induced changes were not observed. This is presented in Fig. 5.13b. Molecules in three different states are clearly identified as manifested in their apparent height and symmetry.

This two-step process of induced modification now reveals also the intermediate state of dehydrogenation of the top C_2H_4-bridge on Co-Salen molecules. One hydrogen is removed per manipulation by a high voltage scan. After the first dehydrogenation, the molecule goes into closer contact with the surface and appears reduced in height. Due to the three remaining hydrogens, the top bridge still exhibits a deformation, which is observed as an asymmetry in the topographic appearance of the molecules (see molecules on the left in Fig. 5.13b labeled as 1H-less). The second dehydrogenation causes a further reduction in apparent height and the molecule appears mirror symmetric (compare molecule labeled as 2H-less in Fig. 5.13b). This symmetric shape is explained with the top bridge now being in the molecular plane with two remaining hydrogens. These manipulations by a scan at $U = +1700$ mV are highly reproducible, which can already be seen from the three single dehydrogenated molecules in Fig. 5.13b (1H-less).

This interpretation is supported by results from DFT calculations by M. Prosenc and S. Sanvito. From the alignment of the molecule on the copper surface shown in Fig. 5.7b, the most probable point of change is the hydrogen in the top bridge in close contact to the copper surface. This fits to the observation of the modification scanline during a high voltage scan being always in the top part of the molecule (compare Figs. 5.13d+e). Another result from the calculations is the loss of one hydrogen atom in the top bridge, when the molecule was relaxed on the surface with the top bridge energetically not fully relaxed. The amount of energy for such a dehydrogenation was calculated as ~1.8 eV, which is in good agreement with the voltage needed for a manipulation in the range of $U = +1700 - 2000$ mV.

For a more precise and reproducible characterization of the manipulation process, point spectroscopy and imaging at a high bias voltage for manipulation, and imaging at low bias voltage for characterization are used in a combined approach.
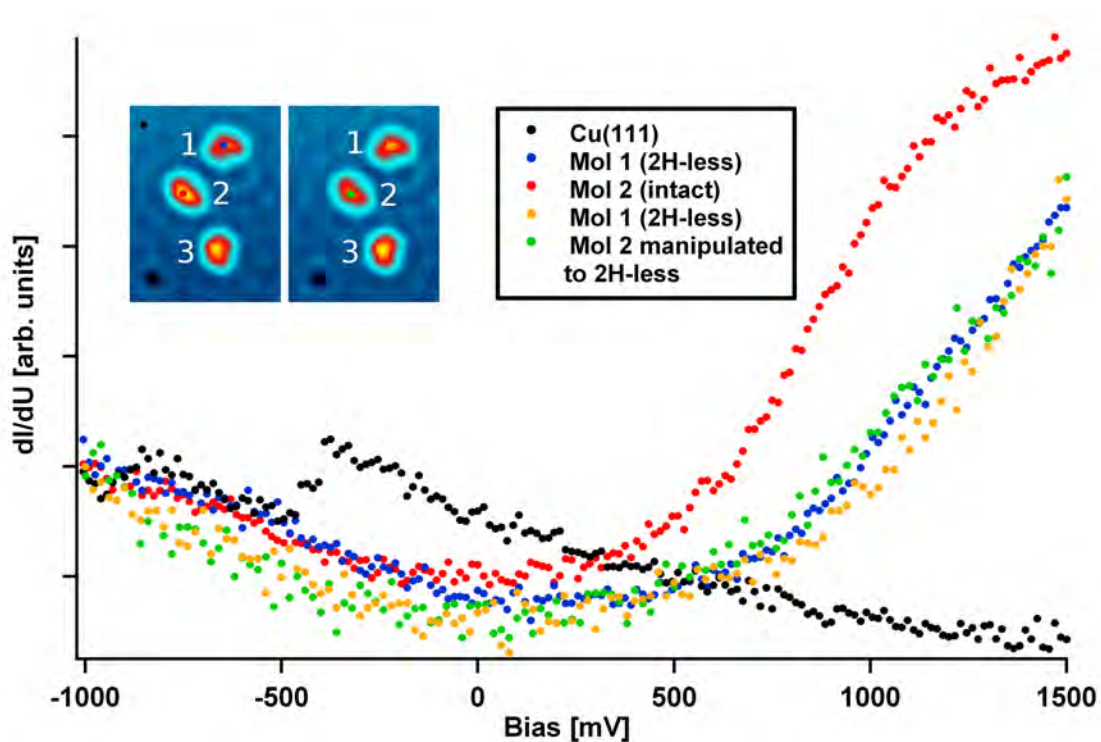
Figure 5.14: Comparison of double dehydrogenated and intact Co-Salen molecules in point spectroscopy. The spectra were taken at the locations indicated by the colored points in the inset. Inset: STM images of Co-Salen molecules on Cu(111) taken before and after acquisition of the point spectra indicated by the colored points. The double dehydrogenated molecule 1 in the first image was manipulated by high voltage scanning, molecule 2 in the second image by point spectroscopy. Molecule 3 remains intact for comparison ($U = +100$ mV, 8×10 nm^2).

An area on the surface was chosen with three molecules visible. They are numbered as molecules 1-3 in the following. Molecule 1 was deliberately manipulated with a high voltage scan into the symmetric state 2H-less. This is shown in the left image of the inset in Fig. 5.14. Non-manipulative point spectra are acquired in the range of $U = \pm 1500$ mV on molecules 1+2. Then, a manipulative spectroscopy curve reaching a bias voltage of $U = +2000$ mV is acquired on molecule 2. A topographic scan of the same area as before is recorded and shown in the right image of the inset in Fig. 5.14. Afterwards, point spectra of the non-manipulative kind are again acquired on the molecules 1+2. Molecule 3 serves as a reference for comparison of apparent height in topography.

Point spectra are recorded on the high voltage scan manipulated molecule 1 (blue) and on the upper intact molecule 2 (red) as indicated. Both curves show a characteristic signature of the LUMO state of the Co-Salen molecule, but the signal strength in the STS data is reduced for the manipulated molecule. In addition, a reference spectrum is taken on the clean copper surface (black). It shows the typical signature of the copper surface state.

Then, molecule 2 is manipulated by a high voltage spectroscopy treatment, reach-

ing a bias of $U = +2000$ mV (not shown). Comparing the appearances of both molecules 1 and 2 in another scan (right inset in Fig. 5.14), their apparent height and symmetric shape reveals both molecules in the double dehydrogenated state. Spectroscopy curves are acquired again on both molecules (yellow and green curves in Fig. 5.14). The curves became identical and indicate, that both manipulation methods lead to a double dehydrogenation of the molecules.

So far, a characteristic fingerprint in the electronic signature of the intact and the dehydrogenated Co-Salen is observed. For a more detailed analysis molecules of all three states (intact, 1H-less, and 2H-less) are investigated in terms of spatial distribution of the electronic states. Figure 5.15 shows a collection of dI/dU-maps with increasing bias voltage recorded on the identical surface area. In the first STM image at $U = +500$ mV, molecules in the three different states are nicely resolved. The intact Co-Salen molecule exhibits the largest apparent height followed by the single dehydrogenated molecule (1H-less). The double dehydrogenated Co-Salen (2H-less) appears flat without a pronounced maximum.

The difference between the three states is more pronounced in their appearance in dI/dU-maps. The intact Co-Salen molecule exhibits the evolution of the electron
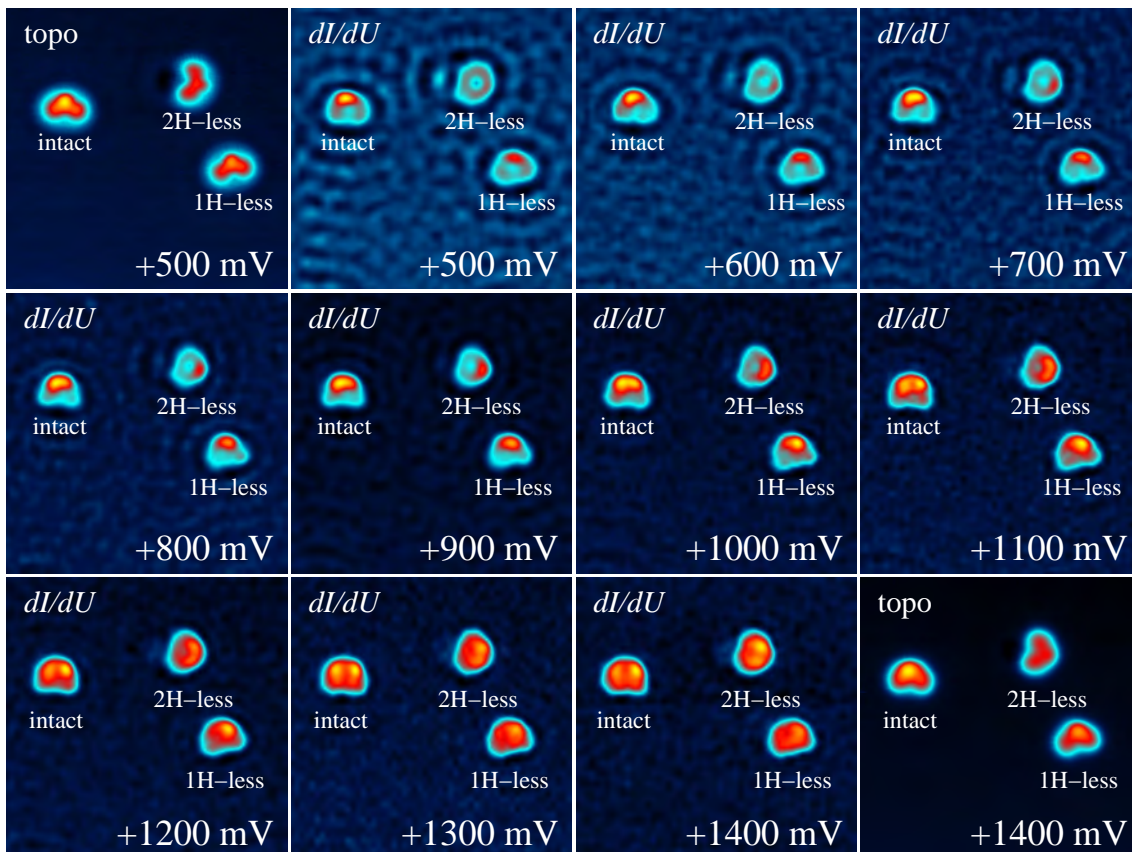
Figure 5.15: The evolution of the electronic states with increasing bias voltage for all three states of Co-Salen on Cu(111) presented in dI/dU-maps. The first STM image shows the topographic channel of the area with Co-Salen molecules in the intact, 1H-less, and 2H-less states (13×13 nm^2).

density as already discussed in the previous section. The dI/dU-maps reflect the asymmetry of the molecule and the maximum in electron density is located on the left side of the C_2H_4-bridge. With increasing energy, the maximum extends laterally further and splits into two separate maxima with a node at the location of the C_2-axis. The situation is different for the 1H-less molecule. The asymmetry in the dI/dU-maps remains strongly pronounced with the maximum on the right for this particular molecule configuration. Different to an intact Co-Salen molecule, the maximum does not split and only one side shows a pronounced maximum in the signal. For the case of the 2H-less molecule, the appearance is again different. The dI/dU-maps show a completely symmetric appearance of the molecule, similar to the appearance in the topographic channel. The signal strength is significantly reduced in comparison to the other molecule states and the signal is predominantly located on the top bridge. Still, a splitting of the maximum is observed, but at a much higher energy ($U = +1300$ mV). For comparison and to make sure that the molecules did not change during the image acquisition, the last STM image shows the topographic channel at $U = +1400$ mV.

The behavior in the dI/dU-maps of the two dehydrogenated states fits perfectly to the picture of hydrogen atoms missing in the top bridge of the molecule. For the single dehydrogenated state (1H-less), the three remaining hydrogens still keep the top C_2H_3-bridge tilted. The asymmetry is strongly pronounced in the dI/dU-maps over the whole voltage range. The most important feature is observed at voltages of $U = +1100$ mV and above. Comparing the appearance of the 1H-less state to the intact molecule, they look quite similar just with one maximum missing in the case of the 1H-less state. This reflects a missing hydrogen in the shape of this particular molecular orbital.

In the case of the 2H-less state, the appearance in the dI/dU-maps is completely symmetric. This indicates a double dehydrogenation of the molecule with the loss of chirality. Furthermore, the signal is much reduced compared to the asymmetric states. The symmetric appearance of the molecule as well as the reduced apparent height strengthen the interpretation, that the 2H-less Co-Salen is lying flat on the surface in difference to the intact molecule, which is lifted from the surface by the tilted top-bridge.

5.2 Influence of 5,5'-substituents on Configuration and Self-assembly

So far isolated molecules of Co-Salen with hydrogen in the 5,5'-positions were discussed. Although a complete decoration of monoatomic copper steps indicates high mobility during deposition (on a sample) at room temperature no self-assembly is observed. This is shown in Fig. 5.16. Starting with a low coverage as seen in Fig. 5.16a, molecules stick to step edges and defects but terraces are undecorated. This demonstrates, that molecules have a high mobility at room temperature. When the coverage is further increased, molecules do not show any tendency to self-assemble (see Fig. 5.16b).

Instead, molecules stay fully isolated, which suggests a repulsive molecule-molecule
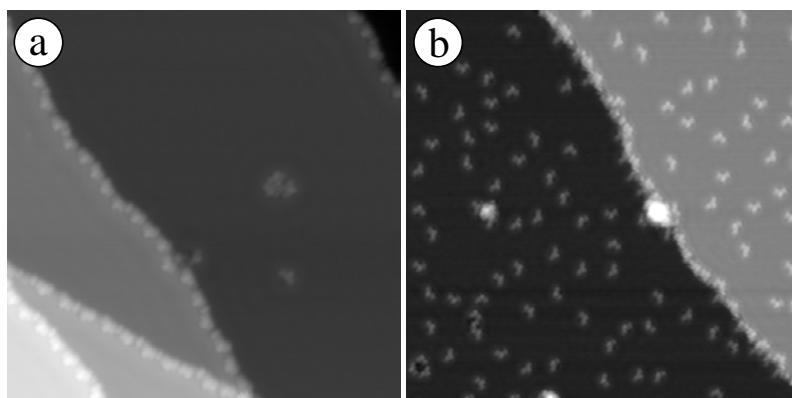
Figure 5.16: Typical images after room temperature preparation at a low (a) and medium (b) coverage of Co-Salen on a Cu(111) surface. (a) Only step edges and defects are decorated (30×30 nm^2, $U = -130$ mV). (b) Molecules do not show any tendency of self-assembly, but stay isolated on flat terraces indicating repulsive forces (45×45 nm^2, $U = +300$ mV).

interaction. An energetically favorable dimerization by a stacking perpendicularly to the molecular plane as in bulk material [111–113] is prevented by the strong molecule-substrate coupling and was not observed. To overcome the present in-plane repulsive steric forces and to artificially equip Salens with the ability to form regular molecular networks, a substituent bearing a high polarity (Cl, complex **3**) is introduced to outbalance the molecular charge distribution and to induce a local attractive dipole moment. Chloride serves as such a negative electric pole "–", which positively charges the molecular center ("+"). As additional reference another substituent (methylgroup CH$_3$, complex **2**) was chosen.

The chemical structures of all three complexes of Co(5,5'-X$_2$-Salen), X=H (**1**), CH$_3$ (**2**), and Cl (**3**) used in this study are presented in Fig. 5.17 with corresponding STM images of isolated molecules adsorbed on a Cu(111) surface and imaged at $U = -100$ mV. For visualization a scaled model of the chemical structure is superimposed. The molecular species are called complexes **1-3** in the following. For complex **1**, the already discussed Co-Salen with hydrogen as substituent, the appearance of the molecule in the STM image fits perfectly to the structure. Due to the different substituents the apparent size of complexes **2** and **3** varies in the topographic images. The influence of the substituent on the local polarity is visualized by charge density plots of all three complexes (see right side of Fig. 5.17). The color bar indicates the polarity distributed over the structures of the complexes. The influence of the methyl group as substituent on the potential landscape in comparison to complex **1** is negligible. The introduction of chloride as substituent on the other hand has a strong influence on the local polarity of the complex. The polarity at the sites of the chlorides turns from positive to negative, additionally neutralizing the former negative polarity on the C$_6$-rings leading to small dipolar gradients added to the sites between chloride and C$_6$-rings.

When studied as isolated molecules after low temperature preparation, all three complexes share the same properties in terms of appearance, chirality and adsorp-
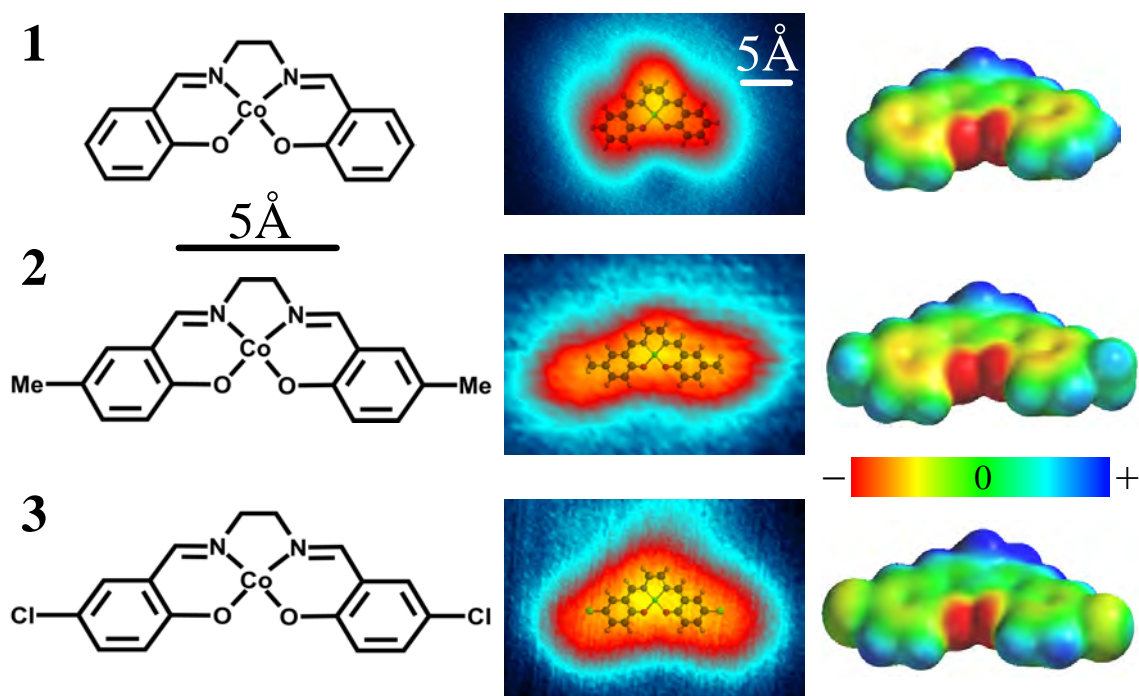
Figure 5.17: Co(5,5'-X$_2$-Salen), X=H (**1**), CH$_3$ (**2**), and Cl (**3**) complexes used in this study shown with their chemical structures (left), equally scaled representative STM images superimposed with a scaled model (middle, STM images 3×2 nm^2, $U = -100$ mV), and contour plots of the charge distribution (right).

tion site. This is demonstrated for the reference molecule complex **2** in Fig. 5.18. However, it must be noted that even at 25 K single molecules of complex **3**, contrary to complex **1** and **2**, are easily displaced by the STM tip during experiments, which indicates the presence of additional forces.

Molecules of complex **2** and **3** also adsorb in 12 different configurations on the Cu(111) surface. Configurations α_L to γ_R of complex **2** are shown in Fig. 5.18a. They exhibit the same angle of 20° between the C_2-axes of "R" and "L" types
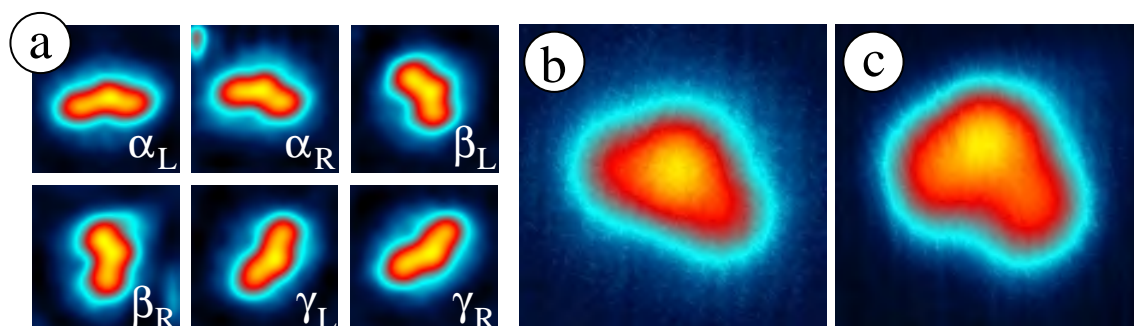
Figure 5.18: Adsorption behavior and appearance in STM topographs shown for reference complex **2** on Cu(111). (a) Configuration α_L to γ_R imaged at $U = -100$ mV. Configuration α_R imaged at (b) $U = -1400$ mV and at (c) $U = +1400$ mV revealing the same features as complex **1** (3×3 nm^2).
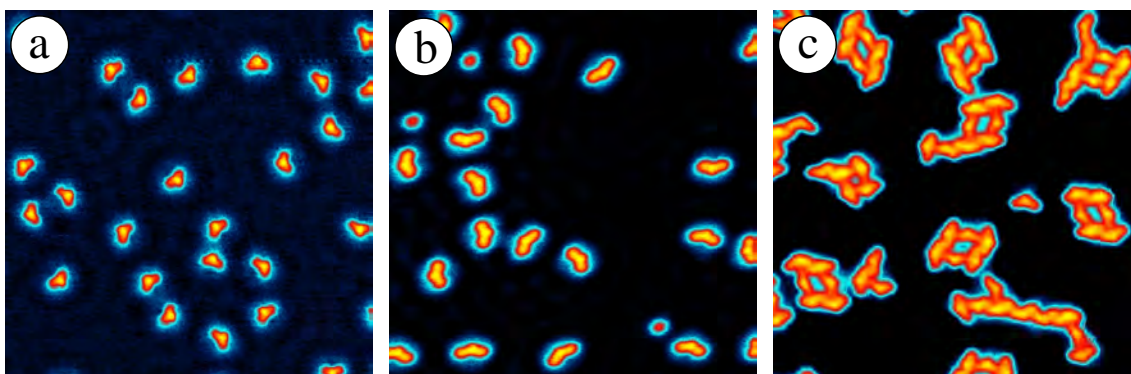
Figure 5.19: Co(5,5'-X$_2$-Salen), X = (a) H, (b) Me, (c) Cl after room temperature preparation on Cu(111). Chloride terminated complexes show self-assembling on the surface (all images 25×25 nm^2, $U = -100$ mV).

reflecting chirality. This is consistent with the observation of complex **1**. The appearance of complex **2** and **3** in the STM topographic channel at elevated negative ($U = -1400$ mV) and positive ($U = +1400$ mV) bias voltages is also similar to the appearance of complex **1**. This is demonstrated by imaging complex **2** at these two bias values. At elevated negative voltages the apparent height on the sides of the molecule is decreased and the strong maximum feature shifts to the location of the cobalt atom (Fig. 5.18b). At elevated positive bias, the maximum in apparent height shifts asymmetrically to one side of the C$_2$H$_4$-bridge (Fig. 5.18c).

Concerning self-assembly, these three structures interact differently. Figure 5.19 shows representative images of complexes **1**–**3** on Cu(111) after room temperature preparation. For complexes **1** and **2**, no indication for attractive interaction among the molecules is observed (compare Figs. 5.19a+b). Molecules are mobile during preparation and stick to step edges and defects, but stay isolated on terraces. With chloride as substituent in complex **3**, molecules form peculiar six membered clusters (see Fig. 5.19c). Competing structures of lower frequencies are chains and four membered islands. All structures vary in orientation and chirality reflecting the manifold orientations of the single molecules.

The six membered clusters are clearly dominating and are therefore investigated more closely. Figures 5.20a+b show two of these clusters imaged at the two pronounced energies (Fig. 5.20a: $U = -100$ mV and Fig. 5.20b: $U = +1400$ mV). These two clusters are mirror symmetric to each other. The mirror axis runs along the [1$\bar{2}$1] direction and is indicated by the white lines. The image at elevated positive bias (Fig. 5.20b) reveals the chirality of each individual molecule ("R" or "L"). Each cluster is composed of entities of both chiral types. For illustrations Fig. 5.20c presents the internal molecular arrangement of the right cluster (in Fig. 5.20a+b) as experimentally deduced. Molecules are aligned as expected from the controlled charge redistribution by the electro-negative chloride. Oppositely charged sides of molecules face each other due to acting Coulomb forces. This results in stabilized molecular units, which overcome the repulsive forces among uncharged molecules. Coulomb forces among molecules are superimposed by local directional molecule-substrate forces, which determine the arrangement of molecules relative to the sub-
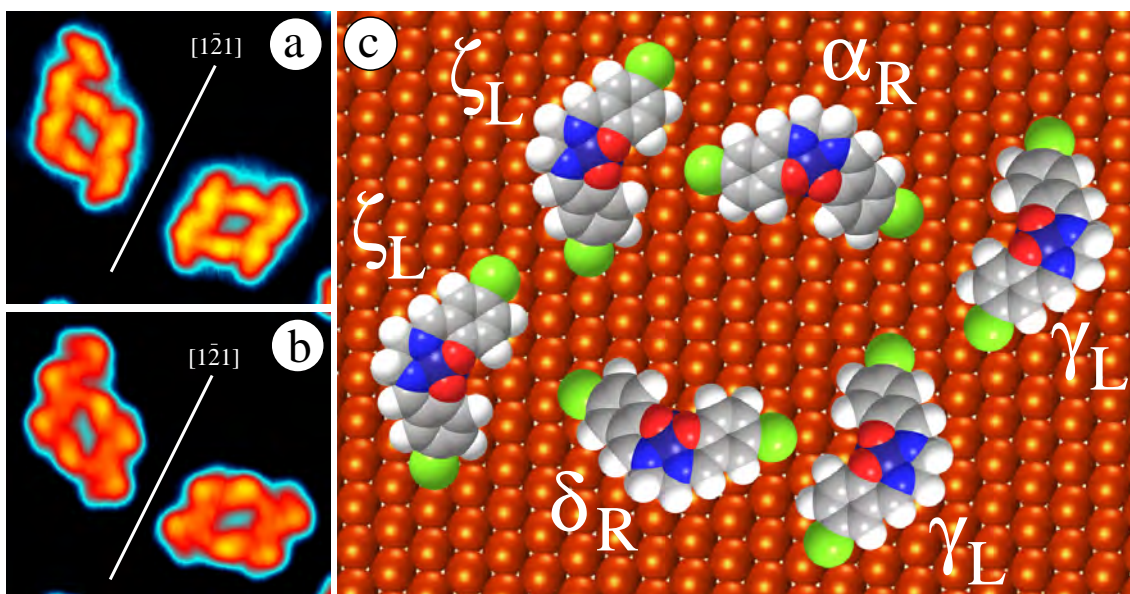
Figure 5.20: Two self-organized Co(5,5'-Cl$_2$-Salen) clusters on Cu(111) imaged at (a) $U = -100$ mV and (b) $U = +1400$ mV. (c) Proposed model for a self-assembled cluster of six molecules. The cluster is composed of both enantiomers with a ratio of 4:2 (STM images: 12×9 nm^2).

strate as for isolated molecules. Nevertheless indications for additional repulsive forces decisive for the actual molecular arrangement in the six membered clusters are present.

Homorace clusters as well as clusters with the molecules α_R and δ_R (see Fig. 5.20c) pointing inwards would result in a closer arrangement of the cluster. Since this was never observed, it is interpreted as a repulsive interaction among the hydrogen terminated sides. The same interpretation holds for observed chain structures and four membered islands.

At an increased coverage, larger self-assembled networks are formed. This is demonstrated in Fig. 5.21a. Large domains with different molecular orientations are observed. A schematic drawing of these domains is shown in Fig. 5.21b with their orientations indicated by arrows. Four different orientations are distinguished in the domains. This is explained by the six different possible variations of the six membered cluster. They act as competing nucleation sites for the network growth and build different oriented domains. Investigating the geometry of the six membered clusters interacting as building blocks for the network on a smaller lateral scale, Fig. 5.21e gives an insight into the alignment. Each building block is from the same chirality and oriented in the same direction. In this way, the Co(5,5'-Cl$_2$-Salen) molecules form a perfectly regular network structure. Depending on the coverage and on defects on the surface, also irregularities in the network structure are observed. Two examples are shown in Figs. 5.21c+d. Induced by a rare variation of the six membered cluster, the network is locally either compressed or stretched. The variation of the building block unit occurs, when an additional row of three molecules extends the cluster to nine species (marked in Figs. 5.21c+d by white circles). This
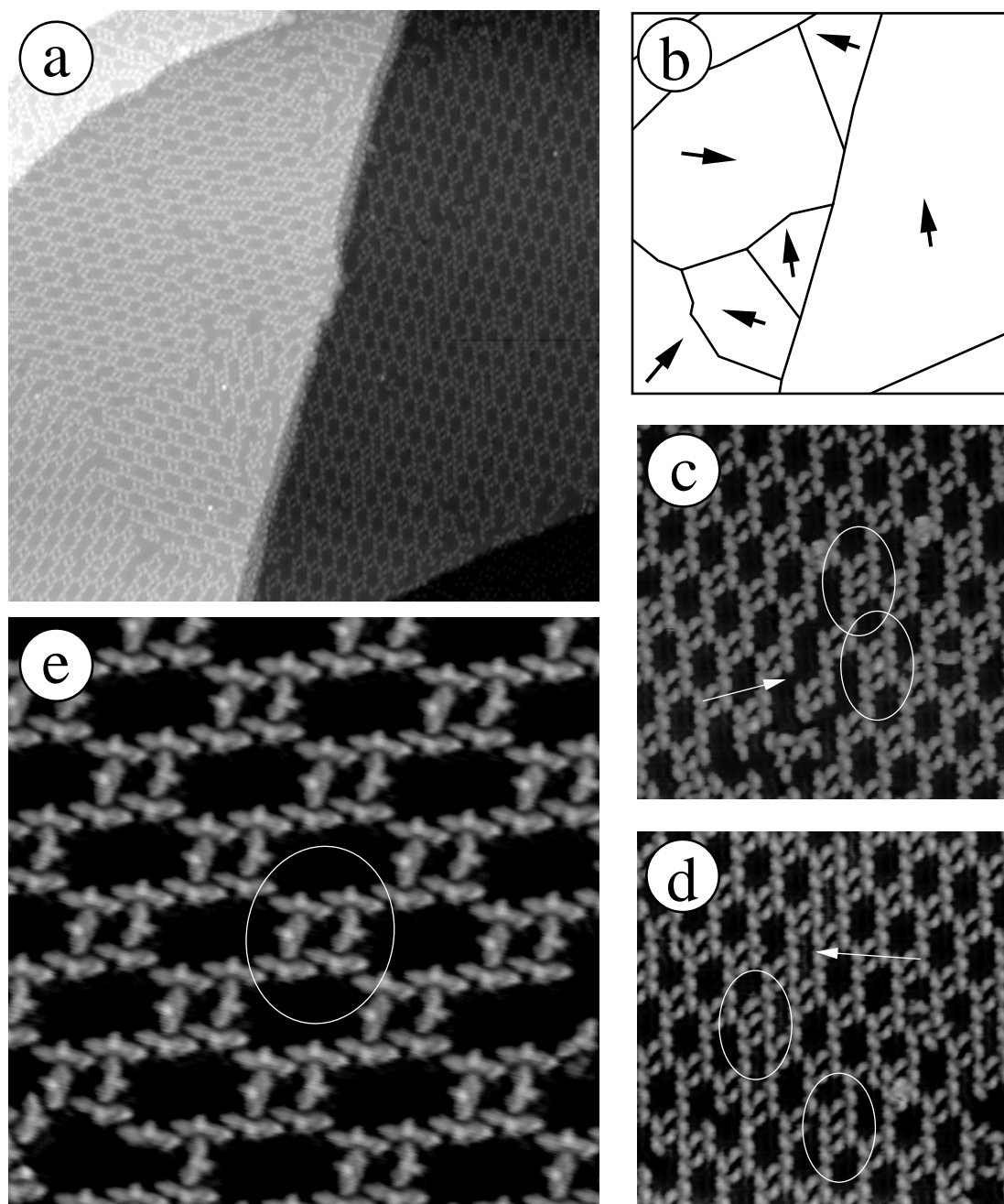
Figure 5.21: Self-assembled network of Co(5,5'-Cl$_2$-Salen) molecules on Cu(111) after room temperature preparation. (a) Large scale overview image showing different domains in the network (100×100 nm^2, $U = -500$ mV). (b) Schematic representation of Fig. 5.21a indicating the directions of the different domains by arrows. (c)+(d) Zoom-in on irregularities in the network indicated by white arrows. They are created by nine membered clusters (white circles), which are rare variations of the normal six membered cluster (20×20 nm^2). (e) Zoom-in on one domain revealing the six membered cluster (white circle) as the building unit of the network (15×15 nm^2, $U = -500$ mV).

difference in size compared to the regular six membered unit is compensated by openings or denser packing (arrows in Figs. 5.21c+d).

5.3   Co-Salen on Cu(100)

For a comparison to the study of Co(5,5'-X$_2$-Salen) complexes on Cu(111), the Co-Salen with hydrogen in the 5,5'-positions is also prepared on a Cu(100) surface. The focus is on the adsorption behavior concerning orientation, hydrogen reactivity and growth for the different substrate lattice. The Cu(100) substrate bears a fourfold symmetry, which was introduced in Sec. 3.1.3.

5.3.1   Orientations on Cu(100)

For the investigation of isolated molecules, a low coverage of Co-Salen was prepared at room temperature. As in the case of Co-Salen adsorbed on Cu(111), molecules stay isolated on the terraces. An exemplary preparation is shown in Fig. 5.22. Single molecules imaged at a low bias voltage of $U = -150$ mV exhibit the same banana-shape with a maximum in the middle as observed on Cu(111).

The C_2-axis of Co-Salen molecules is oriented exactly along one of the two main crystal axes. The slight rotation angle of the Cu(111) case due to chirality is missing, which gives no direct sign of the chirality of Co-Salen molecules. As a consequence of the different surface structure four different molecular orientations on Cu(100) are found. These four different orientations are shown in Figs. 5.22b-e rotated clockwise
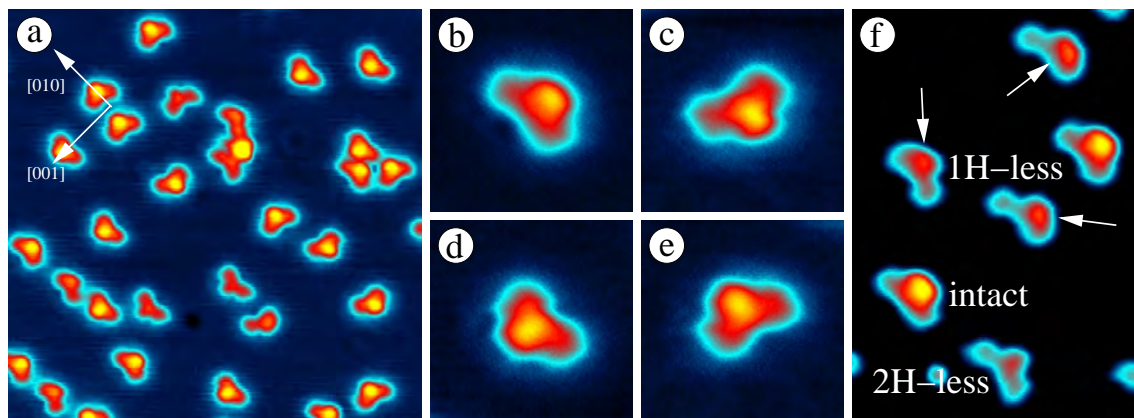
Figure 5.22: (a) Co-Salen on Cu(100) at medium coverage. Molecules exhibit four different orientations with the C_2-axis of the molecules oriented along one of the two main crystal directions. Some of the molecules are identified to be in a state with removed hydrogen atoms from the C$_2$H$_4$-bridge already known from the study on Cu(111) (17×17 nm^2, $U = -150$ mV). (b)–(e) STM images of individual Co-Salen molecules presenting the four different orientations (3×3 nm^2, $U = -150$ mV). (f) Zoom-in on molecules of the same orientation but with different appearances. They are identified as the intact, the single (1H-less) and the double dehydrogenated (2H-less) Co-Salen (6×6 nm^2, $U = -150$ mV).

by 90°. A few of the molecules in Fig. 5.22a appear slightly reduced in height in the STM image. These individuals can be identified as the dehydrogenated states of Co-Salen already known from the study on Cu(111) (see Sec. 5.1.3). For one particular orientation all states, i.e. the intact Co-Salen, the single and the double dehydrogenated Co-Salen are presented in Fig. 5.22f. They are clearly identified from their apparent height and symmetry. The intact and the double dehydrogenated state (2H-less) share the symmetry axis but appear different in height. In the case of the single dehydrogenated state (1H-less), the two enantiomers can be distinguished and are marked by white arrows in Fig. 5.22f. The maximum in apparent height, which is strongly influenced by the top bridge of the molecule, appears for one type on the right and for the other on the left side of the molecule. Why the distinction between the two enantiomeric types of the intact Co-Salen is not possible on Cu(100) in contrast to Cu(111) cannot be explained at this point and additional support from theory is anticipated.

5.3.2 Meta-stable orientations of Co-Salen on Cu(100)

Compared to the four orientations found on a sample prepared at room temperature, additional configurations are observed after low temperature preparation. These are easily displaced by the STM tip, indicating a reduced coupling to the metal substrate. This is demonstrated in Fig. 5.23.

The two molecules on the left in Fig. 5.23a are identified to be in two already known orientations. Their C_2-axes point in the directions of the crystallographic axes of the substrate. The two molecules on the right side of the image exhibit two new orientations. They are rotated by $\sim25°\pm5°$ in comparison to the known orientations. These two orientations are attributed to meta-stable configurations of Co-Salen. When the bias voltage is increased for imaging from $U = +200$ mV (Fig. 5.23a) to $U = +800$ mV (Fig. 5.23b), the energy injected from the tip is sufficient to displace both meta-stable configurations, whereas the known orientations are undisturbed. This effect is reproducibly occurring at voltages above $U = +800$ mV for all observed meta-stable individuals.
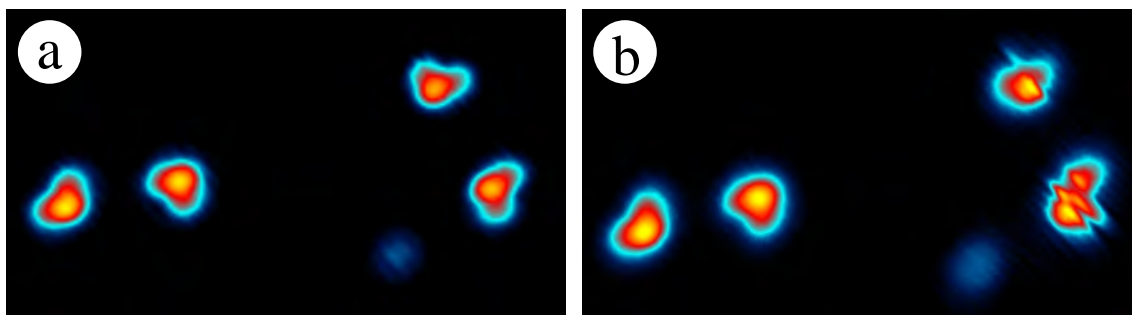
Figure 5.23: Low temperature deposition of Co-Salen on Cu(100). (a) In addition to the four orientations already known from room temperature deposition, additional configurations are observed ($U = +200$ mV). (b) Increasing the bias voltage only to $U = +800$ mV induces enough mobility in the meta-stable states to displace the molecules with the STM tip.

Such meta-stable configurations of Co-Salen were not observed on the Cu(111) surface independent of the preparation conditions. This special role of the Cu(100) facet trapping meta-stable configurations after preparation at low temperatures is also observed for phthalocyanine molecules (see chapter 4).

5.3.3   Growth of Co-Salen on Cu(100)

For a comparison with the growth of Co-Salen on Cu(111), which reveals a repulsion among molecules, Co-Salen is also sublimed on Cu(100) with the sample kept at room temperature. Figure 5.24a shows a Cu(100) surface with a medium coverage of Co-Salen molecules. Comparable to the growth behavior on Cu(111) molecules are mobile during preparation. Therefore, molecules fully decorate step edges and defects without any tendency of self-assembly.
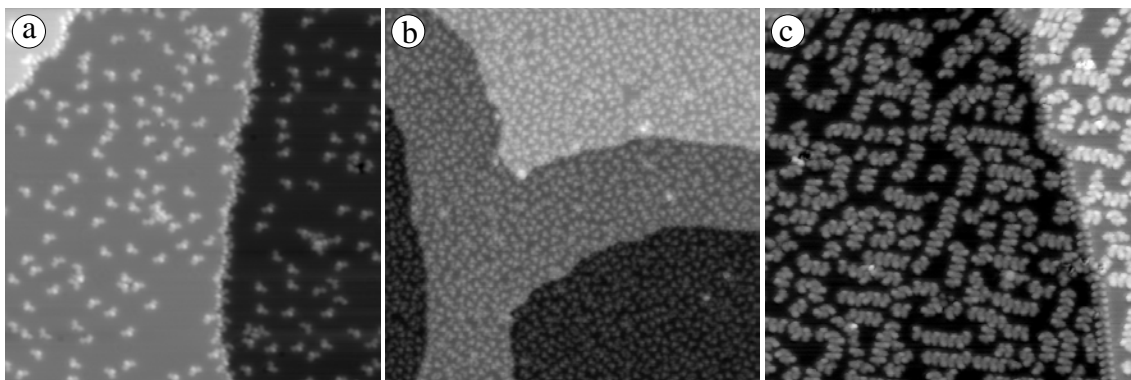
Figure 5.24: Room temperature preparation for low (a) and high (b) coverage of Co-Salen on Cu(100). (a) Only step edges and defects are decorated (40×40 nm^2, $U = -500$ mV). (b) Even at a coverage with nearly no bare substrate left molecules do not form clusters (60×60 nm^2, $U = -150$ mV). (c) After tempering the sample to 200°C molecules form chains, but in addition their appearance is altered indicating a change in their intramolecular structure (35×35 nm^2, $U = -200$ mV).

With increasing coverage still no self-assembly is observed (Fig. 5.24b). This corresponds to the study on Cu(111). Even with a nearly complete coverage of the surface, intermolecular distance is maximized. Tempering the sample completely changes this behavior. After heating the sample to 200°C molecules form chains on the surface, but additionally their appearance changed significantly. The pronounced maximum feature in the center of the molecules observed before heating vanishes as well as the orientation of molecules with respect to the substrate changed. The C_2-axis is now rotated by $\sim 25° \pm 5°$ compared to the original orientations of the intact molecules.

5.4   Co-Salen on NaCl/Cu(111)

For an investigation of molecular properties without hybridization with the states of the copper substrate, Co-Salen is prepared on the NaCl/Cu(111) system as in-

troduced in Sec. 3.2. Co-Salen molecules have a high mobility on NaCl due to their small size.

First, islands of NaCl on Cu(111) of 1–3 ML height are prepared using the preparation method explained in Sec. 3.1. A surface after this preparation is shown in Fig. 5.25a: the copper substrate is covered by patches of NaCl with the thickness of layers varying from 1 to 3. This is reflected in the corresponding line-profile in Fig. 5.25c with the apparent height values already discussed in Sec. 3.1. The area in the upper right corner is of special interest for molecules with high mobility. It offers a big terrace of the first layer of NaCl surrounded by a bilayer border. Co-Salen molecules are now evaporated with the sample in the STM kept at 25 K. Afterwards, the tip is approached to exactly the same spot and molecules are identified on the
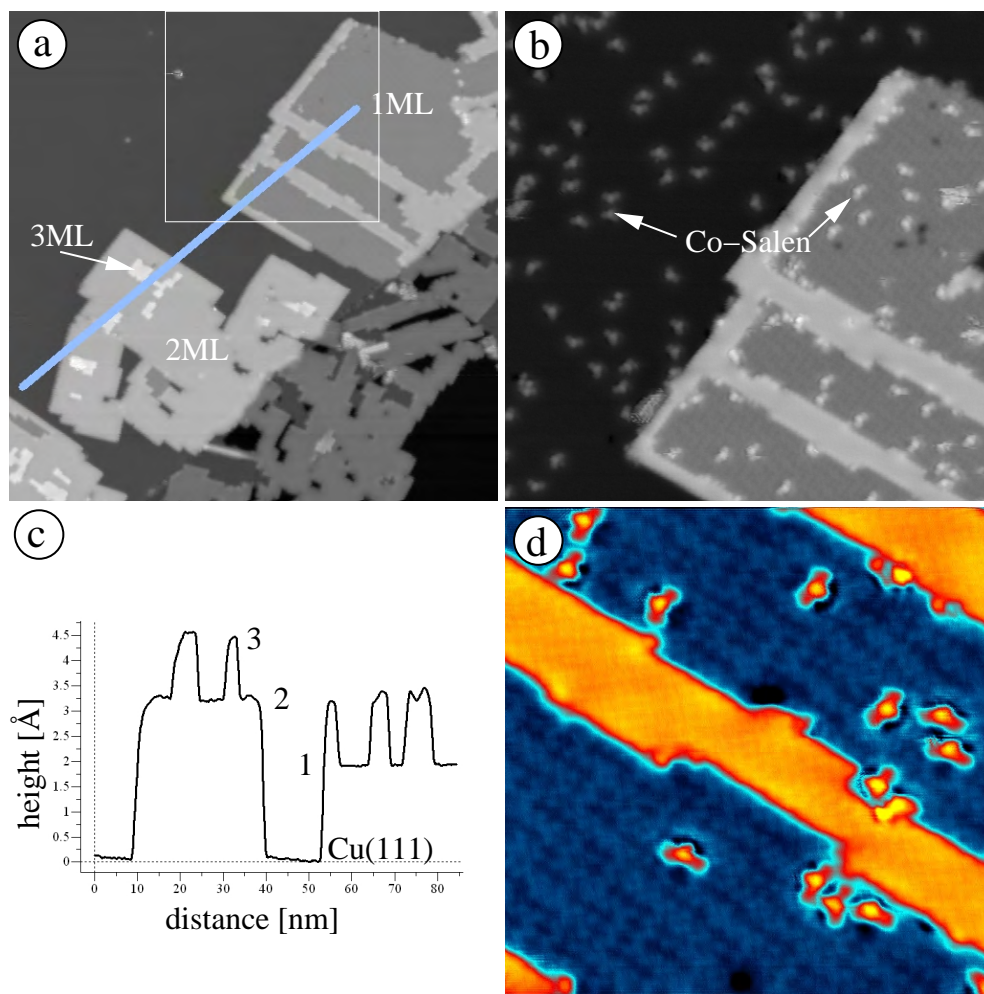
Figure 5.25: (a) NaCl on Cu(111) with a varying thickness of 1–3 layers as indicated. The corresponding line-profile is shown in (c) (95×95 nm^2, $U = +1200$ mV). (b) Area marked in (a) by the white box. The surface is decorated with individual Co-Salen molecules, which can be identified on the copper as well as on the NaCl island (45×45 nm^2, $U = +1200$ mV). (d) Zoom-in on the NaCl island shown in (b) with Co-Salen molecules sitting on the first layer. The Moiré pattern of the atomic lattice is observed (17×17 nm^2, $U = -200$ mV).
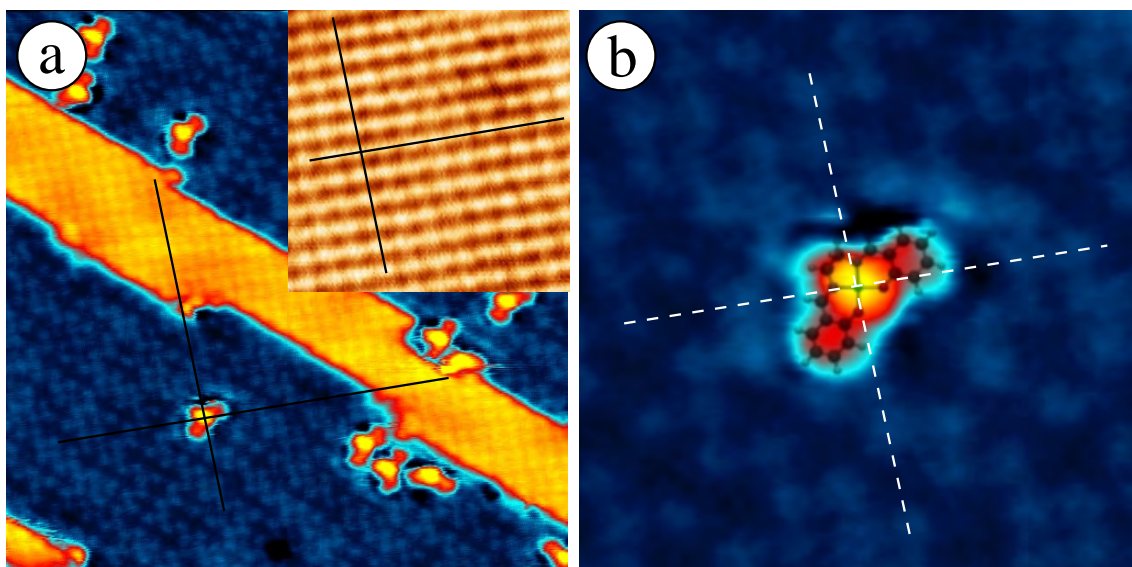
Figure 5.26: (a) Same area as Fig. 5.25d imaged with a different tip. Both NaCl layers are imaged atomically resolved. The chloride atom rows are marked by black lines revealing the adsorption spot of the molecule above a chloride atom (15×15 nm^2, $U = -50$ mV). Inset: Atomic resolution of the NaCl bilayer with the chloride rows marked by black lines (5×5 nm^2, $U = +750$ mV). (b) Zoom-in on Co-Salen on NaCl with the molecular structure superimposed. Marking the chloride atom rows (white dashed lines) reveal the central cobalt atom above a chloride atom of the substrate (4×4 nm^2, $U = -50$ mV).

copper and the first layer of NaCl (Fig. 5.25b, same area as marked in Fig. 5.25a by white box). On the bilayer of NaCl only few molecules are found. They are unstable during imaging and displaced by the tip. Zooming further in on the NaCl island, the typical Moiré pattern of the first layer becomes visible (Fig. 5.25d). The first monolayer of NaCl is divided by a stripe of second layer and molecules are distributed over the two areas of the monolayer. The appearance of the single Co-Salen molecule is similar to molecules adsorbed on both copper facets. The molecular structure is recognized in the banana-shape with a central maximum feature in the apparent height. Molecules are easily displaced or rotated by the STM tip during imaging, reflecting the weak coupling of these small molecules to the NaCl adlayer. Therefore, energy dependent imaging of the same individual molecule without tip changes is not possible. Molecules appear in four distinct orientations reflecting the fourfold symmetry of the (100) terminated NaCl islands. Indications for chirality of molecules are reflected in slight variations of the orientation. Due to the weak coupling and easy displacement of molecules, a clear result could not be gained.

In difference to imaging molecules on metals it is possible to image molecules on NaCl with the substrate appearing atomically resolved at the same time. Therefore, the adsorption site on the NaCl substrate can be extracted from STM images. An example of such an analysis is shown in Fig. 5.26. The same area shown in Fig. 5.25d was scanned with a different tip imaging both layers of NaCl atomically resolved (see Fig. 5.26a). In Sec. 3.1.4 the atomic resolution of NaCl was already discussed. The

chloride atoms appear as bright protrusions shifted by half a row between the first and second monolayer. The inset in Fig. 5.26a shows an area of the second layer of NaCl imaged on the same island. The directions of the chloride rows are recognized and marked by black lines. The same directions are then adapted to the Co-Salen molecule on the first layer of NaCl in Fig. 5.26a. The black lines are adjusted to match the chloride atoms on the first layer and the rows in-between on the second layer. This is more accurate than matching the chloride rows directly on the first monolayer due to the strong Moiré pattern. Zooming in on the Co-Salen with the molecular structure superimposed the lines of the chloride atom rows reveal a perfect match between the cobalt center atom and a chloride surface atom (Fig. 5.26b). The line markers are changed to white dashed lines for better contrast.

Chapter 6

Iron TriPhenylCorrole (FeTPC)

Corroles are tetrapyrrolic macrocycles that are closely related to porphyrins, with one carbon atom less in the outer periphery and one NH proton more in the inner core (see Fig. 6.1).
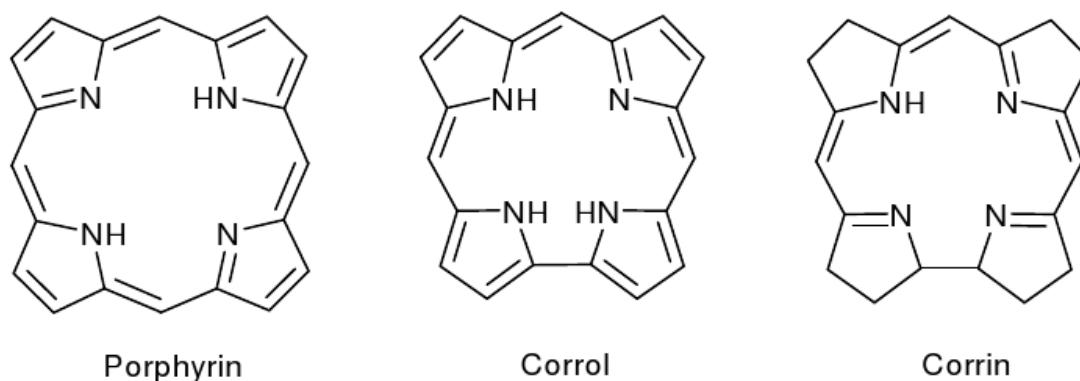
Figure 6.1: Macrocycles of the three closely related molecules: Porphyrin, Corrole and Corrin.

The first successful synthesis was done by Johnson and Kay in 1964, where they got corrole as an intermediate product of their initial synthesis of corrin [114]. This also closely related corrin is a part of Vitamin B_{12} [115]. The contracted coordination of the core and the fact that they act as trisanionic ligands leads to a special feature of corroles relative to porphyrins, i.e., the stabilization of metal ions in high oxidation states [116]. The latter feature leads to more intense metal-ligand interactions in metal chelates and to interesting electronic structures. Corroles have been developed in the past decade to be a very accessible, easily tunable compound with many potential applications in material science and catalysis [117–121].

The study on corrole molecules presented in this thesis was done with derivatives of the triphenylcorrole with an iron ion as metallic center. The molecular material was synthesized by the group of Prof. Martin Bröring of the University of Marburg. There is a zoo of iron(III)-triphenylcorrole (FeTPC) [122–126] derivatives with different axial groups connected to the iron center. The molecular structures of the four complexes **1** – **4** of FeTPC selected for this study are presented in Fig. 6.2.
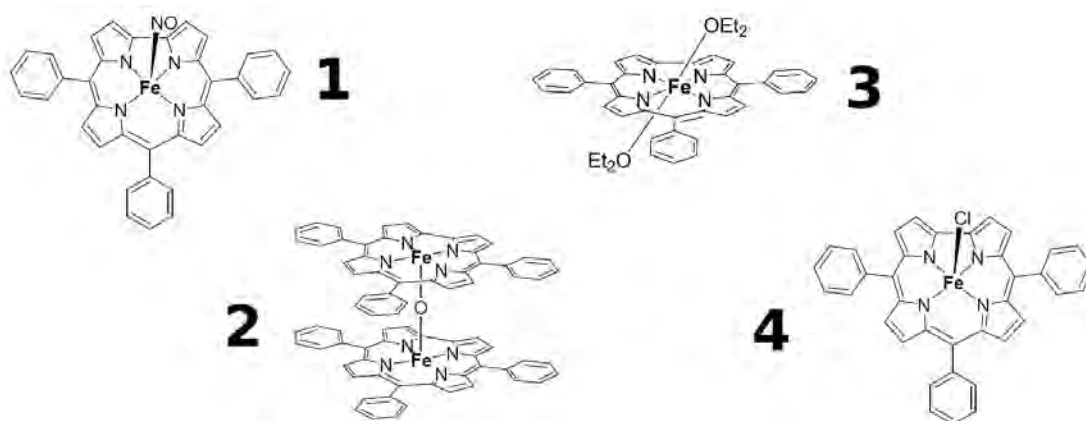
Figure 6.2: Iron(III)-triphenylcorroles with different axial groups used in this study.

They have different properties in bulk or gas phase concerning chemical behavior and magnetism. Their properties on surfaces were not studied so far.

As a first step, the adsorption behavior of these four FeTPC derivatives evaporated in UHV on a metallic surface is investigated (see Sec. 6.1), followed by a comparative study of iron-corrole molecules on the different substrates introduced in Sec. 3.1, i.e. Cu(111), Cu(100) and NaCl/Cu(111) concerning appearance, self-assembly and spectroscopy.

6.1 Adsorption of four different derivatives of FeTPC on Cu(111)

Figure 6.3 gives a comparative overview on representative images after room temperature depositions of all four FeTPC complexes used in this study (see also Fig. 6.2). Molecules are prepared as discussed in detail in Sec. 3.2.

Fig. 6.3a shows the result of a preparation of the FeTPC complex **1** with NO as axial group. Entities made of one to three individuals are recognized on the surface. The result of the preparation of the double-decker complex **2** appears similar (Fig. 6.3b). The coverage is lower compared to complex **1**, but also here entities of one and two individuals are observed, which have the same appearance as complex **1** (compare single and double entities marked by white circles). For complex **3** with the two Et_2O-groups, the preparation result is different (Fig. 6.3c). Double and triple entities are still identified, but additionally patches with stripe patterns are observed. A similar picture results from the STM image of complex **4** with chloride connected to the iron ion (Fig. 6.3d). The stripe patterns in both preparations of complex **3** and **4** follow the crystallographic axes of the hexagonal substrate.

The similar appearance of complexes **1** and **2** on the surface is a sign for the decomposition of the double-decker complex **2** with oxygen as connecting group. This decomposition leads either to two unequal components with and without oxygen connected to the iron ion or to two equal components of pure FeTPC with an ad-
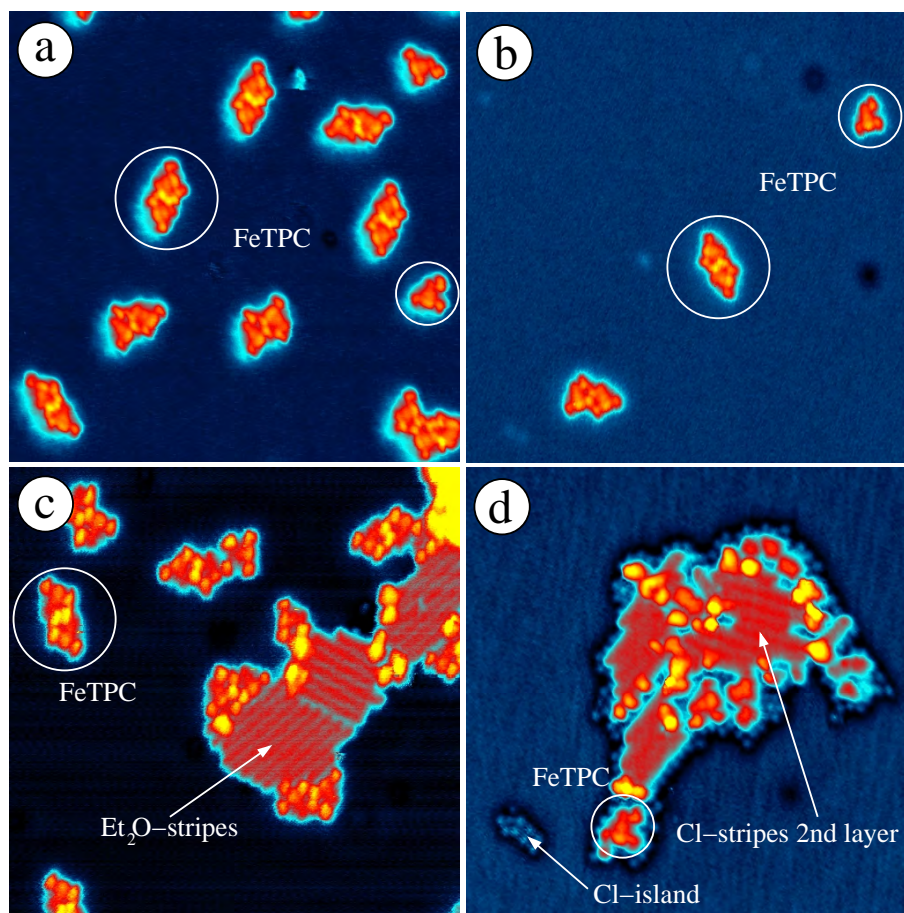
Figure 6.3: Topographic images of FeTPC molecules with (a) NO, (b) O, (c) Et$_2$O, and (d) Cl as axial groups deposited on a Cu(111) surface. (18×18 nm^2, $U = -1000$ mV).

ditional free oxygen. As the individuals on the surface after preparation of complex **2** appear all alike, the latter case is assumed. The comparison to the result of the complex **1** preparation corroborates this assumption. The axial groups of complexes **1** and **2**, i.e., O and NO cannot be identified by STM, because of their same size and appearance as other typical adsorbates (e.g. carbon or oxygen) on the copper surface.

After a preparation with complex **3**, the surface was observed as seen in Fig. 6.3c. The complex also decomposes during preparation and parts of the Et$_2$O-groups form islands on the copper surface with a distinct stripe pattern. This pattern is oriented along the closed packed rows of the Cu(111) surface. The exact moiety taking part in the formation of the striped islands is speculative, but the origin is definitely the Et$_2$O-group of the source. Individual FeTPC molecules are clearly identified, bearing the same appearance as complexes **1** and **2**. They sit at the sides of the Et$_2$O-islands or take part in the formation of double and triple entities.

A similar behavior is observed for chloride as axial group. The chloride splits off already during heating of the molecules in the Knudsen cell. This was also reported for iron porphyrin molecules with chloride connected to the iron ion [48]. It
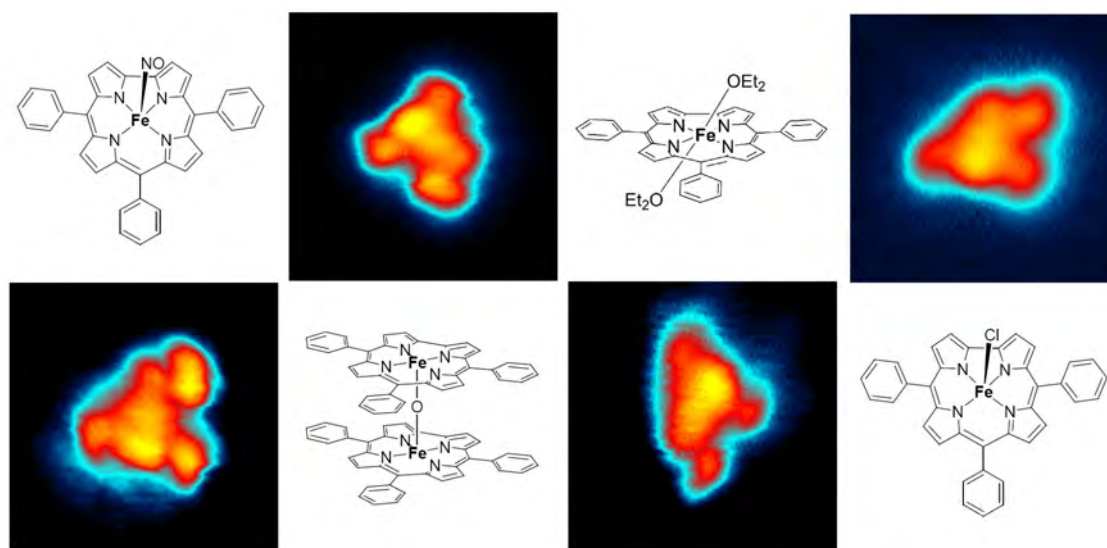
Figure 6.4: Iron(III)-triphenylcorroles with different axial ligands employed in this study. The corresponding STM image is shown above / below.

evaporates much easier than the rest of the molecule, which is seen in the unbalanced amount of iron-corrole molecules compared to chloride atoms (see Fig. 6.3d). The chloride forms islands on the copper surface, reflecting the hexagonal symmetry of the substrate. The second layer is also showing a stripe pattern in the directions of the Cu(111) axes, as in the case of the Et_2O-groups. The FeTPC molecules sit on the first layer of chloride, which is also a proof for the decomposition of the molecule during the heating in the evaporator. Degassing the molecular source for a whole week changes the ratio between chloride and corrole molecules and favors the molecules more and more. This was tested by daily preparations. After one week of degassing, barely no chloride could be detected on the surface and FeTPC molecules sit on the bare copper instead of chloride islands.

Comparing single molecules of all four complexes on Cu(111), their appearance is nearly identical. Variations in the appearance can be attributed to the actual tip shape. Figure 6.4 shows STM images of individual FeTPC molecules adsorbed on a Cu(111) surface prepared from the different sources with the corresponding chemical structure depicted above / below. Molecules exhibit a cigar shaped body with three ellipsoids attached. These ellipsoids are identified as the three phenyl rings. The interpretation is that the observed individuals are all the same metal-organic compound with the axial groups detached during evaporation. As a result, FeTPC molecules appear without axial group on the surface. Therefore, in the following sections the issue of the axial groups is omitted and molecules are simply denoted as FeTPC independent of the originating source.

6.2   FeTPC molecules on Cu(111)

First, single isolated molecules adsorbed on Cu(111) in terms of appearance and conformation are addressed. Afterwards, results concerning self-assembly and spec-
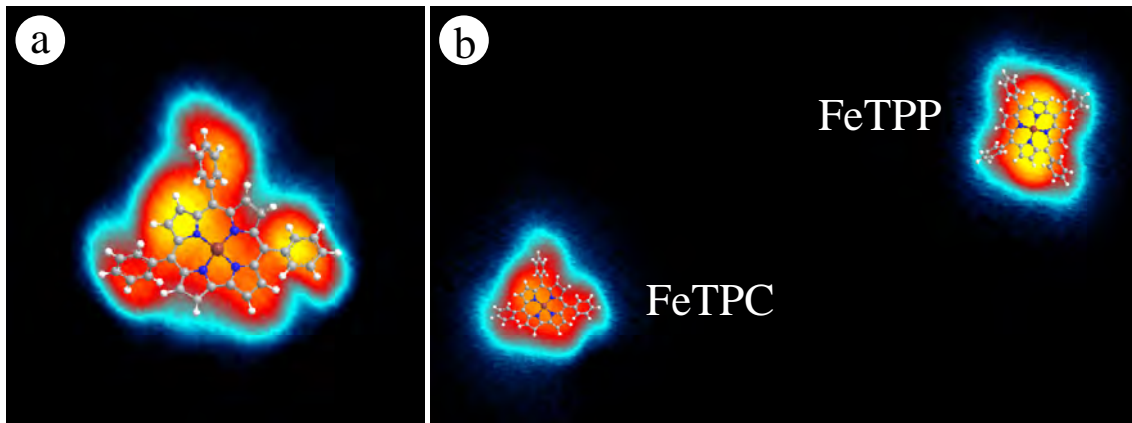
Figure 6.5: (a) High-resolution topographic image of an individual FeTPC molecule adsorbed on a Cu(111) surface. The overlaid model is scaled to the image size and illustrates the proposed saddle conformation of the corrole macrocycle with twisted phenyl legs. (4×4 nm^2, $U = -1000$ mV). (b) FeTPC molecule in comparison to a coevaporated FeTPP molecule on Cu(111) (10×6 nm^2, $U = -1000$ mV)

troscopy are presented and discussed.

6.2.1 Individual FeTPC molecules

Figure 6.5a presents a high-resolution image of an isolated FeTPC molecule on a Cu(111) surface. FeTPC appears without any symmetry. Each molecule has three dominant outer and elongated protrusions at its opposite ends which represent the phenyl legs and one unoccupied end, which breaks mirror symmetry. For the corrole center, we find an accentuated backbone in cigar shape with one side highlighted. This side is located between two outer protrusions. The interpretation of the adsorption geometry follows in a natural way the observed symmetry. The corrole macrocycle is deformed into a saddle conformation and all three phenyl legs are twisted relative to the surface normal. The accentuated backbone reflects the upward bent pyrrolic units of the corrole macrocycle, whereas the other pyrrolic units point towards the surface plane. Additionally, the macrocycle is slightly tilted relative to the plane of the substrate due to the asymmetry of phenyl legs with one side lifted by the supporting phenyl legs. This interpretation is demonstrated by the overlaid structure of FeTPC, and is in line with the interpretation of the adsorption of tetra-phenyl porphyrins (TPP) [127]. Both, FeTPC and FeTPP appear with similar shape (Fig. 6.5b) but with one phenyl leg less for FeTPC due to the exchange of the porphyrin against a corrole core.

A major consequence of the proposed bending of the macrocycle and twisting of phenyl legs is surface supported chirality [128]. The experimental manifestation is demonstrated in Fig. 6.6. Exactly 12 different orientations and conformations are identified for the adsorption of FeTPC on Cu(111). Six different orientations of the backbone and two mirror symmetric conformations of phenyl legs for each orientation are found. The backbones of the macrocycle are perpendicular to the closed packed rows of the underlying substrate (as previously determined by atomic resolution
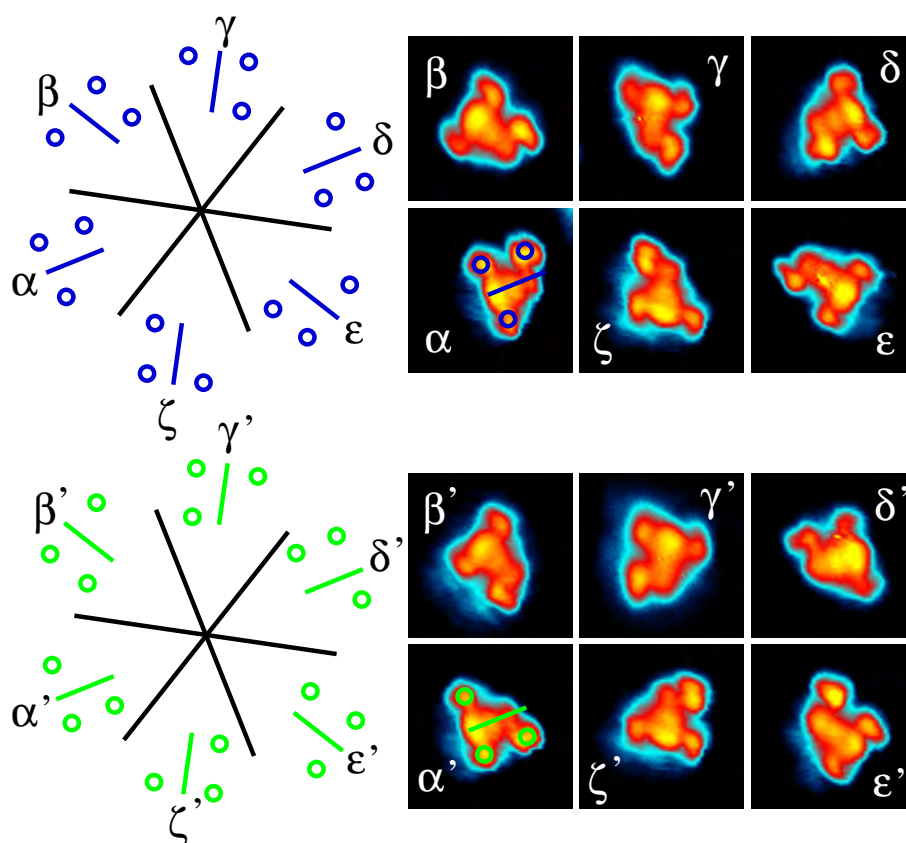
Figure 6.6: Representation of the different orientations and conformations of FeTPC on Cu(111) in STM images. For orientation, all 12 geometries (6 enantiomeric pairs shown in blue and green, respectively) are schematically indicated by the backbones (line) and phenyl legs (circles) along the crystalline axes of the Cu(111) substrate (black lines, all STM images 3×3 nm^2, $U = -1000$ mV).

data) and the pyrrolic units which are bent towards the substrate, are parallel to one of the crystallographic axes of the substrate. Whereas the six orientations reflect the symmetry of the substrate (α, β,...) the two different conformations reflect chirality (α vs α' etc.).

6.2.2   Manipulation of FeTPC on Cu(111)

Using the STM tip as a manipulation tool [129, 130], it is possible to switch iron-corrole molecules between different conformations and orientations. An exemplary series of manipulation steps is depicted in Fig. 6.7 where an FeTPP molecule is used as a topological marker on the surface. In the starting configuration (Fig. 6.7a), the FeTPC molecule is adsorbed in an orientation previously denoted as α. Then, the STM tip is precisely positioned above the center of the molecule and lowered towards the adsorbed molecule ($\Delta z = 0.8$ Å$\pm$0.2 Å). Under the reduction of the tip-sample distance the molecule starts interacting with the tip and rotates from orientation α by 60° into orientation β (Fig. 6.7b). Additional increase of tip-molecule interaction by further lowering the tip ($\Delta z = 1.0$ Å$\pm$0.2 Å) can even induce a change of chirality,
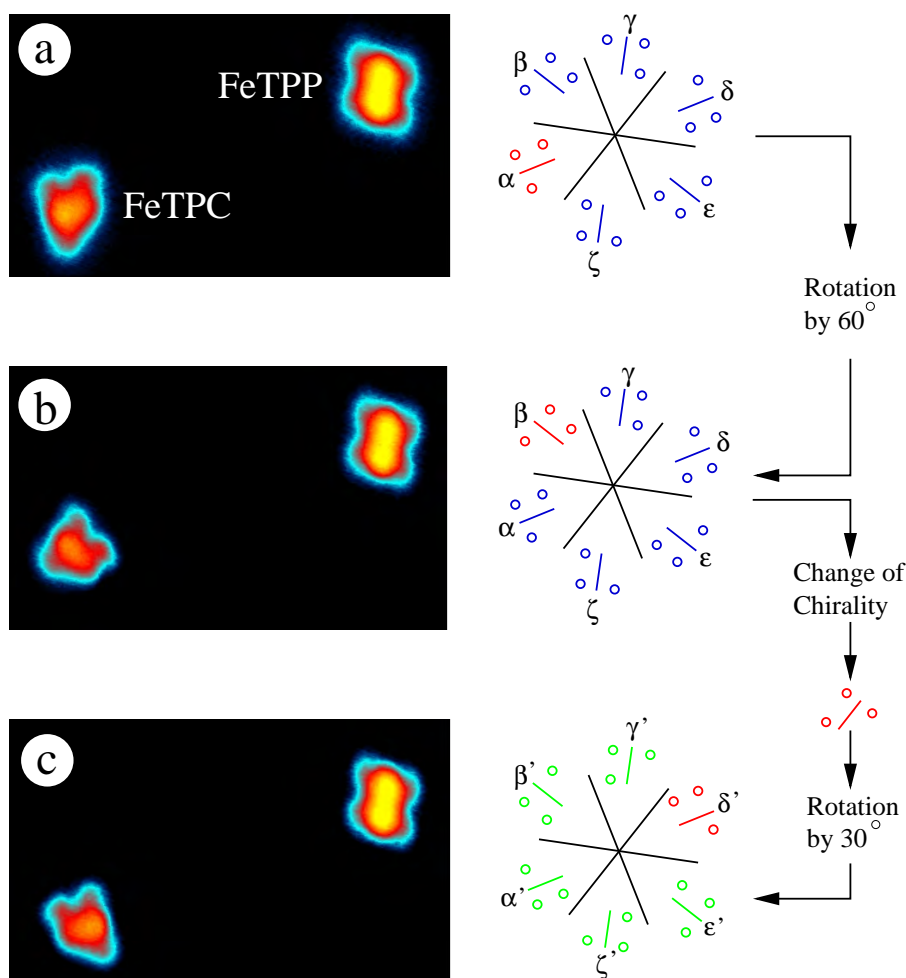
Figure 6.7: Images of the same area taken consecutively after manipulation of the FeTPC molecule. The FeTPP molecule acts as a reference spot. (a) FeTPC and FeTPP molecule on a Cu(111) surface after coevaporation. (b) After manipulation with the STM tip, the FeTPC molecule turned by 60° clockwise. (c) Another manipulation led to a turn of only 30° but with a change of the saddle to the chiral form (all images 10×6 nm^2, $U = -1000$ mV).

here from orientation β into δ' without any destruction of the molecule itself.

With a different method of manipulation, it is possible to switch molecules into an alternative conformation. The starting geometry of the molecule is shown in Fig. 6.8a. Again, the tip is positioned over the center of the molecule and, now, the voltage is ramped up to +4V. After manipulation, the molecule exhibits mirror symmetry (see Fig. 6.8b) with the phenyl groups being fully symmetric. The exact conformation stays speculative and cannot be determined by STM, however, the symmetry and the apparent size of the imaged FeTPC give an indication; the corrole macrocycle is either in a planar geometry or in a so called dome conformation with all pyrrolic units bent downwards. The reduced apparent size of FeTPC can be interpreted in the direction of the latter case with the electron cloud above the molecule lowered at the edges towards the surface. In both cases, steric interaction
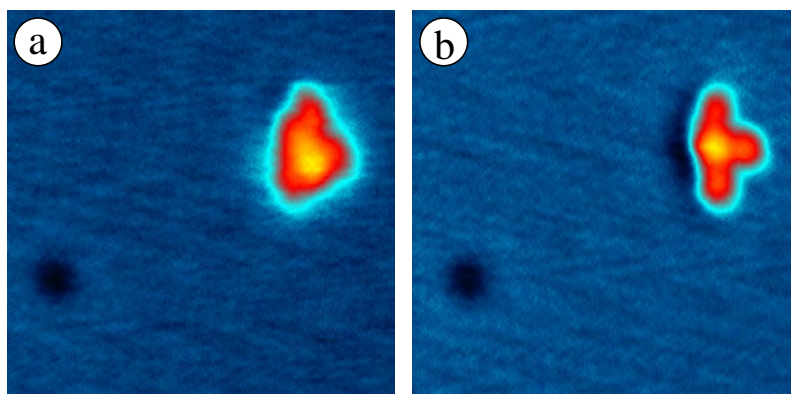
Figure 6.8: An individual FeTPC molecule was manipulated with the STM tip from (a) the saddle into (b) a symmetric conformation. An adsorbate in the lower left corner acts as a marker. The molecule is turned by a few degrees to fit on the surface with the new conformation. (8×8 nm^2, $U = -1500$ mV).

between hydrogen atoms of the phenyl groups and the pyrrolic units will favor a more perpendicular orientation of phenyl legs than for a saddle conformation (for comparison of the proposed planar configuration see Sec. 6.4). This way of manipulation inserts a lot of energy into the molecule, which is needed to change the conformation of the molecule against the strong interaction with the surface. This is not always reproducible and sometimes leads to the decomposition of the molecule during manipulation.

6.2.3   Self-assembly of FeTPC

To study the self-assembly of FeTPC, molecules were deposited onto the room temperature Cu(111) surface. Molecules are mobile on the surface at room temperature and form self-assembled structures. A characteristic STM image of adsorbed FeTPC molecules on Cu(111) is presented in Fig. 6.9a. In contrast to porphyrin molecules, which form large self-assembled islands on metallic surfaces at room temperature (see Sec. 3.2.2 and [57, 80]), FeTPC molecules predominantly assemble in pairs, so called duplex structures.

Four structurally different duplex aggregates A–D are present on the hexagonal surface. They differ in the number of appearance, the relative orientation of the constituting FeTPC moieties, and by the site of aggregation. Structures A and B are C_2 symmetric, while no symmetry can be found for the duplex structures C and the very rare D. For convenience, the exemplary images in Figs. 6.9c-f were selected with the top molecules of the aggregates always in the same orientation (δ as defined in Fig. 6.6, for the single molecule compare Fig. 6.9b). In the case of A and B, molecules with the same chirality are involved (δ and α in Figs. 6.9c+d). Structure C is made of FeTPC molecules with different chirality (δ and δ') and duplex D consists of molecules in exactly the same arrangement (twice orientation δ in Fig. 6.9f). Therefore, duplex formations A and B exist in 6 and C and D in 12 enantiomeric variations according to the 12 different orientations of the individual FeTPC molecules (see Sec. 6.2 and Fig. 6.6) and the different symmetries of the
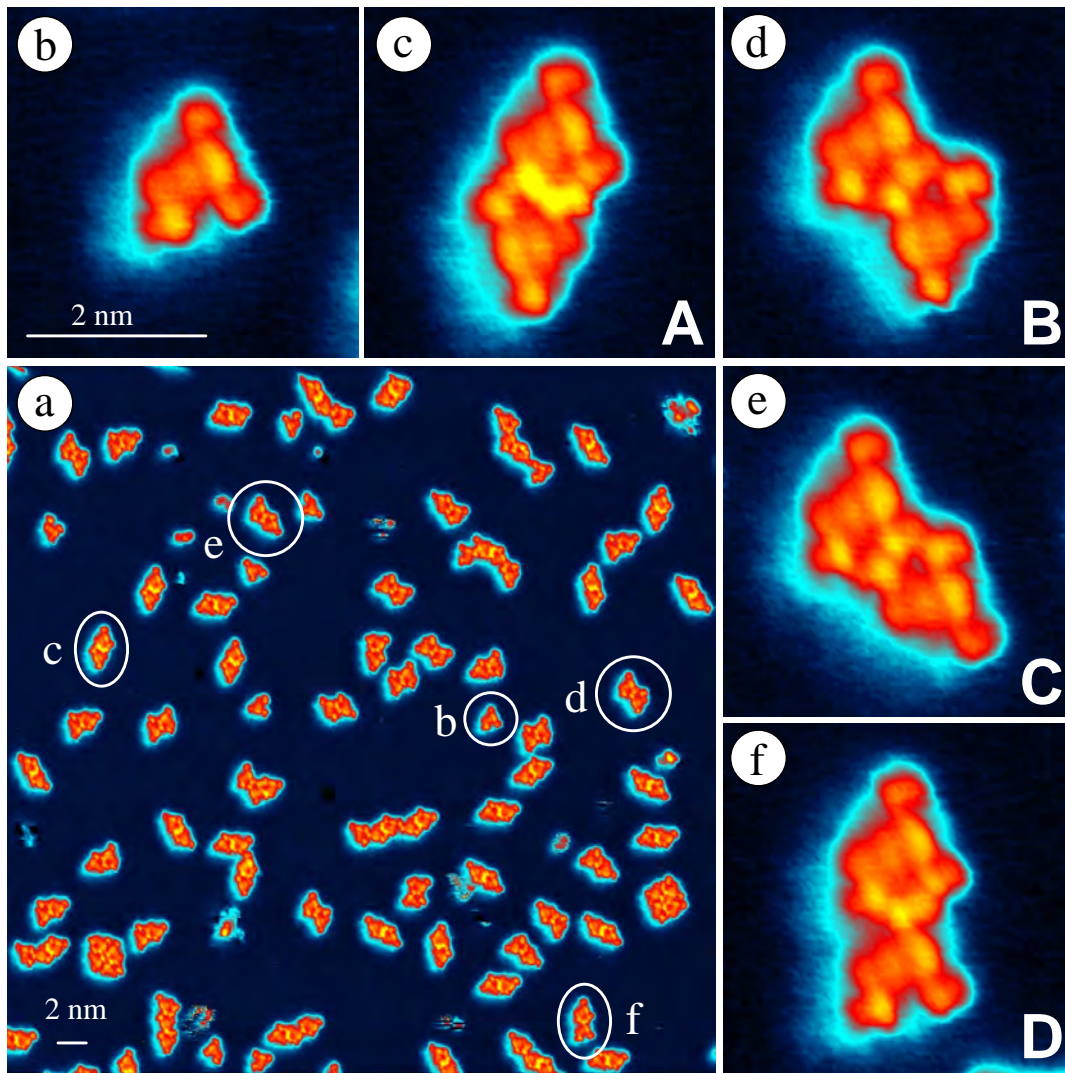
Figure 6.9: (a) STM image of FeTPC on Cu(111) (50×50 nm^2, $U = -1000$ mV). (b)-(f) show a single FeTPC molecule along with characteristic duplex structures A–D as enlarged from (a).

duplex structures. Due to their equal status this difference in orientation is neglected and in the following the duplex structures are only referred to as A–D.

adsorbates	#	adsorbates	#
monomer	24	3mer (A+D)/(A+E)	9/9
2mer A	75	3mer (B+D)/(B+E)	2/0
2mer B	23	3mer (C+D)/(C+E)	1/1
2mer C	38	4mer (C+C)	3
2mer D	3		
2mer E	0		

Table 6.1: Frequencies of appearances for different FeTPC aggregates (enantiomeric forms not resolved).
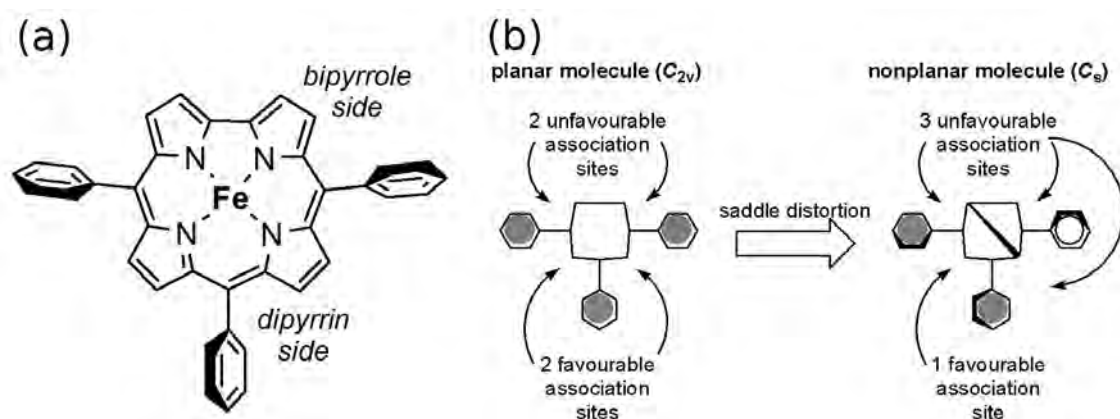
Figure 6.10: (a) Chemical structure of 5,10,15-Triphenylcorrolatoiron (FeTPC). (b) Comparison of favorable and unfavorable association sites for a planar and a nonplanar FeTPC molecule.

Table 6.1 summarizes the numbers of duplex forms counted on a representative 6700 nm^2 area of the surface.

After revisiting the structure of the FeTPC molecule, the difference to the parent porphyrin molecule becomes clear. Compared to TPP molecules the corrole molecule is missing one phenyl ring, leading to two unequal sides for interaction with other molecules (see Fig. 6.10a). The bipyrrole side offers two pyrrolic units and no phenyl leg leading to an open access directly to the macrocycle in contrast to the dipyrrin side, where connections between two phenyl legs are possible. Including the saddle deformation of the molecules on the surface, which changes the symmetry from C_{2v} of the planar geometry to C_s (see Fig. 6.10b), the similarity of the two association sites on the dipyrrin side changes.

Figure 6.11 sketches the arrangements of the different duplex structures including
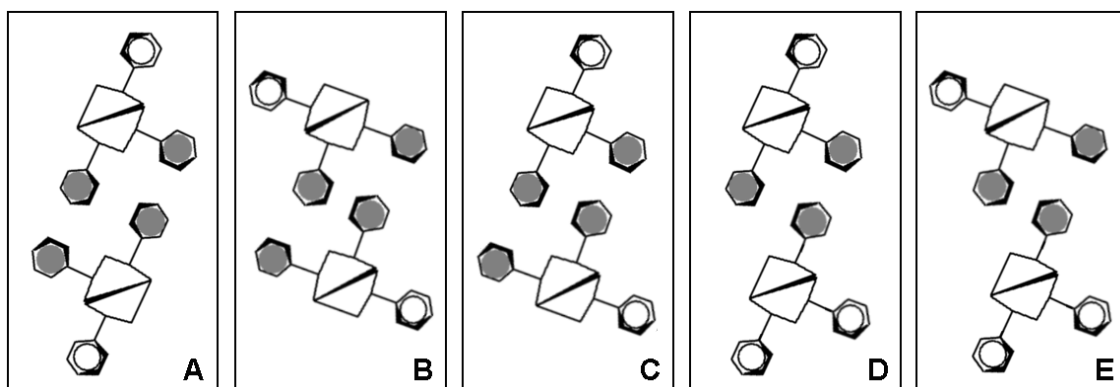
Figure 6.11: Sketches of coupled duplex configurations with four (A–C) and three (D and E) interacting phenyl groups. Interacting phenyl groups are indicated by gray dots, non-interacting by open circles. The backbone of the saddle distortion is indicated by the wedged line in the structures. The rotation of the phenyl rings out of the molecular plane is shown with the black border pointing towards the observer.

the asymmetry of the association sites and the deformation of the macrocycle into the saddle conformation (wedged line indicating saddle). Apparently, the dipyrrin half of the molecules is favored over the bipyrrole half with respect to intermolecular interactions. If two FeTPC molecules are associated at the respective dipyrrin sides, the interactions of four phenyl side chains (dark dots in Fig. 6.11) are observed. This is the case for the more abundant forms A–C, while in D one of the monomeric units binds via the bipyrrole side with only one phenyl group. An interaction similar to duplex D should be found in the predicted duplex E, but was observed during the experiments only in assemblies with higher numbers of participating molecules, i.e. chains of three and more molecules. The small number of observed examples of D and the failure of observing E is in line with the expectation of a lower association energy in these cases.

While duplex forms D and E are rare, duplex A is found in higher numbers than expected. In addition, an intense feature in the apparent height is detected for A at the site of interaction between the two FeTPC molecules. This increase in apparent height is not observed for B–D (this is also expected for E). The particular orientation of the FeTPC units in A seems to allow a slightly different and energetically favored duplex configuration, presumably due to minor differences in the duplex metrics.

Superimposing the STM images from Figs. 6.9c-f with the hexagonal lattice of the Cu(111) substrate and comparing the distances between the molecules in the different duplex formations, the special status of duplex structure A becomes obvious. The superimposed lattice of the copper substrate is aligned with the iron atom over a top position, according to findings of Auwärter *et al.* concerning the adsorption site of porphyrin on Cu(111) [131], but the following argumentation also holds for any other adsorption site.

The yellow circles mark the position of the copper surface atoms, the copper atom below the iron ion of the FeTPC molecule is marked in blue (Fig. 6.12). The adsorption geometry concerning the lattice atoms is exactly the same for duplex structures B–D leading to a distance between the iron atoms of the molecules of 13.5 Å. In case A the adsorption geometry is different and the distance between the molecular centers is reduced to 11.2 Å. This can lead to a different deformation of the phenyl legs involved in the coupling in duplex A compared to B–D. This is
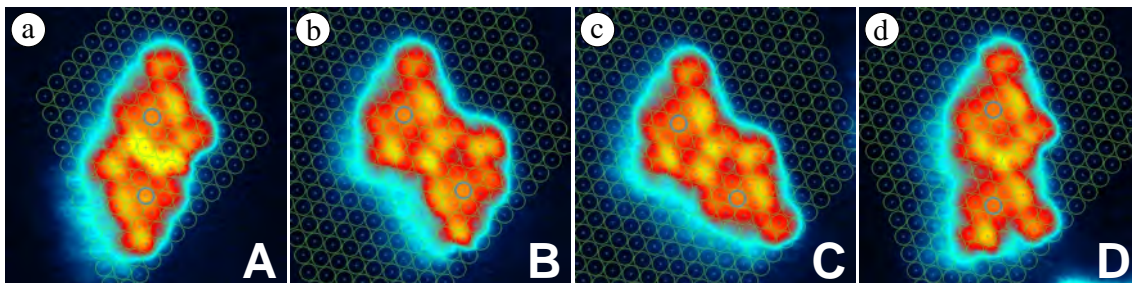
Figure 6.12: FeTPC duplex arrangements A–D taken from Fig. 6.9 superimposed with the hexagonal structure of the Cu(111) lattice. The copper atoms are symbolized by yellow circles (4×4 nm^2, $U = -1000$ mV).
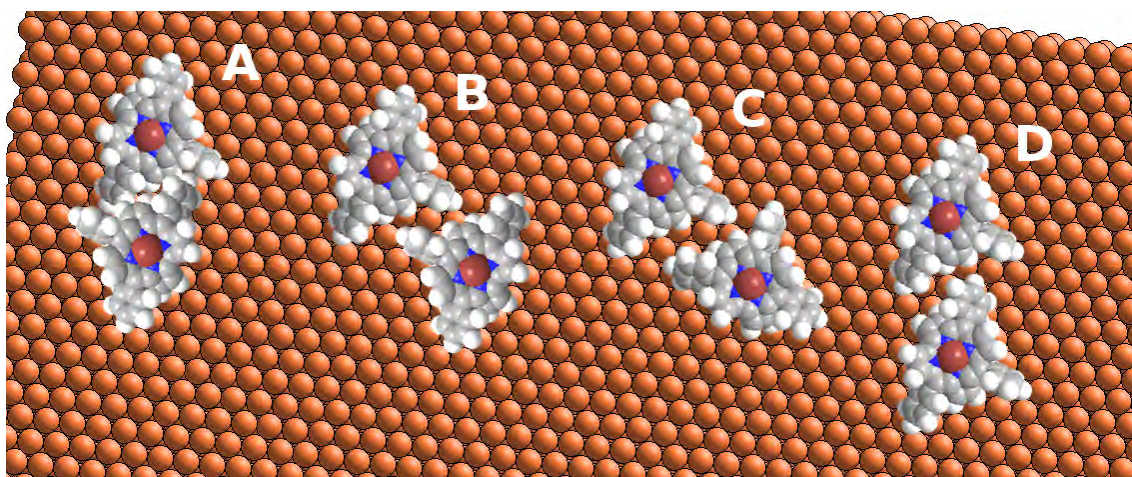
Figure 6.13: Model of the four FeTPC duplex arrangements A–D on the Cu(111) surface derived from Fig. 6.12.

further investigated using spectroscopy measurements to deduce the topographical nature of this increased intensity from an increase in electron density (see Sec. 6.2.4).

Figure 6.13 shows the duplex arrangements of molecules on the Cu(111) surface as experimentally deduced. The representative structures of the molecules are scaled to fit the model of the copper surface.

The macrocycles of FeTPC molecules are not flat but display a saddle distortion on the surface, and the two components of a given duplex always contain parallel saddle axes, indicated by the wedged line in Fig. 6.14. Apparently, the configurational information is transferred from one molecule to the neighbor during the association process, and this recognition of the non-planar distortion mode plays a vital role in the stabilization of the duplex arrangements. A duplex formation with saddle axes perpendicular to each other would only be possible on the hexagonal surface with additional orientations of at least one participating molecule. This was not observed on the Cu(111) surface and the existence of this possibility will be investigated on the Cu(100) surface (see Sec. 6.3.2).

Besides the duplex forms described above, also aggregate forms appear with a higher number of participating molecules. Other than for tetraphenylporphyrin derivatives (TPPs), however, these aggregates tend to stay small and isolated, and no trends to form large ordered domains have been detected for FeTPC. Figure 6.14 presents three typical members of this group, two trimeric forms and one tetrameric ensemble. Both trimers contain one of the stable duplex forms A–C (for B see table 6.1) and one additional FeTPC molecule, which is bound to one of the bipyrrolic sides of the respective duplex (association type D; E is also found, see table 6.1). The tetramer consists of a weakly associated dimer of the self-complementary duplex structure C.

The preference of FeTPC to form duplex structures on a surface can be rationalized by a three-dimensional analysis of the saddle distortion. In order to visualize the effect of symmetry reduction upon the association interaction of molecular systems, a fictitious transition from a symmetric 2D to a distorted 3D molecular structure of
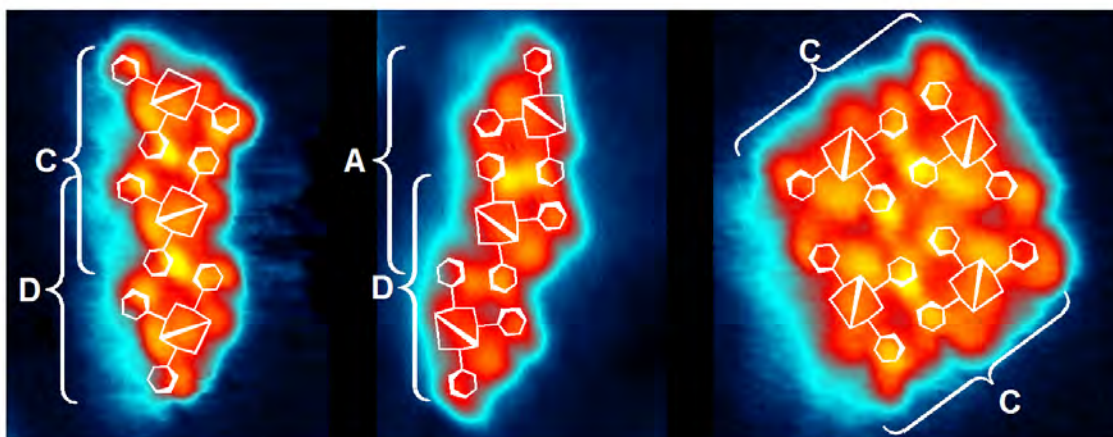
Figure 6.14: Representative STM images of higher aggregates (3mer, 4mer) with simplified structures superimposed to indicate coupling configurations. The assemblies shown are recognized as C+D, A+D and C+C with the notation used in table 6.1 (3×5 nm^2, resp. 5×5 nm^2, $U = -1000$ mV).

FeTPC is shown in Fig. 6.10b. Two equally favorable sites for association processes exist at the dipyrrin side of the planar molecule. With the saddle distortion this number of favorable sites is reduced to one. Stable duplexes of such asymmetric species should be associated at this position and thus block all binding sites at the perimeter. Any further aggregation is difficult and directed to unfavorable positions at either the bipyrrole side (as in duplex D) or in the saddle axis at the dipyrrin side (as in the tetramer). The observed preferential formation of three distinct duplex forms as the thermodynamically stable products of the self-assembly process on Cu(111) can thus be attributed to the differentiated binding at the bipyrrole and the dipyrrin side, and to the decisive influence of the non-planar distortion of FeTPC on the surface. This behavior is fundamentally different from all observations on TPPs, which exhibit four (almost) equivalent binding sites and order supramolecularly in large 2D planes.

6.2.4   Spectroscopy on FeTPC Molecules

Before the peculiar duplex forms are investigated in terms of spectroscopy, an isolated single molecule is selected for point spectroscopy.

Spectroscopy curves are taken first on the clean copper to evaluate the tip quality, afterwards on the points of interest over the molecule and again on the copper, to check if the tip changed during the previous data acquisition. The result is shown in Fig. 6.15. The spectra are acquired on the positions marked by the colored circles in the STM image. The bias voltage is ramped from $U = -1000$ mV to $U = +1000$ mV with open feedback and the dI/dU-signal is recorded using a Lock-In amplifier. The blue spectra on the clean copper show the signature of the surface state and the tip did not change during acquisition.

The positions for spectra on the molecule where chosen by their special relevance
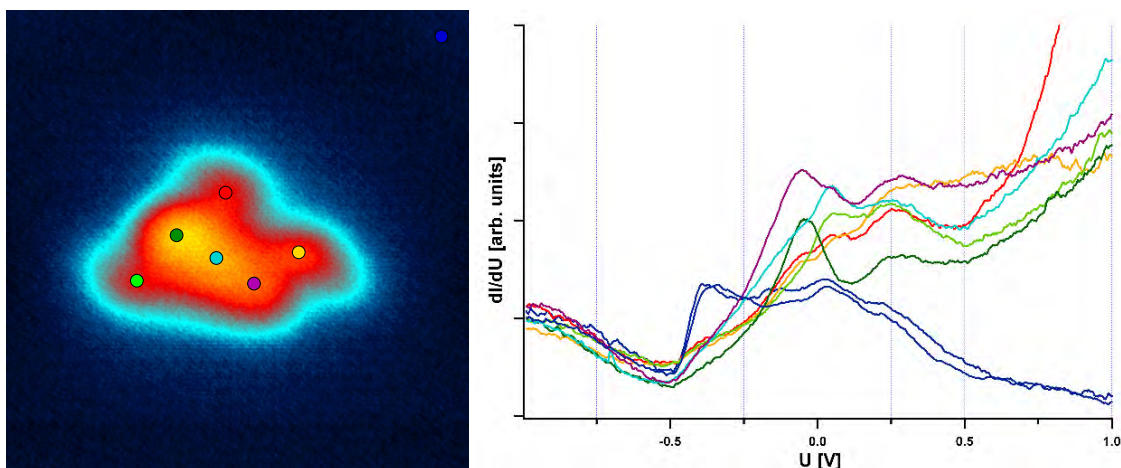
Figure 6.15: Point spectroscopy curves taken on locations indicated by colored circles in the STM image (left, 4×4 nm^2, $U = -1000$ mV). Spectra taken on the clean copper were acquired as the first and the last curve for reference.

(phenyl legs, pyrrolic units of the saddle and center of the molecule). Between $U = -1000$ mV and $U = -250$ mV all spectra are completely featureless and follow the background of the copper signal. Starting at $U = -250$ mV the signal from the molecule rises above the copper signal. The first small peak appears around $U = -100$ mV on the location of the pyrrolic units of the saddle. This higher signal on the molecule mainly at positive bias voltages gives a hint towards the presence of molecular states. Therefore, dI/dU-maps are acquired in the range of interest between $U = -250$ mV and $U = +1000$ mV.

A special location on the sample was selected: single molecules as well as all four duplex forms A–D are present in one area (see Fig. 6.16a). Two surface adsorbates and one subsurface defect are observed, which act as additional scatter points for the surface state electrons, but do not influence the electronic structure of the molecules.

The same scene is imaged with increasing bias voltage starting at $U = -250$ mV and the dI/dU-channel is recorded simultaneously (Figs. 6.16b-f). In the dI/dU-map taken at $U = -250$ mV the scattering of the surface electrons is clearly observed with each molecule acting as a scatter point. No signal from the molecules at this particular energy is observed, which fits to the single point spectra discussed before. With increasing bias voltage the signal of the surface state stays constant, but the signal from the molecules increases. The wavelength of the scattering pattern decreases due to the dispersion of the free electron like surface state electrons (Figs. 6.16c-f).

In the dI/dU-maps acquired at positive bias voltages, the molecular states are changing appearance depending on the voltage. The exact spatial distribution of these states over the single molecule and the duplex forms is investigated comparing them on a smaller lateral scale. Figure 6.17 shows a composition of STM topographs (first and last row) and dI/dU-maps (rows in between) of a single FeTPC molecule and the duplex forms A–D taken at the bias voltages as indicated.

The first column of images presents data taken on a single FeTPC molecule. The topographic channel shows the typical appearance of an FeTPC molecule imaged
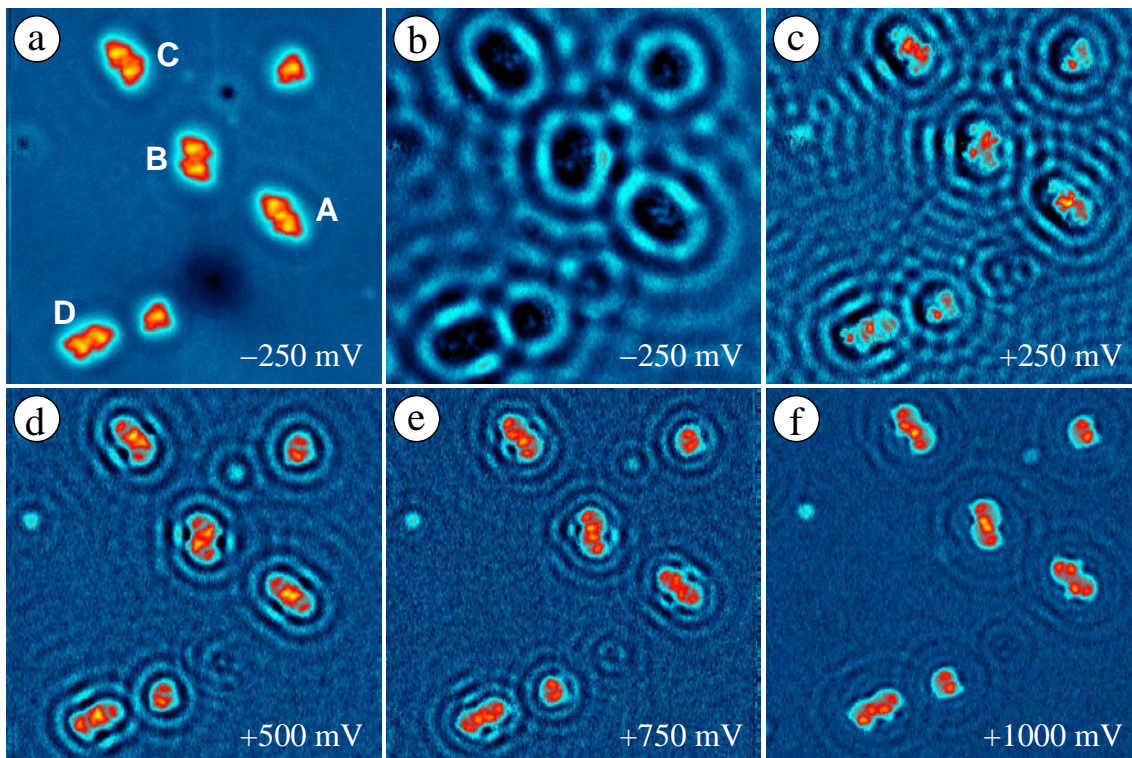
Figure 6.16: FeTPC molecules on Cu(111) imaged at different bias voltages as indicated, with the (a) topographic and (b)-(f) dI/dU-channel recorded simultaneously (all images: 25×25 nm^2).

with a metallic tip lacking the high resolution of a molecule tip. This is important, so that the states of a molecule at the tip do not influence the dI/dU measurement. Using a metallic tip with a flat density of states, the dI/dU-signal is dominated by the molecular states of the probed molecule on the sample. The dI/dU channel at $U = +250$ mV reveals a state located only on one phenyl leg of the FeTPC molecule. This asymmetry is not known from the literature of spectroscopy on TPP molecules but is reasonable because of the complete lack of symmetry in the FeTPC. Increasing the bias voltage ($U = +500$ mV and $U = +750$ mV), the shape of the molecular state becomes more symmetric and appears similar to the state known from TPPs [80]. The symmetry is broken again at $U = +1000$ mV and the dI/dU-map shows two bright maxima located over the region between one pyrrolic unit of the saddle and the adjacent phenyl legs. This is also visible in the topographic channel at this energy (last image of this column) and the distinct maximum of the saddle shape is flattened out. For an even more pronounced asymmetry in the electronic states see Sec. 6.3.3 about spectroscopy on FeTPC/Cu(100).

This big variation in the spatial distribution of electron density is used to analyze the four duplex structures. The increased apparent height of duplex form A discussed in the last section is investigated more thoroughly using dI/dU-maps. This maximum feature is observed in the topographic channel at $U = +250$ mV of duplex structure A. The related dI/dU-map at the same energy (see Fig. 6.17 second row) shows the asymmetric state above one phenyl ring pointed out before
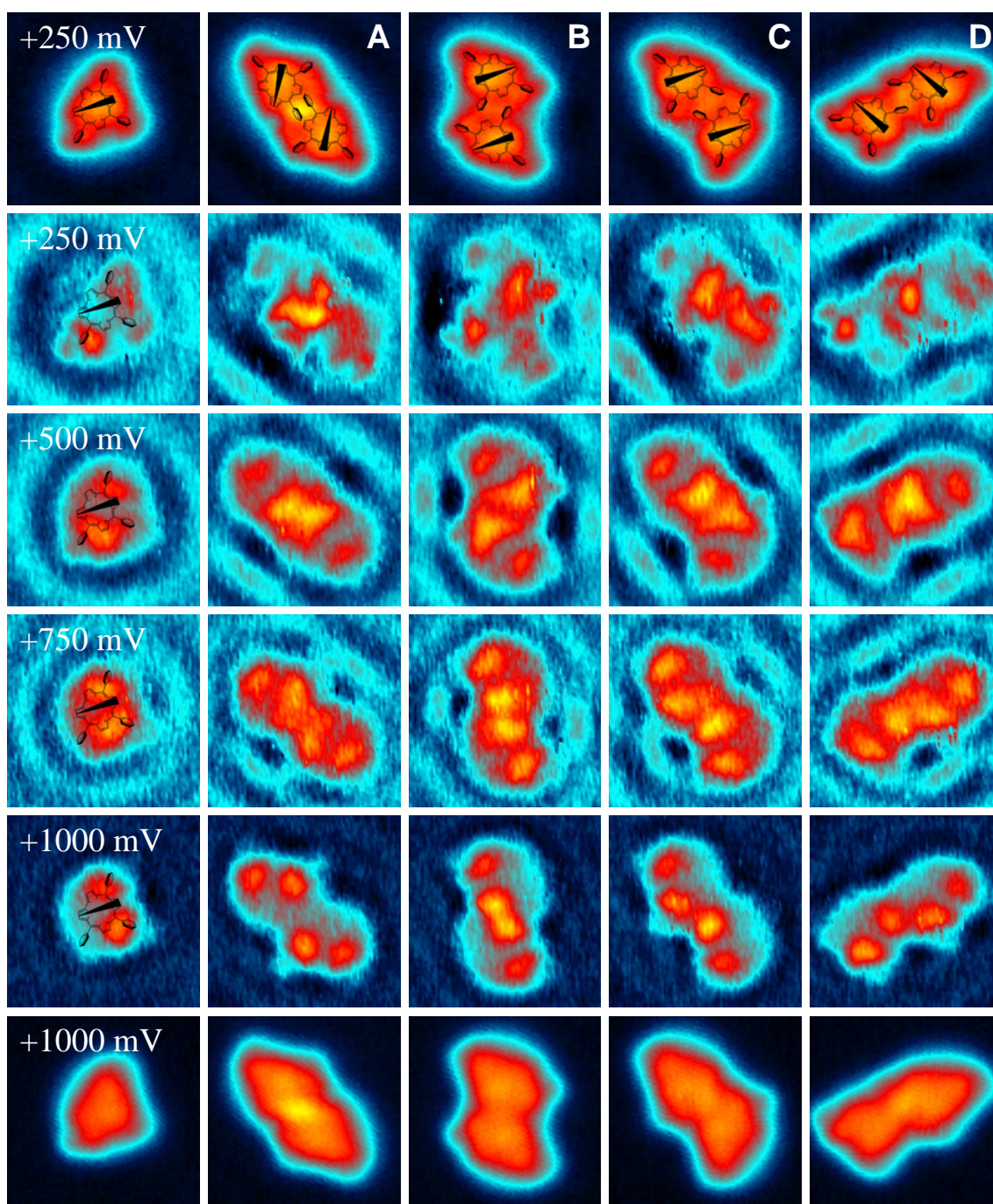
Figure 6.17: STM images and dI/dU-maps of a single isolated FeTPC molecule (first column) and the four duplex structures A–D (indicated in the first row). The first and last row show STM images at $U = +250$ mV and $U = +1000$ mV, respectively. Rows 2–5 show dI/dU-maps taken at $U = +250$ mV to $U = +1000$ mV as indicated (all images: 3×3 nm^2).

on the single molecule. This phenyl ring is responsible for the interaction between the molecules in form A and therefore the maximum in the dI/dU-map is observed at the site of interaction. The intensity of the maximum is larger compared to the

signal of this state on the single molecule. This results either from a higher electron density due to the coupling of the molecular states or from a different geometry of the molecular orbitals due to a stronger rotation of the interacting phenyl rings. Switching to a bias voltage of $U = +1000$ mV, the dI/dU-map reveals no electron density in the area of the interacting phenyl rings but the two maxima on the opposing side of the molecule similar to the single molecule. In the topographic channel at $U = +1000$ mV the increased height is still visible (last row). This leads to the conclusion, that the increased apparent height results from a geometrical deformation of the interacting phenyl rings and reflects a real increased height. This is also responsible for an increase in the electron density in the dI/dU-map at $U = +250$ mV due to a deformation of the molecular orbitals resulting from the different geometry or a stronger overlap.

The coupling between the molecules in the other duplex structures B–D is also observed by analyzing the dI/dU-maps. Investigating the molecular state at the location of interaction between the molecules in the particular duplex form ($U = +1000$ mV for B and $U = +500$ mV for C and D), an increase in intensity in comparison to the single molecule is observed. This is probably caused by an overlap of the molecular states at the site of interaction leading to an increase in electron density.

6.3 FeTPC Molecules on Cu(100)

Here, a study of FeTPC molecules adsorbed on the Cu(100) substrate is presented. Analog to the study on Cu(111), first the conformations of individual FeTPC molecules are analyzed and then self-assembly and the electronic structure are addressed. The difference between these two copper facets is described in detail in Sec. 3.1. The main properties of the (100) facet are the square lattice and the absence of a surface state.

6.3.1 Conformations of Individual FeTPC Molecules

Similar to the preparation on the Cu(111) substrate, isolated FeTPC molecules are observed for a low coverage on Cu(100) independent of the sample temperature during preparation. Eight different configurations of FeTPC molecules are found on the Cu(100) substrate as demonstrated in Fig. 6.18.

Four enantiomeric pairs are found with the saddle distortion of the macrocycle present for all observed molecules. This is in line with the observations on the FeTPC/Cu(111) system. However, the eight orientations of FeTPC/Cu(100) are aligned with the saddle along the closed packed rows of the substrate (sketched in Fig. 6.18 with black lines) and not perpendicular to them as on Cu(111). The already established notation of the different types is adopted from the FeTPC/Cu(111) system (α, β,... for the orientation and α vs α' for the two chiral conformations).
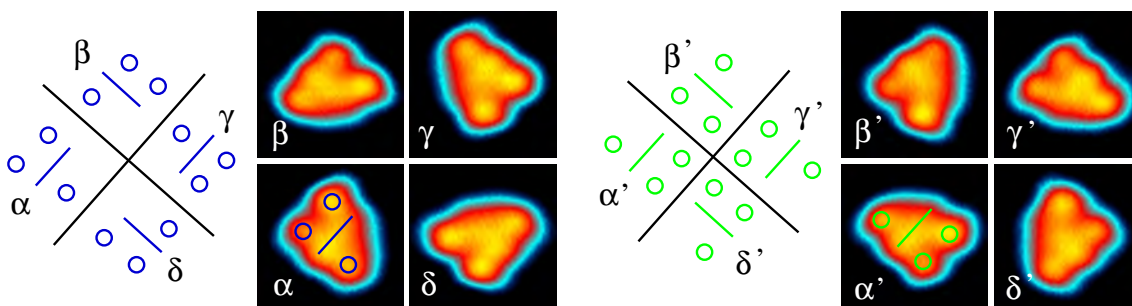
Figure 6.18: Isolated FeTPC molecules on a Cu(100) surface. Four different orientations with two enantiomeric variations are observed. The closed packed rows of the substrate are sketched by the black lines (all STM images 3×3 nm^2, $U = -1000$ mV).

6.3.2   Self-assembly of FeTPC Molecules

FeTPC molecules were evaporated on the Cu(100) substrate with the sample kept at room temperature. The result of this preparation is shown in Fig. 6.19a. Molecules form self-assembled structures, but isolated FeTPC molecules are also found similar to observations on Cu(111).

Analyzing the self-assembled structures, duplex formations similar to Cu(111) are found. In addition to the already known duplex formations A–E from FeTPC/Cu(111), two new duplex structures labeled as F+G are found. All arrangements A–G found in Fig. 6.19a (form D is not found in this particular STM image) are shown separately in Figs. 6.19c-h. For comparison and for better recognition a single molecule is shown in Fig. 6.19b, which is in configuration δ'.

Duplex forms A and B are composed of two molecules of the same chirality. Following the previously introduced notation, A is composed of molecules of configurations α and δ, B of β' and δ' respectively. C and E are made of two different chiral enantiomers (δ and δ' for C, β and δ' for E). The new duplex structures F and G are also composed of molecules of the same chirality (α and γ for F, α' and γ' for G).

In Fig. 6.20 all duplex structures are sketched in the same way introduced for the FeTPC/Cu(111) system. The molecules are simplified with the backbone of the saddle indicated by the wedged line and the rotation of the phenyl rings demonstrated by a black border pointing towards the observer. Additionally, the phenyl rings participating in the interaction of the duplex structure are marked by gray dots, the non-interacting ones with white circles.

The duplex forms A–E show exactly the same behavior and alignment as observed on Cu(111). Four phenyl rings participate in the interaction in structures A–C (marked by gray dots). In the case of forms D and E three phenyl rings are responsible for the interaction.

The two new duplex structures F and G show different interactions of the participating phenyl rings. In form F only two phenyl rings are interacting with the molecules connected on the bipyrrole sides. Form G exhibits four phenyl rings taking part in the assembly. The molecules in this duplex structure are oriented in the
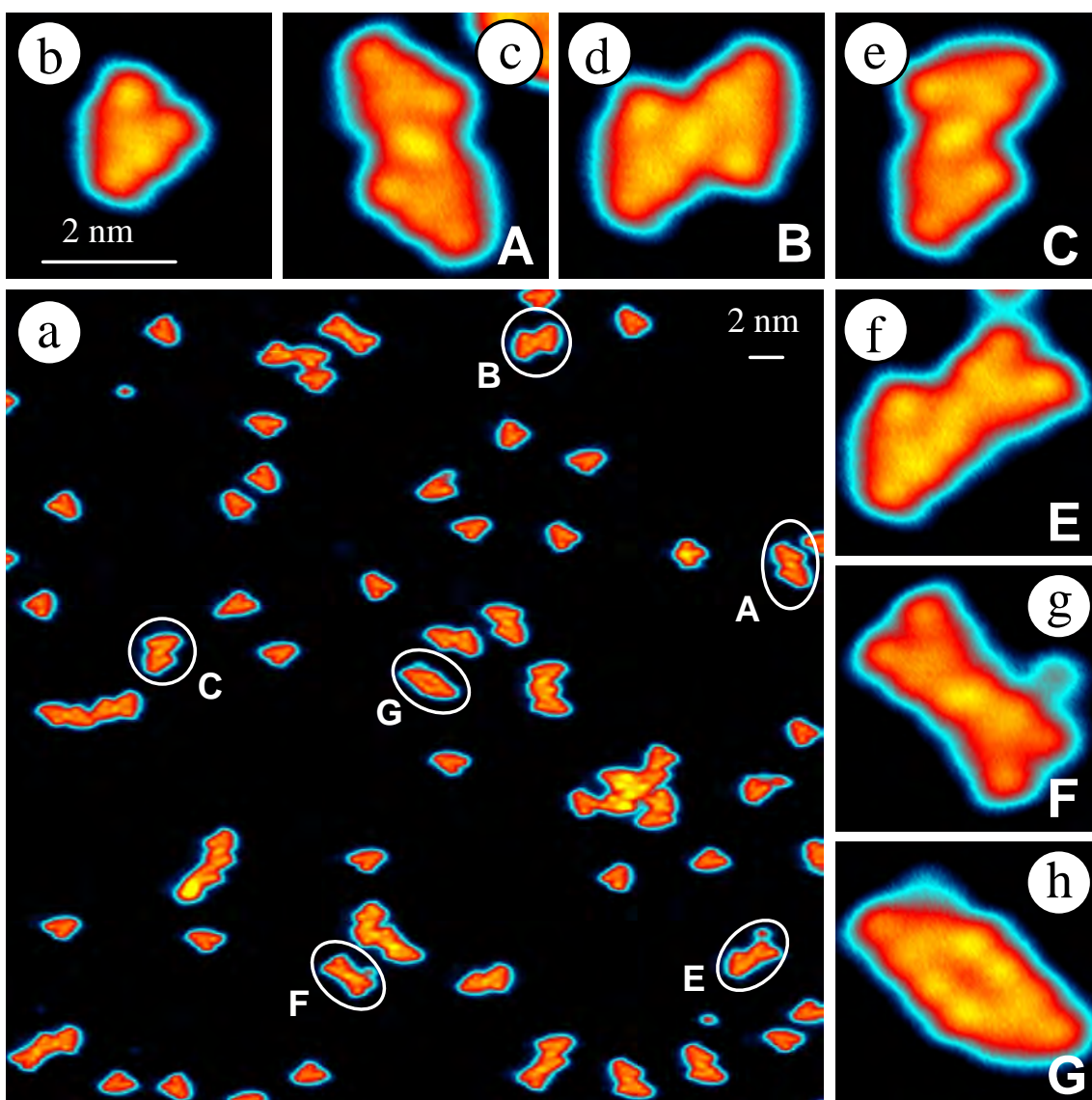
Figure 6.19: FeTPC molecules after a room temperature deposition on Cu(100). (a) Representative STM image of a low coverage. Isolated FeTPC molecules are dominant, but also duplex structures are found. The different duplex formations are marked with A–G. (b) Single FeTPC for comparison (c)-(h) Duplex forms A–G (D was not found in this exemplary image)

same way as in form A. The distance between the molecules is increased compared to A and the connection is done from the outer side and not with the rings in between each other.

The common feature between the new structures F and G and the known forms A–E is the arrangement of the saddle backbones of the two molecules in all duplex structures: they are all aligned parallely. This is obvious from the saddles indicated by the wedged lines in Fig. 6.20. Only duplex structures with this alignment are observed, although an arrangement of two molecules with their saddle backbones perpendicular to each other is possible from the observed conformations of single
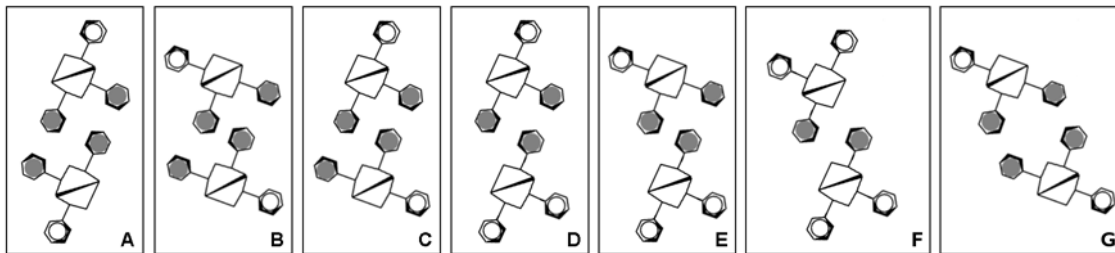
Figure 6.20: Sketches of coupled duplex configurations with four (A–C, G), three (D and E), and two (F) interacting phenyl groups. Interacting phenyl groups are indicated by gray dots, non-interacting by open circles. The backbone of the saddle distortion is indicated by the wedged line in the structures. The rotation of the phenyl rings out of the molecular plane is shown with the black border pointing towards the observer.

adsorbates	#	adsorbates	#
monomer	115	3mer (A+D)/(A+E)	2/1
2mer A	27	3mer (A+F)	4
2mer B	13	3mer (B+D)/(B+E)	1/1
2mer C	46	3mer (B+F)	1
2mer D	2	3mer (C+D)/(C+E)	4/1
2mer E	2	3mer (C+F)	6
2mer F	10	3mer (D+D)/(D+F)	1/1
2mer G	7	3mer (F+G)	1

Table 6.2: Frequencies of occurrence for different FeTPC aggregates (enantiomeric forms not resolved).

FeTPC molecules (e.g. β and γ).

In the next step, the complete numbers of occurrence of the observed structures on Cu(100) are compared and the numbers found on a representative set of images spanning an area of 22500 nm^2 is presented in table 6.2. The enantiomeric variations of the duplex structures are rated as equal and therefore not resolved. Duplex forms A–C are again the most favorable aggregates. This time the numbers are in favor of form C instead of form A. Structures D and E are only rarely found. The frequency of occurrence for F and G is lower compared to A–C, but higher than D and E. They are also found in certain trimer formations. Thus, F and G are counting as new duplex forms only found on the Cu(100) surface. For another investigation of the coupling in the duplex forms, the electronic structure of duplex forms F and G is compared to forms A and C in Sec. 6.3.3 using dI/dU-maps.

Comparing the numbers from table 6.2 with the numbers of the FeTPC on Cu(111) system summarized in table 6.1, a mismatch in the ratio between single molecules and duplex forms is observed. The single molecules are more frequent than the duplex forms on Cu(100). On Cu(111) the ratio is 24:139 and on Cu(100) it is 115:107. To check if this is really due to the reduced mobility on Cu(100) and not consolidated by some desire of the molecules to stay isolated perhaps induced by
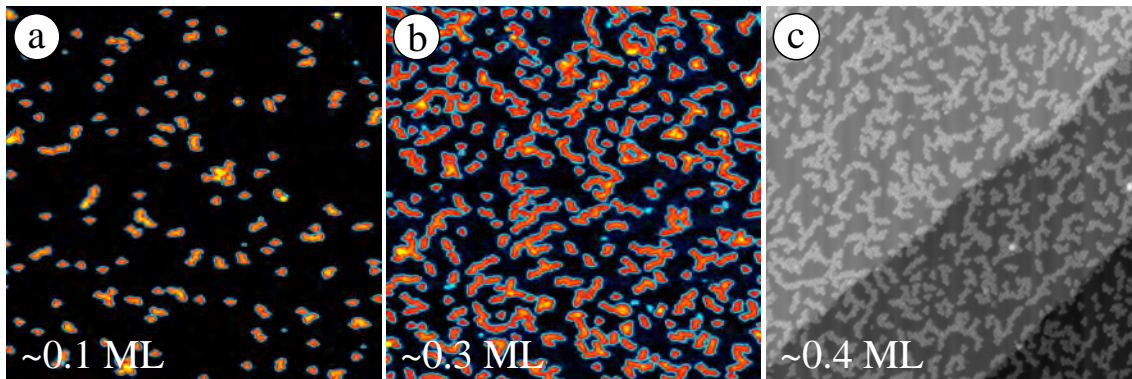
Figure 6.21: Different coverages of FeTPC molecules after room temperature deposition on Cu(100). The coverage is slightly increased from (a) ∼0.1 ML to (b) ∼0.3 ML and ∼0.4 ML to compare the ratio between single molecules and duplex structures (all STM images 75×75 nm², $U = -1000$ mV).

a critical density of molecules, the coverage is varied slightly for three preparations and the ratio is compared. Representative STM images for these three coverages of ∼0.1 ML, ∼0.3 ML and ∼0.4 ML are shown in Fig. 6.21. Coverages higher than 0.4 ML were not found to be reasonable, because the total amount of single molecules and duplex forms becomes too small. For every coverage an area of 100 x 100 nm² was counted.

Only for the preparation with ∼0.1 ML the duplex forms are found in smaller quantities than the single ones; the ratio being 3:1 for the monomers. With an increase of coverage to ∼0.3 ML the numbers are equal (55 monomers to 53 duplex forms). The ratio of 1:1 changes only slightly with an increasing coverage to ∼0.4 ML, but the total number of single and duplex structures per area is decreasing (23 monomers and 31 duplex structures). Tempering the sample above room temperature to further increase the mobility of the single molecules has to be performed to get more information about this mismatch with the findings on Cu(111).

6.3.3 Electronic Structure of FeTPC Molecules

Similar to the analysis of electronic states of FeTPC on Cu(111), also on the Cu(100) surface a single isolated molecule is selected and point spectroscopy curves over special points of the molecule are taken. This is presented in Fig. 6.22 with the colored circles marking the locations of spectra. The copper reference was taken on the clean copper just outside the topographic image (black curve). Similar to the Cu(111) case, the spectra on the molecule follow the spectrum of the copper for negative energies between $U = -1500$ mV and $U = -500$ mV. Around $U = -250$ mV all molecule spectra reveal a state and on the positive side the curves show different behavior with different onset values. The local variation in the spectra especially for positive energies is investigated in more detail taking dI/dU-maps. Figure 6.23(left) shows a topographic image of an isolated molecule with corresponding dI/dU-maps taken at various energies as indicated. The spatial variation in the electron density is quite drastic and much stronger than on the Cu(111) substrate. As mentioned
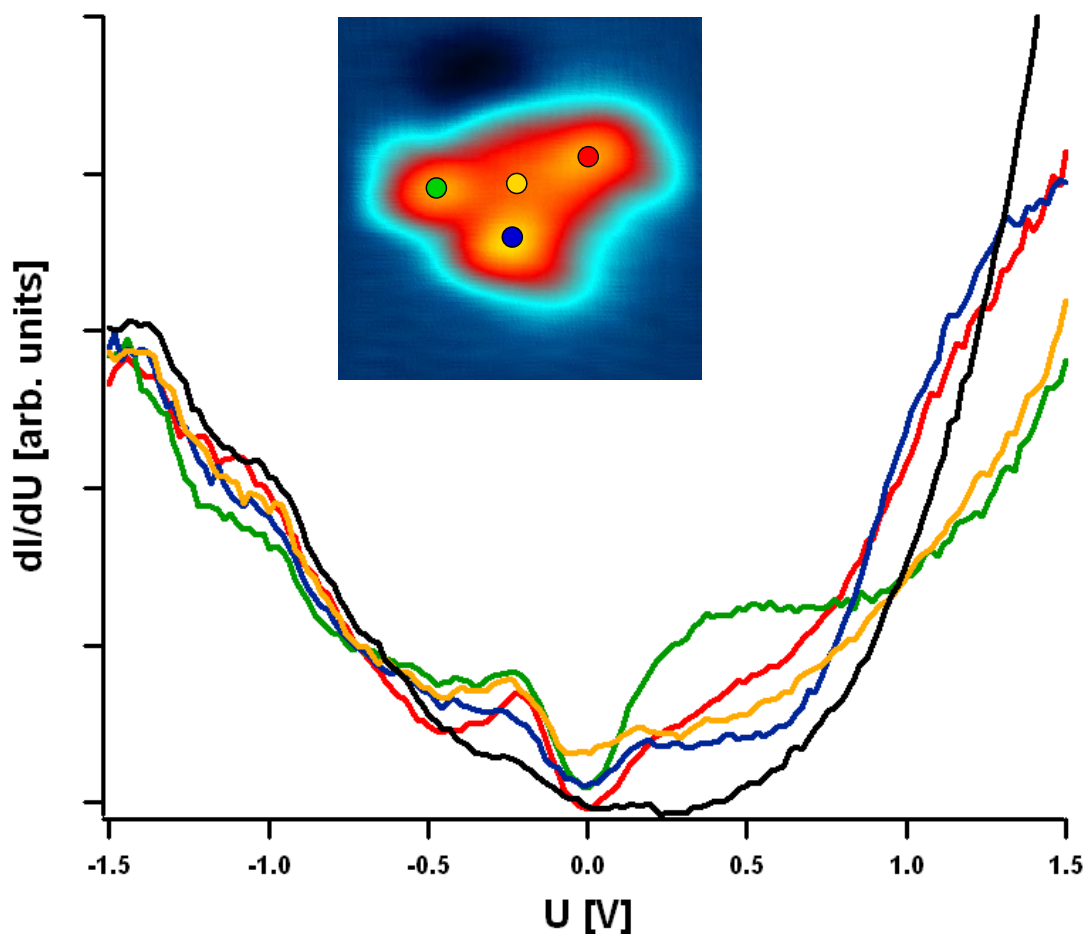
Figure 6.22: Point spectra taken on various spots on an isolated FeTPC molecule on Cu(100). The positions are marked by colored circles (inset: 3×3 nm^2). The reference spectrum of the copper substrate (black line) was taken on the clean copper outside the topographic STM image.

above, at $U = -500$ mV and below the intensity of electron density on the molecule is equal to the one on the substrate. The state around $U = -250$ mV exhibits two bright maxima on the location of the pyrrolic units from the saddle backbone. This is similar to the LUMO state observed for CoTPPs on copper (see Sec. 3.3.2 and [80]).

The most striking features are the asymmetric states on the phenyl legs at $U = +250$ mV and $U = +1000$ mV. They reflect the diversity of all three legs in sense of rotation compared to the macrocycle of the molecule and the surface and in sense of coupling to the substrate states. The orientation of the phenyl ring is even recognizable in the shape of the molecular state. This is visualized in Fig. 6.23(right), where the chemical model of the molecule is superimposed with the shapes of the three important molecular states at $U = -250$ mV (red), $U = +250$ mV (blue) and $U = +1000$ mV (green). The shapes of the states are reduced to the area of the maxima. The chemical model bears the same orientation including the saddle
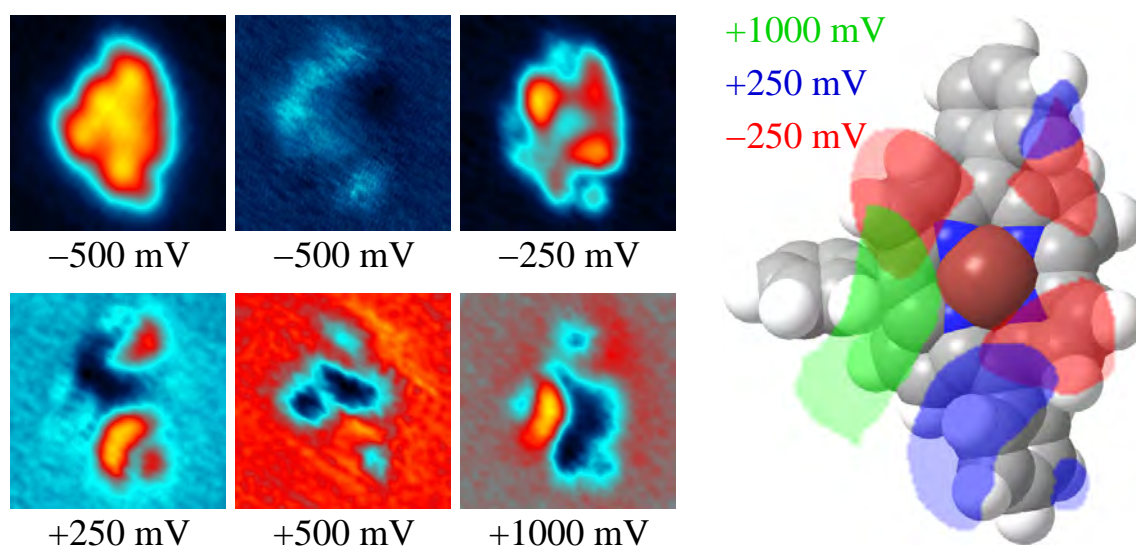
Figure 6.23: Left: STM images of an isolated FeTPC molecule on Cu(100). The orientation of the molecule can be recognized as β' from the topographic channel (upper left). The $\mathrm{d}I/\mathrm{d}U$-maps taken at the indicated energies reveal a strong variation in the spatial distribution of electron density over the molecule (all STM images: $3 \times 3 \ \mathrm{nm}^2$). Right: Chemical model of the molecule bearing the same orientation and saddle distortion as the molecule in the STM images on the left. The shapes of the three important states are superimposed over the model with a color code indicating the locations on the molecule participating in the electron density.

distortion as the selected isolated molecule in the STM images. For $U = -250$ mV (red) the main area of the electron density fits to the location of the bent up pyrrolic units of the macrocycle. The molecular orbital at $U = +250$ mV (blue) fits to the rotation of the participating phenyl rings. The lower ring is bent up on the left side, the other one on the right. The signature observed in the $\mathrm{d}I/\mathrm{d}U$-map fits to the regions of the phenyl rings pointing up towards the STM tip. The maximum on the lower ring is exhibiting a higher intensity than the upper ring. The $\mathrm{d}I/\mathrm{d}U$-map taken at $U = +1000$ mV (green) exhibits a maximum in the region of the left phenyl ring, also pointing in the direction of the ring rotation.

The distinct shape of the molecular state on the phenyl legs at $U = +250$ mV is now used for further investigation of the interaction in the duplex forms of the molecules. In Fig. 6.24 a selection of the observed duplex structures is presented with their topographic (top row) and differential conductance channel (bottom row).

First, a comparison is made of the duplex forms A and C, to understand the frequency of occurrence in favor of structure C (A is favored on Cu(111), compare Sec. 6.2.3). The appearance of duplex form A is similar to the appearance on Cu(111) both in the topographic and the $\mathrm{d}I/\mathrm{d}U$ channel. The phenyl rings participating in the molecular interaction exhibit a maximum in apparent height as well as in the electron density. The same observation is made for form C, with an increase in apparent height and in electron density on the location of the responsible phenyl rings. This is in contrast to the observation for duplex structure C on Cu(111), where no increase is observed and leads to an understanding of the stronger coupling for C
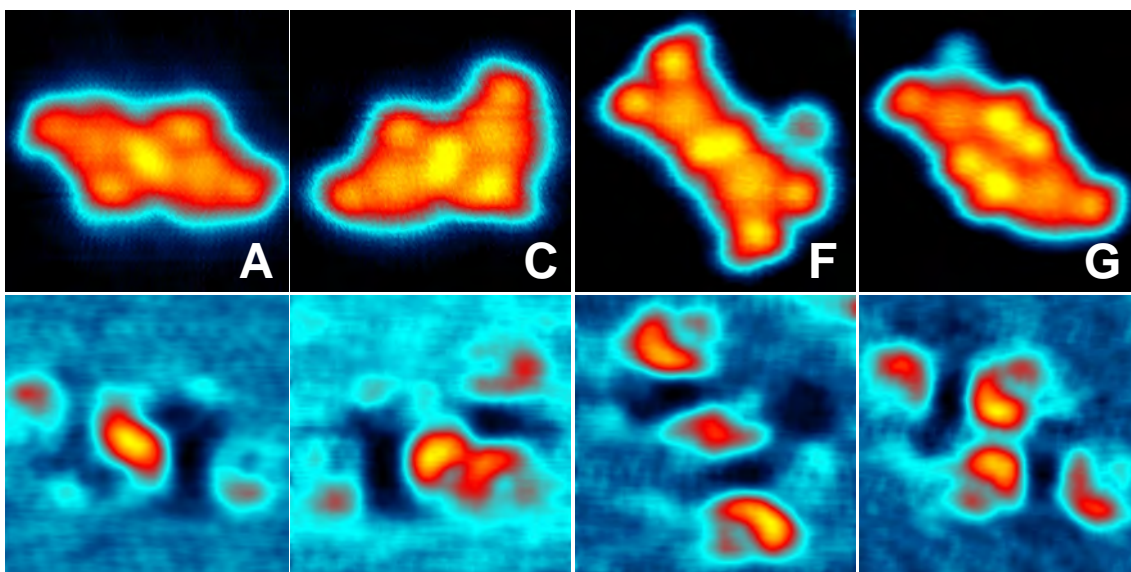
Figure 6.24: Selected duplex forms of FeTPC on Cu(100) presented with the topographic channel (top row) and the dI/dU-map (bottom row) taken at $U = +250$ mV (all images: 4×4 nm^2).

on Cu(100) than on Cu(111), but still the favor of this structure compared to form A remains unclear.

In the topographic images of duplex forms F and G also an increase in the apparent height for the interacting phenyl rings is found, but no increase in the electron density in comparison to the signature of the single molecule. Duplex form G can be interpreted as an intermediate state to duplex structures A and B. The molecules are already aligned in the same way, but somehow a small barrier has to be overcome to go from structure G to A or B. This would explain the reduction in frequency of occurrence for the structures A and B. For duplex form F no explanation is found so far to fit the preferred alignment of molecules in form F compared to the similar form E.

6.4   FeTPC molecules on NaCl/Cu(111)

To check the role of the substrate influence on the conformation of these molecules, an insulating adlayer is introduced to decouple the molecules from the metallic substrate. After preparation of 1 ML islands of NaCl on the Cu(111) substrate (see Sec. 3.1.4), molecules are evaporated on the cold surface. The result from this preparation can be seen in Fig. 6.25.

The coupling between the NaCl and the molecules is so weak, that the molecules are easily pushed around by the tip during scanning (see molecule on NaCl terrace in Fig. 6.25a). Two conformations are observed: one conformation without any symmetry (white circle) and a conformation exhibiting a symmetry axis (black circles). For comparison, the inset in Fig. 6.25a shows the magnification of a FeTPC molecule on the Cu(111) terrace.
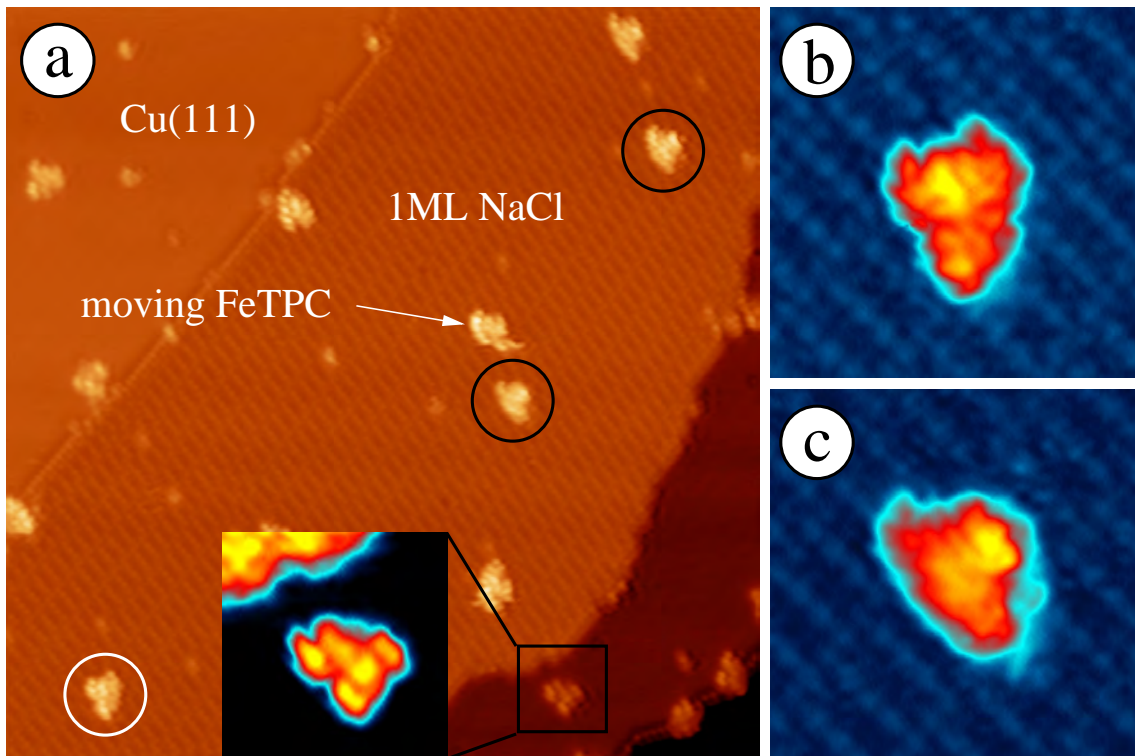
Figure 6.25: FeTPC molecules evaporated on NaCl/Cu(111). (a) The image shows a 1ML island of NaCl on a Cu(111) substrate. The two different conformations of the molecule observed are marked by circles. The saddle conformation (white circle) is observed on the Cu(111) (see inset) and on the NaCl. The planar conformation (black circles) is only seen on the NaCl island (40×40 nm^2, $U = -1500$ mV). (b)+(c) Single molecule in (b) saddle and (c) planar conformation on the NaCl terrace (5×5 nm^2, $U = -2000$ mV).

Figures 6.25b+c show individual molecules of both conformations on the NaCl island with high resolution. The distinct Moiré pattern of the NaCl atomic lattice is clearly resolved. Comparing the FeTPC molecule without any symmetry (Fig. 6.25b and white circle in Fig. 6.25a) with FeTPC molecules on the Cu(111) with the known saddle conformation (see inset in Fig. 6.25a), the agreement in appearance is persuasive. All typical features of the saddle conformation are observed for the molecule on NaCl: no apparent symmetry axis, one elongated cigar shaped center between three outer protrusions with an increased height on the side of the two protrusions (see Fig. 6.25b). In the case of the conformation shown in Fig. 6.25c the situation is different. The molecule exhibits a symmetry axis similar to the planar molecular structure of FeTPC. This structure is also dominant in number of appearances. Together with the fact of the weak interaction between the molecules and the insulating NaCl film, the interpretation of this structure as the planar conformation of the molecule is reasonable.

Chapter 7

Summary and Outlook

In this thesis a study of magnetic molecules with varying structures and properties on metallic surfaces and insulating adlayers is presented. The investigation covers the basic features, i.e. adsorption, growth behavior, and electronic structure. For these measurements the setup of a specially designed UHV system was realized. It offers the possibility to study molecules over the whole temperature range between 20–300 K. Additionally, the preparation of molecules on precooled samples with a defined flux is achieved. This is especially important for the study of isolated molecules and molecular systems on insulating adlayers. The properties of the used substrates ((111) and (100) facets of copper and NaCl/Cu(111)) and preparational techniques of molecular systems on these surfaces are described in detail. Three different classes of molecules are used in this study with the focus slightly varying due to their special structural characteristics. All molecules bear a metallic atom in the central position.

The phthalocyanine (PC) molecule is completely planar exhibiting a four-lobed cross shape both in molecular structure and topographic STM images. Preparation of these molecules with Cu, Co, and Fe as metallic center on both copper facets leads to a strong hybridization of molecular and substrate states due to their flat structure. Therefore, no electronic features in spectroscopy are observed, which is consistent with literature. Self-assembly of molecules prepared on a room temperature sample is not observed. PC molecules stay isolated and exhibit three orientations on Cu(111) and two on Cu(100). When prepared on a precooled sample, two additional meta-stable states on Cu(100) are observed. On Cu(111) all PC molecules appear with a break of symmetry which is not observed on the Cu(100) surface: two opposing lobes show an increased apparent height compared to the other two. This is explained by a slight bending of the molecule due to the strong interaction with the substrate.

The chirality of Co-Salen molecules resulting from a tilted top bridge is observed on the Cu(111) surface, leading to interesting features from the direct bridge-surface interaction. Molecules are observed in six orientations with two enantiomeric variations. The asymmetry is reflected in the topographic appearance as well as in the electronic structure. The injection of high energy electrons from the STM tip at elevated voltages (above 1.7 V), causes a dehydrogenation of the top bridge. Three different states (intact, single, and double dehydrogenated) of molecules are easily

distinguished in STM images and dI/dU-maps. The so far preliminary work of S. Sanvito *et al.* using DFT calculations to model STM images and dI/dU-maps of Co-Salen molecules on Cu(111) presented in this thesis will be extended to all three states of the dehydrogenation process. On Cu(100) also meta-stable states are found when preparing Co-Salen on the cold substrate. On both facets of copper, no self-assembly is observed for the normal Co-Salen, but substituting the hydrogen atoms in the 5,5'-positions with chloride induces additional dipolar moments from a changed charge distribution. This leads to the formation of two-dimensional networks on the surface.

For all FeTPC derivatives used in this thesis, the discociation of the axial group is observed already during the preparation. Pure FeTPC is left on the surface. The corrole molecule shows a similar behavior on metallic surfaces as reported for the parent porphyrin molecule: the macrocycle is distorted into a saddle conformation from the interaction with the substrate. This saddle conformation introduces chirality into the corrole structure and is observed on both copper facets. Both enantiomeric versions are found in six orientation on Cu(111) and in four orientations on Cu(100). Molecules can be converted between different conformations by manipulation with the STM tip. With slightly different manipulation parameters, a new conformation can be created, which shows features of the dome conformation. On NaCl the saddle and an additional planar conformation are observed. FeTPC molecules are mobile during room temperature preparation on both copper facets and form self-assembled structures. Duplex formations are dominant, which is more strongly pronounced on Cu(111). The slight decoupling of the macrocycle from the substrate due to the phenyl rings and the asymmetry of FeTPC on the surface lead to peculiar molecular states in dI/dU-maps with a different contribution for every phenyl ring. Additional spectroscopic measurements are proposed to gain more insight into the coupling mechanism in the duplex structures. The derivatives of FeTPC were chosen from their different magnetic properties steered by the axial group. Therefore, another experiment will be the dosing of pure FeTPC on the surface with molecular oxygen and NO to create again FeTPC with different magnetic states.

The knowledge about the investigated molecules concerning adsorption, growth and electronic structure gained from the results of this thesis gives a solid basis for further magnetic measurements using SP-STM. Experiments on phthalocyanine molecules are in progress and are planned for salen and corrole molecules as well.

Bibliography

[1] H. Schiff, Ann. Suppl. **3**, 343 (1864).

[2] A. W. Johnson and R. Price, J. Chem. Soc. 1649 (1960).

[3] A. Aviram and M. A. Ratner, Chem. Phys. Lett. **29**, 277 (1974).

[4] A. S. Martin, J. R. Sambles, and G. J. Ashwell, Phys. Rev. Lett. **70**, 218 (1993).

[5] M. A. Reed, C. Zhou, C. J. Muller, T. P. Burgin, and J. M. Tour, Science **278**, 252 (1997).

[6] J. Park, A. N. Pasupathy, J. I. Goldsmith, C. Chang, Y. Yaish, J. R. Petta, M. Rinkoski, J. P. Sethna, H. D. A. na, P. L. McEuen, and D. C. Ralph, Nature **417**, 722 (2002).

[7] W. Liang, M. P. Shores, M. Bockrath, J. R. Long, and H. Park, Nature **417**, 725 (2002).

[8] A. R. Rocha, V. M. García-Suárez, S. W. Bailey, C. J. Lambert, J. Ferrer, and S. Sanvito, Nat. Mater. **4**, 335 (2005).

[9] L. A. Bumm, J. J. Arnold, M. T. Cygan, T. D. Dunbar, T. P. Burdin, L. J. II, D. L. Allara, J. M. Tour, and P. S. Weiss, Science **271**, 1705 (1996).

[10] C. J. Chen, *Introduction to Scanning Tunneling Microscopy* (Oxford University Press, New York, 1993).

[11] G. Binnig, H. Rohrer, C. Gerber, and E. Weibel, Phys. Rev. Lett. **49**, 57 (1982).

[12] G. Binnig, H. Rohrer, C. Gerber, and E. Weibel, Appl. Phys. Lett. **40**, 178 (1982).

[13] P. O. Gartland and B. J. Slagsvold, Phys. Rev. B **12**, 4047 (1975).

[14] J. Bardeen, Phys. Rev. Lett. **6**, 57 (1961).

[15] J. Tersoff and D. R. Hamann, Phys. Rev. B **31**, 805 (1985).

[16] R. J. Hamers, Annu. Rev. Phys. Chem. **40**, 531 (1989).

[17] J. K. Gimzewski, E. Stoll, and R. R. Schlittler, Surf. Sci. **181**, 267 (1987).

[18] P. H. Lippel, R. J. Wilson, M. D. Miller, C. Wöll, and S. Chiang, Phys. Rev. Lett. **62**, 171 (1989).

[19] P. G. Arscott, G. Lee, V. A. Bloomfield, and D. F. Evans, Nature **339**, 484 (1989).

[20] R. J. Driscoll, M. G. Youngquist, and J. D. Baldeschwieler, Nature **346**, 294 (1990).

[21] J. S. Foster, J. E. Frommer, and P. C. Arnett, Nature **331**, 324 (1988).

[22] B. C. Stipe, M. A. Rezaei, and W. Ho, Science **279**, 1907 (1998).

[23] T. A. Jung, R. R. Schlittler, J. K. Gimzewski, H. Tang, and C. Joachim, Science **271**, 181 (1996).

[24] W. Mizutani, M. Shigeno, Y. Sakakibara, K. Kajimura, M. Ono, S. Tashima, K. Ohno, and N. Toshima, J. Vac. Sci. Technol. A **8**, 675 (1990).

[25] M. Pomerantz, A. Aviram, R. A. McCorkle, L. Li, and A. G. Schrott, Science **255**, 1115 (1992).

[26] B. C. Stipe, M. A. Rezaei, and W. Ho, Science **280**, 1732 (1998).

[27] J. K. Spong, H. A. Mizes, L. J. L. Jr, M. M. Dovek, J. E. Frommer, and J. S. Foster, Nature **338**, 137 (1989).

[28] R. Sonnenfeld and P. K. Hansma, Science **232**, 211 (1986).

[29] J. S. Foster and J. E. Frommer, Nature **333**, 542 (1988).

[30] D. P. E. Smith, J. K. H. Hörber, G. Binnig, and H. Nejoh, Nature **344**, 641 (1990).

[31] B. Hulsken, R. van Hameren, J. W. Gerritsen, T. Khoury, P. Thordarson, M. J. Crossley, A. E. Rowan, R. J. M. Nolte, J. A. A. W. Elemans, and S. Speller, Nat. Nanotech **2**, 285 (2007).

[32] G. P. Lopinski, D. J. Moffatt, D. D. M. Wayner, and R. A. Wolkow, Nature **392**, 909 (1998).

[33] T. A. Jung, R. R. Schlittler, and J. K. Gimzewski, Nature **386**, 696 (1997).

[34] S. Weigelt, C. Busse, L. Petersen, E. Rauls, B. Hammer, K. V. Gothelf, F. Besenbacher, and T. R. Linderoth, Nat. Mater. **5**, 112 (2006).

[35] S.-W. Hla, L. Bartels, G. Meyer, and K.-H. Rieder, Phys. Rev. Lett. **85**, 2777 (2000).

[36] V. Iancu and S.-W. Hla, PNAS **103**, 13718 (2006).

[37] F. Chiaravalloti, L. Gross, K.-H. Rieder, S. M. Stojkovic, A. Gourdon, C. Joachim, and F. Moresco, Nat. Mater. **6**, 30 (2007).

[38] L. Grill, K.-H. Rieder, F. Moresco, G. Rapenne, S. Stojkovic, X. Bouju, and C. Joachim, Nat. Nanotech **2**, 95 (2007).

[39] S.-W. Hla, K.-F. Braun, B. Wassermann, and K.-H. Rieder, Phys. Rev. Lett. **93**, 208302 (2004).

[40] A. Zhao, Q. Li, L. Chen, H. Xiang, W. Wang, S. Pan, B. Wang, X. Xiao, J. Yang, J. G. Hou, and Q. Zhu, Science **309**, 1542 (2005).

[41] S. Katano, Y. Kim, M. Hori, M. Trenary, and M. Kawai, Science **316**, 1883 (2007).

[42] X. H. Qiu, G. V. Nazin, and W. Ho, Science **299**, 542 (2003).

[43] J. Repp, G. Meyer, S. M. Stojković, A. Gourdon, and C. Joachim, Phys. Rev. Lett. **94**, 026803 (2005).

[44] J. Köhler, J. A. J. M. Disselhorst, M. C. J. M. Donckers, E. J. J. Groenen, J. Schmidt, and W. E. Moerner, Nature **363**, 242 (1993).

[45] J. Wrachtrup, C. von Borczyskowski, J. Bernard, M. Orrit, and R. Brown, Nature **363**, 244 (1993).

[46] P. Gambardella, S. Rusponi, M. Veronese, S. S. Dhesi, C. Grazioli, A. Dallmeyer, I. Cabria, R. Zeller, P. H. Dederichs, K. Kern, C. Carbone, and H. Brune, Science **300**, 1130 (2003).

[47] A. Scheybal, T. Ramsvik, R. Bertschinger, M. Putero, F. Nolting, and T. A. Jung, Chem. Phys. Lett. **411**, 214 (2005).

[48] H. Wende, M. Bernien, J. Luo, C. Sorg, N. Ponpandian, J. Kurde, J. Miguel, M. Piantek, X. Xu, P. Eckhold, W. K. , K. Baberschke, P. M. Panchmatia, B. Sanyal, P. M. Oppeneer, and O. Eriksson, Nat. Mater. **6**, 516 (2007).

[49] Y. Manassen, R. J. Hamers, J. E. Demuth, and A. J. C. Jr., Phys. Rev. Lett. **62**, 2531 (1989).

[50] C. Durkan and M. E. Welland, Appl. Phys. Lett. **80**, 458 (2002).

[51] F. Meier, L. Zhou, J. Wiebe, and R. Wiesendanger, Science **320**, 82 (2008).

[52] Y. Yayon, V. W. Brar, L. Senapati, S. C. Erwin, and M. F. Crommie, Phys. Rev. Lett. **99**, 067202 (2007).

[53] U. Kaiser, A. Schwarz, and R. Wiesendanger, Nature **446**, 522 (2007).

[54] J. Li, W.-D. Schneider, R. Berndt, and B. Delley, Phys. Rev. Lett. **80**, 2893 (1998).

[55] V. Madhavan, W. Chen, T. Jamneala, M. F. Crommie, and N. S. Wingreen, Science **280**, 567 (1998).

[56] V. Iancu, A. Deshpande, and S.-W. Hla, Nano Lett. **6**, 820 (2006).

[57] V. Iancu, A. Deshpande, and S.-W. Hla, Phys. Rev. Lett. **97**, 266603 (2007).

[58] Y.-S. Fu, S.-H. Ji, X. Chen, X.-C. Ma, R. Wu, C.-C. Wang, W.-H. Duan, X.-H. Qiu, B. Sun, P. Zhang, J.-F. Jia, and Q.-K. Xue, Phys. Rev. Lett. **99**, 256601 (2007).

[59] C. Iacovita, M. V. Rastei, B. W. Heinrich, T. Brumme, J. Kortus, L. Limot, and J. P. Bucher, Phys. Rev. Lett. **101**, 116602 (2008).

[60] Variable-temperature UHV SPM by Omicron NanoTechnology GmbH.

[61] CryoVac Gesellschaft fuer Tieftemperaturtechnik, D-53842 Troisdorf.

[62] Lakeshore Ltd., 'Cryogenic Reference Table'.

[63] E. P. Roth and A. C. Anderson, J. Appl. Phys. **47**, 3644 (1976).

[64] Ph.D. Thesis, T. Haenke, University of Hamburg (2005).

[65] S. H. Pan, International Patent Publication No. WO 93/19494 (International Bureau, World Intellectual Property Organization), September 30,1993.

[66] J. Wiebe, A. Wachowiak, F. Meier, D. Haude, T. Foster, M. Morgenstern, and R. Wiesendanger, Rev. Sci. Instrum. **75**, 4871 (2004).

[67] O. Pietzsch, A. Kubetzka, D. Haude, M. Bode, and R. Wiesendanger, Rev. Sci. Instrum. **71**, 424 (2000).

[68] R. Bennewitz, V. Barwich, M. Bammerlin, C. Loppacher, M. Guggisberg, A. Baratoff, E. Meyer, and H.-J. Güntherodt, Surf. Sci. **438**, 289 (1999).

[69] R. Bennewitz, A. S. Foster, L. N. Kantorovich, M. Bammerlin, C. Loppacher, S. Schär, M. Guggisberg, E. Meyer, and A. L. Shluger, Phys. Rev. B **62**, 2074 (2000).

[70] G. Hörmandinger, Phys. Rev. B **49**, 13897 (1994).

[71] W. Shockley, Phys. Rev. **56**, 317 (1939).

[72] M. Crommie, C. Lutz, and D. Eigler, Nature **363**, 524 (1993).

[73] J. Kliewer, R. Berndt, E. V. Chulkov, V. M. Silkin, P. M. Echenique, and S. Crampin, Science **288**, 1399 (2000).

[74] J. Repp, G. Meyer, S. Paavilainen, F. E. Olsson, and M. Persson, Science **312**, 1196 (2006).

[75] C. Schwennicke, J. Schimmelpfennig, and H. Pfnür, Surf. Sci. **293**, 57 (1993).

[76] Ph.D. Thesis, J. Repp, FU Berlin (2002).

[77] W. Hebenstreit, J. Redinger, Z. Horozova, M. Schmid, R. Podloucky, and P. Varga, Surf. Sci. **424**, L321 (1999).

[78] S. Fölsch, A. Helms, S. Zöphel, J. Repp, G. Meyer, and K.-H. Rieder, Phys. Rev. Lett. **84**, 123 (2000).

[79] J. Repp, G. Meyer, and K.-H. Rieder, Phys. Rev. Lett. **92**, 036803 (2004).

[80] A. Weber-Bargioni, W. Auwärter, F. Klappenberger, J. Reichert, S. Lefrançois, T. Strunskus, C. Wöll, A. Schiffrin, Y. Pennec, and J. V. Barth, ChemPhysChem **9**, 89 (2008).

[81] X. W. Tu, G. R. Mikaelian, and W. Ho, Phys. Rev. Lett. **100**, 126807 (2008).

[82] G. V. Nazin, X. H. Qiu, and W. Ho, Science **302**, 77 (2003).

[83] M. Takada and H. Tada, Jpn. J. Appl. Phys. **44**, 5332 (2005).

[84] P. Jiang, X. Ma, Y. Ning, C. Song, X. Chen, J.-F. Jia, and Q.-K. Xue, J. Am. Chem. Soc. **130**, 7790 (2008).

[85] A. Scarfato, S.-H. Chang, S. Kuck, J. Brede, G. Hoffmann, and R. Wiesendanger, Surf. Sci. **602**, 677 (2008).

[86] L. Gao, W. Ji, Y. B. Hu, Z. H. Cheng, Z. T. Deng, Q. Liu, N. Jiang, X. Lin, W. Guo, S. X. Du, W. A. Hofer, X. C. Xie, and H.-J. Gao, Phys. Rev. Lett. **99**, 106402 (2007).

[87] X. Lu and K. W. Hipps, J. Phys. Chem. B **101**, 5391 (1997).

[88] Z. H. Cheng, L. Gao, Z. T. Deng, Q. Lin, N. Jiang, X. Lin, X. B. He, S. X. Du, and H.-J. Gao, J. Phys. Chem. C **111**, 2656 (2007).

[89] Z. H. Cheng, L. Gao, Z. T. Deng, N. Jiang, Q. Liu, D. X. Shi, S. X. Du, H. M. Guo, and H.-J. Gao, J. Phys. Chem. C **111**, 9240 (2007).

[90] J. Åhlund, J. Schnadt, K. Nilson, E. Göthelid, J. Schiessling, F. Besenbacher, N. Mårtensson, and C. Puglia, Surf. Sci. **601**, 3661 (2007).

[91] T. G. Gopakumar, M. Lackinger, M. Hackert, F. Müller, and M. Hietschold, J. Phys. Chem. B **108**, 7839 (2004).

[92] M. Koudia, M. Abel, C. Maurel, A. Bliek, D. Catalin, M. Mossoyan, J.-C. Mossoyan, and L. Porte, J. Phys. Chem. B **110**, 10058 (2006).

[93] Y. Wang, J. Kröger, R. Berndt, and W. Hofer, Angew. Chem. Int. Ed. **48**, ASAP (2009).

[94] K. Walzer and M. Hietschold, Surf. Sci. **471**, 1 (2001).

[95] X. Chen, Y.-S. Fu, S.-H. Ji, T. Zhang, P. Cheng, X.-C. Ma, X.-L. Zou, W.-H. Duan, J.-F. Jia, and Q.-K. Xue, Phys. Rev. Lett. **101**, 197208 (2008).

[96] J. C. Buchholz and G. A. Somorjai, J. Chem. Phys. **66**, 573 (1977).

[97] CuPC, CoPC, and FePC powder, 90% purity, Sigma-Aldrich.

[98] P. Liljeroth, J. Repp, and G. Meyer, Science **317**, 1203 (2007).

[99] A. Rosa and E. J. Baerends, Inorg. Chem. **33**, 584 (1994).

[100] T. Tsumaki, Bull. Chem. Soc. Jpn **13**, 252 (1938).

[101] N. S. Venkataramanan, G. Kuppuraj, and S. Rajagopal, Coord. Chem. Rev. **249**, 1249 (2005).

[102] E. N. Jacobsen, Acc. Chem. Res. **33**, 421 (2000).

[103] P. G. Cozzi, Chem. Soc. Rev. **33**, 410 (2004).

[104] J. Park, K. Lang, K. A. Abboud, and S. Hong, J. Am. Chem. Soc. **130**, 16484 (2008).

[105] M. H. Chisholm and Z. Zhou, J. Am. Chem. Soc. **126**, 11030 (2004).

[106] D. J. Darensbourg, A. I. Moncada, W. Choi, and J. H. Reibenspies, J. Am. Chem. Soc. **130**, 6523 (2008).

[107] W. Zhang, J. L. Loebach, S. R. Wilson, and E. N. Jacobsen, J. Am. Chem. Soc. **112**, 2801 (1990).

[108] R. Irie, K. Noda, Y. Ito, N. Matsumoto, and T. Katsuki, Tetrahedron Lett. **31**, 7345 (1990).

[109] W. Hirahata, R. M. Thomas, E. B. Lobkovsky, and G. W. Coates, J. Am. Chem. Soc. **130**, 17658 (2008).

[110] Y. Shimazaki, T. Yajima, F. Tani, S. Karasawa, K. Fukui, Y. Naruta, and O. Yamauchi, J. Am. Chem. Soc. **129**, 2559 (2007).

[111] S. L. Holt, R. Delasi, and B. Post, Inorg. Chem. **10**, 1498 (1971).

[112] S. Brückner, M. Calligaris, G. Nardin, and L. Randaccio, Acta Cryst. **B25**, 1671 (1969).

[113] W.-B. Yuan, H.-Y. Wang, J.-F. Du, S.-W. Chen, and Q. Zhang, Acta Cryst. **E62**, m3504 (2006).

[114] A. W. Johnson and I. T. Kay, J. Chem. Soc. 1620 (1965).

[115] D. C. Hodgkin, J. Pickworth, J. H. Robertson, K. N. Trueblood, R. J. Prosen, and J. G. White, Nature **176**, 325 (1955).

[116] E. Vogel, S. Will, A. S. Tilling, L. Neumann, J. Lex, E. Bill, A. X. Trautwein, and K. Wieghardt, Angew. Chem. Int. Ed. **33**, 731 (1994).

[117] D. T. Gryko, J. P. Fox, and D. P. Goldberg, J. Porphyrins Phthalocyanines **8**, 1091 (2004).

[118] S. Nardis, D. Monti, and R. Paolesse, Mini-Rev. Org. Chem. **2**, 355 (2005).

[119] K. M. Kadish, L. Frémond, Z. Ou, J. Shao, C. Shi, F. C. Anson, F. Burdet, C. P. Gros, J.-M. Barbe, and R. Guilard, J. Am. Chem. Soc. **127**, 5625 (2005).

[120] I. Aviv and Z. Gross, Chem. Commun. 1987 (2007).

[121] M. Bröring, F. Brégier, E. Cónsul Tejero, C. Hell, and M. C. Holthausen, Angew. Chem. Int. Ed. **46**, 445 (2007).

[122] S. Nardis, R. Paolesse, S. Licoccia, F. R. Fronczek, M. G. H. Vicente, T. K. Shokhireva, S. Cai, and F. A. Walker, Inorg. Chem. **44**, 7030 (2005).

[123] B. Koszarna and D. T. Gryko, J. Org. Chem. **71**, 3707 (2006).

[124] S. Cai, S. Licoccia, C. DOttavi, R. Paolesse, S. Nardis, V. Bulach, B. Zimmer, T. K. Shokhireva, and F. A. Walker, Inorg. Chim. Acta **339**, 171 (2002).

[125] C. A. Joseph and P. C. Ford, J. Am. Chem. Soc. **127**, 6737 (2005).

[126] O. Zakharieva, V. Schünemann, M. Gerdan, S. Licoccia, S. Cai, F. A. Walker, and A. X. Trautwein, J. Am. Chem. Soc. **124**, 6636 (2002).

[127] W. Auwärter, A. Weber-Bargioni, S. Brink, A. Riemann, A. Schiffrin, M. Ruben, and J. V. Barth, ChemPhysChem **8**, 250 (2007).

[128] N. Wintjes, J. Hornung, J. Lobo-Checa, T. Voigt, T. Samuely, C. Thilgen, M. Stöhr, F. Diederich, and T. Jung, Chem.–Eur. J. **14**, 5794 (2008).

[129] F. Rosei, M. Schunack, P. Jiang, A. Gourdon, E. Lægsgaard, I. Stensgaard, C. Joachim, and F. Besenbacher, Science **296**, 328 (2002).

[130] F. Moresco, C. Joachim, and K. H. Rieder, Surf. Interface Anal. **36**, 109 (2004).

[131] W. Auwärter, F. Klappenberger, A. Weber-Bargioni, A. Schiffrin, T. Strunskus, C. Wöll, Y. Pennec, A. Riemann, and J. V. Barth, J. Am. Chem. Soc. **129**, 11279 (2007).

Publications

1. A. Scarfato, S.-H. Chang, S. Kuck, J. Brede, G. Hoffmann, and R. Wiesendanger: *Scanning tunneling microscopy study of iron(II) phthalocyanine growth on metal and insulating surfaces*; Surf. Sci. **602**, 677 (2008)

2. S. Kuck, J. Wienhausen, G. Hoffmann, and R. Wiesendanger: *A versatile variable-temperature scanning tunneling microscope for molecular growth*; Rev. Sci. Instr. **79**, 083903 (2008)

3. S. Kuck, G. Hoffmann, M. Bröring, M. Fechtel, M. Funk, and R. Wiesendanger: *"Naked" Iron-5,10,15-triphenylcorrole on Cu(111): Observation of Chirality on a Surface and Manipulation of Multiple Conformational States by STM*; J. Am. Chem. Soc. **130**, 14072 (2008)

4. S.-H. Chang, S. Kuck, J. Brede, L. Lichtenstein, G. Hoffmann, and R. Wiesendanger: *Symmetry reduction of metal phthalocyanines on metals*; Phys. Rev. B **78**, 233409 (2008)

5. S. Kuck, S.-H. Chang, J.-P. Klöckner, M. H. Prosenc, G. Hoffmann, and R. Wiesendanger: *Steering two dimensional molecular growth via dipolar interaction*; ChemPhysChem (accepted)

6. J. Brede, S. Kuck, J. Schwöbel, S.-H. Chang, M. Linares, G. Hoffmann, A. Scarfato, R. Wiesendanger, R. Lensen, P. Kouwer, J. Hoogboom, A. Rowan, M. Bröring, M. Funk, S. Stafström, F. Zerbetto, and R. Lazzaroni: *Dynamics of molecular self-ordering on metallic substrates*; Nanotechnology (submitted)

Conferences

- S. Kuck, G. Hoffmann, and R. Wiesendanger: *Design of a scanning tunneling microscope for variable temperatures in an ultra-high-vacuum environment*, 68th Spring Conference, Deutsche Physikalische Gesellschaft, Regensburg, Germany, 08.03.2004 (poster).

- S. Kuck, A. Wachowiak, G. Hoffmann, and R. Wiesendanger: *STM study of CuPC molecules on Cu(111) and Au(111)*, 70th Spring Conference, Deutsche Physikalische Gesellschaft, Dresden, Germany, 29.03.2006 (poster).

- S. Kuck, J. Wienhausen, A. Wachowiak, F. Vonau, G. Hoffmann, and R. Wiesendanger: *Single CuPC molecules on Cu(111) and Au(111)*, International Conference on Nanoscience and Technology, Basel, Switzerland, 01.08.2006 (poster).

- S. Kuck, J. Brede, F. Vonau, A. Scarfato, G. Hoffmann, and R. Wiesendanger: *Phthalocyanines on Surfaces*, 71st Spring Conference, Deutsche Physikalische Gesellschaft, Regensburg, Germany, 26.03.2007 (poster).

- G. Hoffmann, S. Kuck, J. Brede, A. Scarfato, and R. Wiesendanger: *Magnetic Molecules in the Scanning Tunneling Microscope*, Colloquium of SPP 1137 "Molekularer Magnetismus", Bad Dürkheim, Germany, 07.05.2007 (poster).

- S. Kuck, J. Brede, F. Vonau, G. Hoffmann, R. Wiesendanger, S. May, J.-P. Klöckner, and M. Prosenc: *STM investigation of Salen-complexes*, International Conference on Nanoscience and Technology, Stockholm, Sweden, 03.07.2007 (poster).

- G. Hoffmann, S. Kuck, J. Brede, and R. Wiesendanger: *STM / STS investigations of porphyrin and corrole molecules on surfaces*, 72nd Spring Conference, Deutsche Physikalische Gesellschaft, Berlin, Germany, 27.02.2008 (poster).

- S. Kuck, J. Brede, G. Hoffmann, and R. Wiesendanger: *Conformational study of FeTPC molecules on Cu(111) with STM*, 72nd Spring Conference, Deutsche Physikalische Gesellschaft, Berlin, Germany, 28.02.2008 (talk).

- S. Kuck, L. Lichtenstein, G. Hoffmann, and R. Wiesendanger: *Electronic structure of FeTPC on Cu(111) vs Cu(100) investigated with STM and STS*, 73rd Spring Conference, Deutsche Physikalische Gesellschaft, Dresden, Germany, 23.03.2008 (talk).

- L. Lichtenstein, S. Kuck, G. Hoffmann, and R. Wiesendanger: *Adsorption Geometry and Self-assembly of Corrole Molecules*, 73rd Spring Conference, Deutsche Physikalische Gesellschaft, Dresden, Germany, 25.03.2008 (poster).

- S.-H. Chang, J. Brede, J. Schwöbel, S. Kuck, G. Hoffmann, and R. Wiesendanger: *Adsorption of metal phthalocyanines on Cu(111) and Cu(100): A STM study*, 73rd Spring Conference, Deutsche Physikalische Gesellschaft, Dresden, Germany, 25.03.2008 (poster).

Acknowledgements

At this place I would like to thank everybody who helped and supported me during the last five years on the work of this thesis. A few prominent ones are named for their special role.

Prof. Roland Wiesendanger for providing me with the opportunity to make my PhD-thesis in his research group and giving me an excellent support during that time.

My supervisor Germar Hoffmann for being there during the good and the bad times.

Thanks to Jan Wienhausen for helping me set up the VT-lab, François Vonau for accompanying me on the first steps in the molecular world and to all the other members of the Hoffmann subgroup.

A very special thank you to Jens Brede for being a huge support in the process of this thesis.

Also thanks to the whole group R. The atmosphere in the group is very productive and friendly and I enjoyed the last years working here.

Mr. Benecke and his team of the mechanical workshop for the excellent parts they machined for the VT-STM setup.

The workgroup of Prof. Marc Prosenc for the provision and guidance in chemical questions concerning Salen molecules.

Prof. Martin Bröring and everybody in his group who provided us with corrole molecules. We had a lot of helpful and important discussions about molecules.

And finally I thank my family. My wife Tanja, who supported me with the same effort and enthusiasm I myself put into the thesis. My lovely daughters Leonie Sophie and Anna Karlotta for keeping me awake at night. My sister for proof reading this thesis and my brother-in-law for moral support. My parents for their patience and great help during this long period.